High Frequency Magnetic Core Loss Study

Mingkai Mu

Dissertation submitted to the faculty of the
Virginia Polytechnic Institute and State University
in partial fulfillment of the requirements for the degree of

Doctor of Philosophy
in
Electrical Engineering

Fred C. Lee, Chair
Dushan Boroyevich
Paolo Mattavelli
Jaime De La Ree
Dwight Viehland

February 22nd, 2013
Blacksburg, Virginia

Keywords: Magnetic core loss, measurement, high frequency,
non-sinusoidal excitation, DC bias, core loss model,
finite element, low temperature co-fired ceramics,
magnetic characterizations

High Frequency Magnetic Core Loss Study

Mingkai Mu

Abstract

The core used to build power inductors and transformers are soft magnetic materials. When there is alternating external field, the magnetic moments rotate and consume energy, which is the core loss. The core loss depends on the AC flux frequency, amplitude, waveform, DC bias and temperature. These dependences are nonlinear and difficult to predict. How to measure, model and analyze the core loss is a challenge for decades.

In this dissertation, two new core loss measurement methods are introduced first. These two methods use the reactive cancellation concept to reduce the sensitivity to phase discrepancy, which will destroy the accuracy in classic two-winding method for high frequency high quality factor sample measurements. By using the new measurement techniques the accuracy can be improved by several orders. The first is for sinusoidal waveforms, and the second is for non-sinusoidal wave. The new methods enable high frequency core loss characterization capability, which will help scientists and engineers on material research and inductor/transformer design. Measurement examples, considerations and error analysis are demonstrated and discussed in detail.

With the measurement techniques, the core loss under rectangular AC voltage and DC bias current are investigated. A new core loss model named rectangular extension Steinmetz equation (RESE) is proposed based on the measurement results. The new model is shown to be more accurate than the existing core loss models. Several commercially available MnZn ferrites are characterized and modeled.

Other than conventional MnZn ferrite materials, three commercial LTCC ferrite materials are characterized for integrated power supply applications. Based on characterized properties of these LTCCs, a group of new LTCC ferrites are fabricated and tested. The new LTCC is fabricated by laminating commercial LTCC tapes and co-firing. The new LTCC is demonstrated to have over 50% more inductance over the commercial LTCC materials. This work indicates that the power electronics engineers should work with material engineers to get the optimum material for a given application.

In the last part, the core loss of the partially saturated lateral flux planar inductor is analyzed. The challenge of the analysis is the complexity of the distribution of bias field and flux density in a highly biased planar inductor. Each point in the core is working at different excitation and bias condition, and the core loss density is very non-uniform. The proposed method combines the characterization tested in previous chapters and the commercial finite element tool. Experiments verified that the calculation errors are within about 10%.

In conclusion, the research in this dissertation proposed a complete solution to measure, model and analyze the high frequency core loss. This solution will not only facilitate fundamental research on physics understanding and material innovation, but also development of power electronics and RF applications.

To My Family:
My parents: Zhigang Mu
Xiaoai Xu
My wife: Yu Zhao
My sister: Meng Mu

ACKNOWLEDGMENTS

Many people have helped me during my Ph.D. study. It is impossible for me to finish this job without them.

First I would like to thank my advisor, Dr. Fred C. Lee for his guidance in my studies. He has not only taught me the knowledge of power electronics, but also the rigorous attitude towards research. His invaluable training and enlightenment will be with me for all my life. Having the opportunity to study with him has been an honor.

I am grateful to my committee members: Dr. Dushan Boroyevich, Dr. Paolo Mattavelli, Dr. Jaime De La Ree, and Dr. Dwight Viehland. Their advice, experience, and encouragement have contributed significantly to my research and understanding of fundamentals.

I would like to thank my colleagues in the power management consortium (PMC) of Center for Power Electronics Center (CPES) over the years. It is my honor to work with these talented people. Many thanks go to: Dr. Ming Xu, Dr. Qiang. Li, Dr. Michele Lim, Dr. Yan Dong, Dr. Wenli Zhang, Mr. David Gilham, Mr. Yipeng Su, Mr. Alex Ji, Dr. Dongbin Hou, Dr. David Reusch, Dr. Julu Sun, Dr. Jian Li, Dr Arthur Ball, Dr. Dianbo Fu, Dr. Chuanyun Wang, Dr. Pengju Kong, Mr. Yi Sun, Mr. Zheng Luo, Mr. Daocheng Huang, Mr. Pengji Lai, Mr. Zijian Wang, Mr. Qian Li, Dr. Yingyi Yan, Mr. Feng Yu, Mr. Haoran Wu, Mr. Yi Jiang, Mr. Chanwit Prasantanakorn, Mr. Weiyi Feng, Mr. Shuilin Tian, Mr. Wei Zhang, Mr. Li Jiang, Mr. Pei-Hsin Liu, Mr. Xiucheng Huang, Mr.

Zhengyang Liu, Mr. Yuchen Yang. I also appreciate all other colleagues and students in CPES. It is precious memory to live and work with you for the past years.

Many visiting scholars have bought their expertise and helpful discussion during my research. They are: Dr. Feng Zheng, Dr. Xinke Wu, Dr. Kuang-Yao Cheng, Dr. Xiaoyong Ren, Mr. Zeng Li, Mr. Feng Wang, Dr. Hao Zhang. Thank you for the help and friendship.

The excellent faculty and staff has facilitated my research and provided the best resources available. I would like to thank Dr. Khai Ngo, Dr. Fang Luo, Igor Cvetkovic, Douglas Sterk, Teresa Shaw, Linda Gallagher, Trish Rose, Linda Long, Marianne Hawthorne, and Cindy Hopkins in the graduate advising office.

I would like to thank my parents and sister. Though they are an ocean away, their love always encouraged me to finish this journey. I am very grateful to my loving wife, Yu Zhao, for her support through the years. With her love and support, my life at Blacksburg has been full of joy.

Many thanks for the CPES PMC consortium members for the funding of my research: Chicony Power Technology Co., Ltd., Delta Electronics, Enpirion INC, Huawei Technologies, International Rectifier, Intersil Corporation, Linear Technology, NEC/TOKIN Corporation, NXP Semiconductors, Richtek Technology, Texas Instruments, Infineon, ZTE Corporation and Simplis Technologies INC, etc. I would also like to thank ARPA-E for their funding on the project "Power Supplies on a Chip".

Table of Contents

List of Figures

List of Tables

Chapter One Introduction

1.1 Background of Magnetic Core Loss

The cores used to build inductors and transformers are usually made of soft magnetic materials. The core loss of power inductors and transformers are important for the converter's efficiency and power density [1][2][3]. The core loss is induced by the magnetic domain wall movement and resonance. These domain walls bounds small magnetic domains within the magnetic materials. A magnetic domain is a region which has uniform magnetization. The individual magnetic moments of all atoms within the domain are aligned and point in the same direction. Thus the magnetization within each domain points in the same direction, but the magnetization of other domains may point in different directions. So the net magnetization is neutral in the absence of external magnetizing fields. At the domain walls, the magnetization rotates coherently from the direction in one domain to that in the next domain. When there is an alternating external field, the domain wall moves and consumes energy, which gives rise to core loss.

There are two sources of core loss: hysteresis loss and eddy current loss. The hysteresis loss is the energy consumed to change the direction of the magnetic moments within the domains. It refers to the area enclosed by the static hysteresis loop shown in Fig. 1.1. The hysteresis loss dominates at low frequencies. [4]

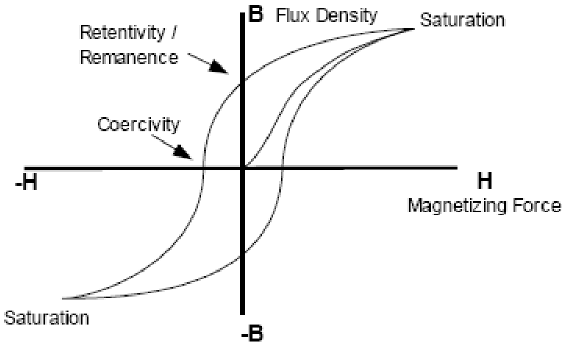

Figure 1.1 Hysteresis loop

When the frequency increases, the loop area becomes bigger. This is because of the eddy current loss. The eddy current loss is traditionally divided into two parts. One is called classic eddy current loss and the other is called excess loss (or anomalous loss). Excess loss accounts for the difference between the measured loss and the sum of calculated hysteresis loss and the classic eddy current loss. This loss was explained as eddy current loss due to localized magnetization [5]. Because the material is composed of domains that are heterogeneous, when the external field changes, the magnetization happens only near the domain walls. So the actual eddy current loss is higher than the calculated eddy current assumed under uniform magnetization.

The core loss of some commercial powder materials and ferrites are shown in Fig. 1.2. Some emerging materials like LTCC ferrites, flake, and thin film materials are also shown here [6][7][8][9][10][11]. Due to lack of measurement data, this map is limited to 10MHz only.

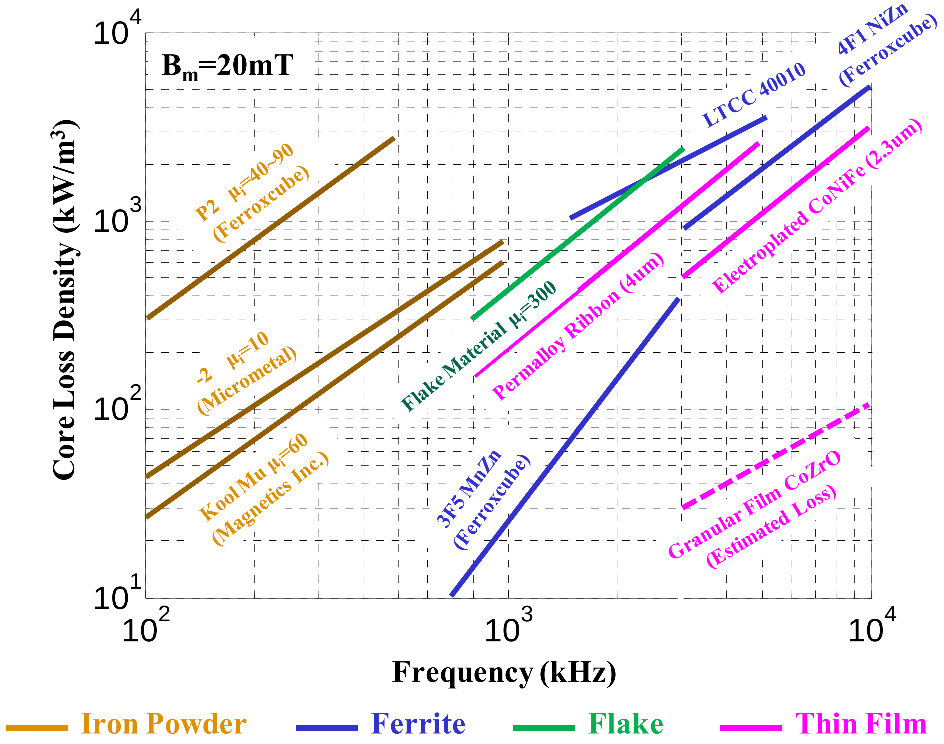

Figure 1.2 Core loss map for high frequency materials

In Fig. 1.2, the loss is measured under sinusoidal excitation with no DC bias. This information is of limited help in power electronics applications, because the core loss depends on many aspects:

1. AC excitation frequency and amplitude: According to early researches on core loss [12], the AC excitation frequency and amplitude directly affect the core loss.

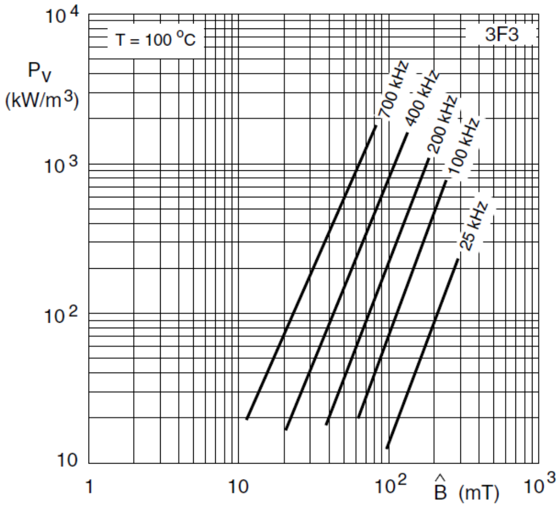

Figure 1.3 Core loss vs. peak flux density and frequency (3F3 from Ferroxcube)[13]

The simplest equation which can model the core loss with minimum number of parameters is the Steinmetz equation.

$$P_{core} = kf^{\alpha} B_m^{\beta} \tag{1.1}$$

Parameter k, α, β are curve fitted with measurement data. α is typically a number between 1 and 2; β is typically between 1.5 and 3. These coefficients vary material to material and because of the nonlinearity of core loss, the Steinmetz parameters are valid for a limited range of frequencies and flux densities. A group of ferrite materials are modeled with Steinmetz equation and are shown in Table 1.1 [14]. When the frequency range is wide, different sets of Steinmetz parameters are defined to maintain accuracy all over the range. Some literatures reported different ways to use unified Steinmetz parameters to model the core loss over a wide range. [15][16]. These parameters are still derived by fitting the measurement data.

Table 1.1 Steinmetz parameters for segmented frequency range [14]

Material	Frequency	k	α	β
3C94	20-200	2.37e-3	1.46	2.75
	200-400	2e-9	2.6	2.75
3F3	100-300	0.25e-3	1.63	2.45
	300-500	2e-5	1.8	2.5
	500-1000	3.6e-3	2.4	2.25
3F4	500-1000	12e-4	1.75	2.9
	1000-3000	1.1e-11	2.8	2.4

2. Waveform has strong impact to the core loss. Instead of sinusoidal waveform, the rectangular voltages are the most commonly seen waveforms in power electronics applications. Many literatures have reported that the core loss under rectangular excitation is different from sinusoidal excitation, and the duty cycle plays an important role to the loss. In 1978, by comparing the measured the core loss of various materials under these excitations, Chen [17][18] discovered that the core loss for square voltage excitation is lower than the sinusoidal excitation with the same AC flux amplitude. In 1991, by using Fourier analysis, Severns [19] analyzed the core loss for rectangular excitations under duty cycles other than 50%. At 50% duty cycle, the higher order harmonics are very small, so the core loss is dominated by the fundamental. The triangular excitation's fundamental amplitude is lower than sinusoidal, so its loss is lower than sinusoidal. As the duty cycle becomes smaller or bigger, the high order harmonics makes the core loss larger than the sinusoidal. This Fourier analysis helped the qualitative understanding of the core loss under non-sinusoidal excitations, but it is not quantitatively accurate.[20] In 1996, Albach etc. [20]

measured and explained non-sinusoidal core loss by relating the core loss with the rate of change of flux (dB/dt), and not just on the flux swing. According to this explanation, the first generalized core loss model for non-sinusoidal excitation was proposed, which is also called modified Steinmetz equation (MSE). [21] The normalized core loss for rectangular voltage excitation as predicted by MSE is shown in Fig.1.4. After this work, numerous core loss models are proposed, like GSE[22], iGSE[23],NSE[24], DNSE[25],WcSE[26], i^2GSE[28], etc. These models give quick estimation for the non-sinusoidal core loss, but none of them have enough experimental verification for different frequency ranges, waveform profiles or materials. They tried to provide a universal solution to predict the non-sinusoidal core loss, but ignored the complexity of the core loss of various ferro- or ferri-magnetic materials. The hypotheses and derivation of these models are discussed in Section 1.3. So far, because of lack of good understanding to the core loss under different waveforms, measurement is still the only reliable and accurate way to know the actual core loss.

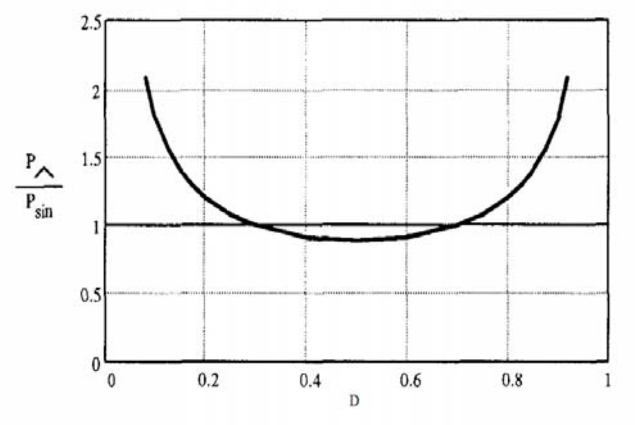

Figure 1.4 Normalized core losses of different duty cycles[20]

3. DC bias. The DC pre-magnetization will change the domain distribution. So the bias will affect the loss, though the DC flux doesn't produce loss directly. [32][33][34][35][52] Generally speaking, the core loss will increase with the increasing bias, because further magnetizing the dipoles under the pre-magnetization condition will need more energy. But the bias impact varies with materials. The core loss under certain bias can be lower than non-biased core loss, as shown in Fig.1.5. The physics behind the bias impact to the core loss is very complex. Therefore, test is the only method to accurately know the core loss under DC bias.

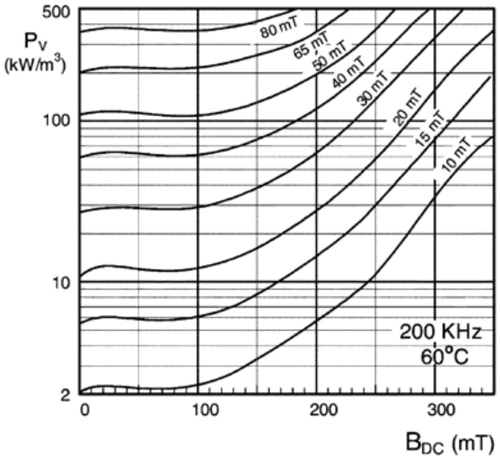

Figure 1.5 Core loss under bias [34]

4. Temperature. The core loss depends on temperature, especially for ferrites. The ferrites usually display lowest loss between 60°C to 100°C. So many literatures used a parabola to model the temperature dependence.[36][37] However, this dependence changes with excitation level. Fig.1.6(a) shows the measured core loss scale factor of 3C85, from 25°C to 100°C.[37] At different AC flux excursion, the minimum loss takes place at different temperature. What is more, the temperature dependence is also related to the test frequency, as shown in Fig.1.6(b) [29]. The parabola shape can be different when the frequency is different. As a result, the characterization of core loss is unpredictable unless the loss is measured.

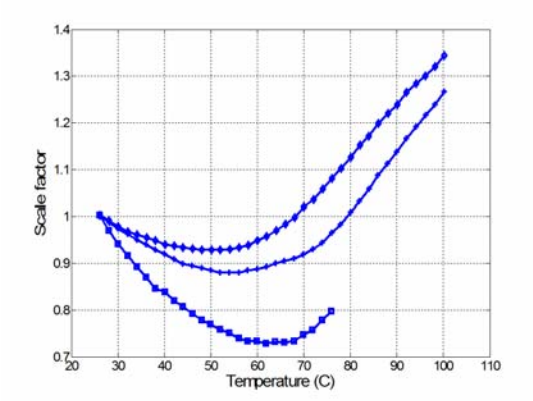

(a) Temperature dependence of core loss (3C85) [37]

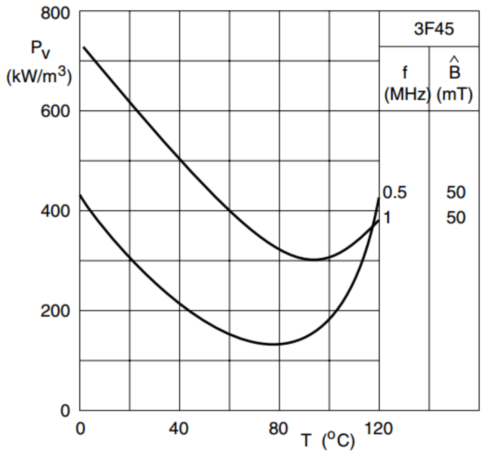

(b) Temperature dependence of core loss (3F45) [29]

Figure 1.6 Core loss vs. temperature

In conclusion, due to the nonlinearity of the core loss and the dependence on so many factors, testing is the only reliable solution to get the accurate core loss. The above factors should be considered when testing materials and designing magnetic components.

1.2 Review of the Core Loss Measurement Techniques

There are many core loss measurement methods. Basically, the methods are divided in to two categories: thermal method and the electrical method.

1.2.1 Thermal Method

This method is a pretty common way to test the core-loss. [37][38][39][40] The basic diagram is shown in Fig. 1.7. The level of liquid coolant is fixed. At the beginning, the relationship between heat and the temperature difference or its rising rate is measured with a reference heat generator (for example using a resistor with known resistance). Then replace the reference heater with the device under test (DUT). Measure the temperature differences or the rising rate and then the loss can be estimated. Stirring is necessary for the uniform temperature of the coolant.

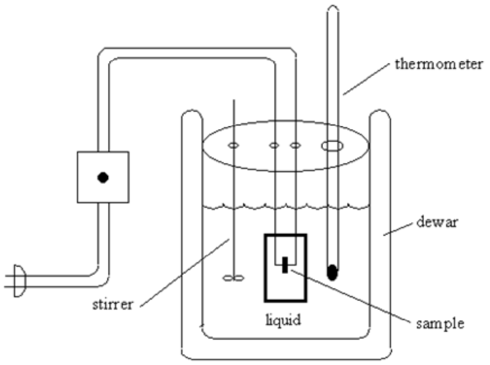

Figure 1.7 Basic calorimeter

More sophisticated calorimeter uses the circulating coolant to measure the heat. (Fig.1.8) [37] The basic idea is to put the winded core in the thermal isolated chamber, and measure the temperature difference between inlet and outlet coolant. With the temperature difference, the heat generated by the excited inductor can be calculated.

$$P = \frac{c_p \cdot m \cdot \Delta T}{dt} \tag{1.2}$$

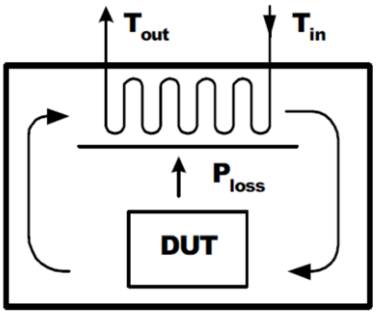

Figure 1.8 Closed type calorimeter

Another type of calorimeter method is the double-chamber calorimeter.[40] The temperature rise caused by the high frequency core loss is compared with a reference low frequency loss. This method doesn't need any complicated calibration procedure as other calorimeter methods, but its structure is more complicated.

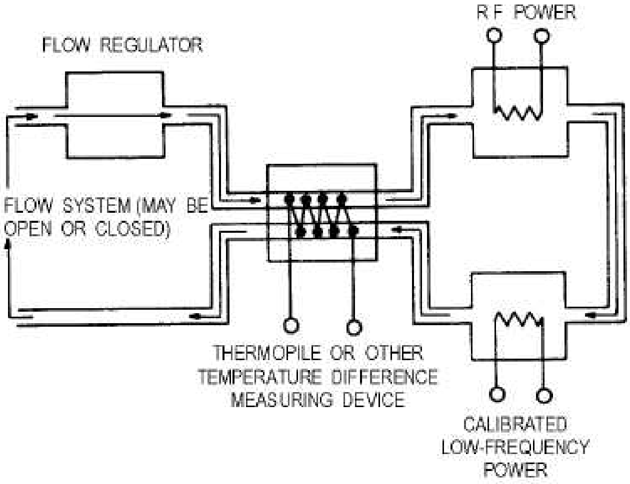

Figure 1.9 Double-chamber calorimeter

Generally speaking, the thermal approach is a pretty universal way to test the core loss. It can measure the core loss under any desired excitation or bias. However, it has the following disadvantages:

1. The measurement process is very time consuming. Each measurement needs to

wait until the temperature is stabilized. For temperature sensitive samples, the coolant temperature should return to its initial value after each measurement, which further reduces the efficiency of such tests.

2. The winding loss is not easy to compensate, especially when tested at higher frequencies. Though some literatures proposed ways to excite the core without windings [39], a sophisticated setup is required to do so.
3. The temperature rise can't be too high for some materials that are sensitive to temperature variation, like ferrites.
4. And when the loss is small and temperature rise is low, the accuracy is poor.

1.2.2 Impedance Based Method

This type of methods interprets the core loss as an equivalent resistor in parallel or in series with an ideal inductor. In circuit analysis, people usually use an equivalent resistor in connection with an ideal inductor to represent the real inductor. There are two ways of

(a) Series representation (b) Parallel representation

Figure 1.10 Two representations of inductor core loss arrange the resistor with the ideal inductor. One is in series; the other is in parallel, as shown in Fig.1.10. Once the core loss resistor is measured, the core loss can be calculated as

$$P_{core} = I_{rms}^2 R_{core} \text{ (Series) or } P_{core} = \frac{V_{rms}^2}{R_{core}} \text{ (Parallel)} \tag{1.3}$$

There are several versions of the impedance base methods for core loss measurement.[41][42][43][44]

1. Bridge method
2. I-V method
3. Auto-balanced bridge

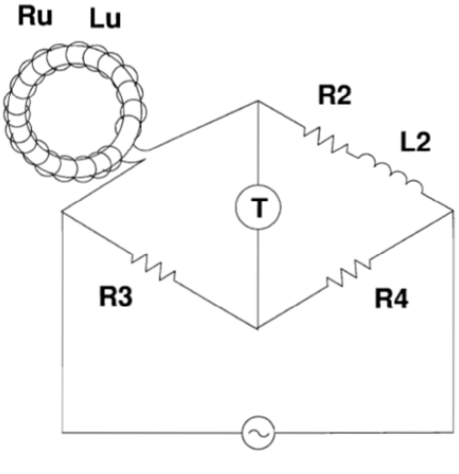

Figure 1.11 Bridge method

The balanced bridge puts an inductor made of the core under test in a bridge [41]. One branch is tuned until the detector in middle sees zero potential difference. This method is highly accurate for small signal measurement. However, the nonlinearity of the core material at high excitation condition will produce high order harmonics and the potential on the detector won't settle to zero.

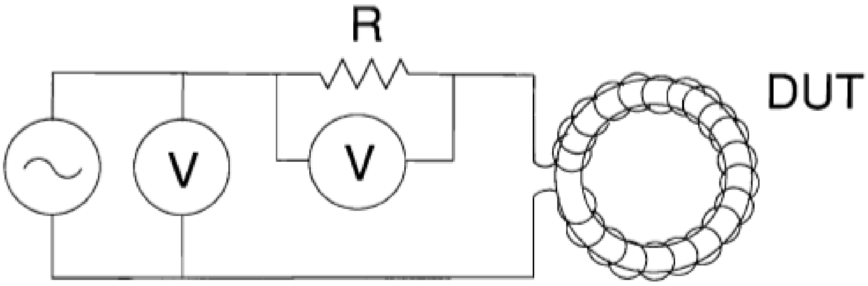

Figure 1.12 I-V method

The I-V method measures the voltage and current to get the impedance information of the device under test. To reduce the voltage drop on the sensing resistor, the current is usually measured by a current transformer. The use of current transformer limits the lower end of the measurable frequency range. So the auto balancing bridge is widely used instead.

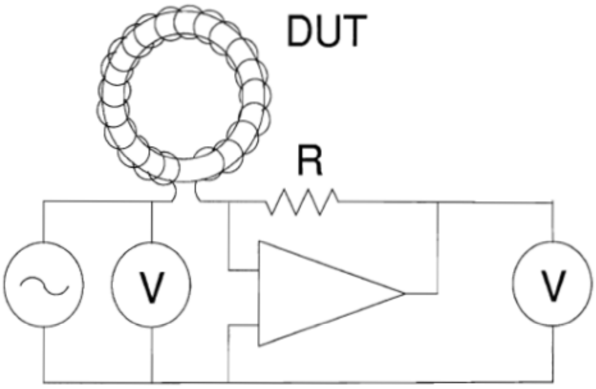

Figure 1.13 Auto-balancing bridge

The auto-balancing bridge needs a wide band operational amplifier. The measurable frequency is from tens of hertz to over 100 mega hertz. It is the most widely used method in LF and HF frequency band impedance analyzer. The commercial impedance analyzer usually can't provide enough excitation for power inductors and transformers. So Gradzki [43][44] measured the core loss by providing external amplified signal to the impedance analyzer, as shown in Fig.1.14. With this setup, the core loss can be swept over a wide frequency range and excitation levels, very conveniently and fast.

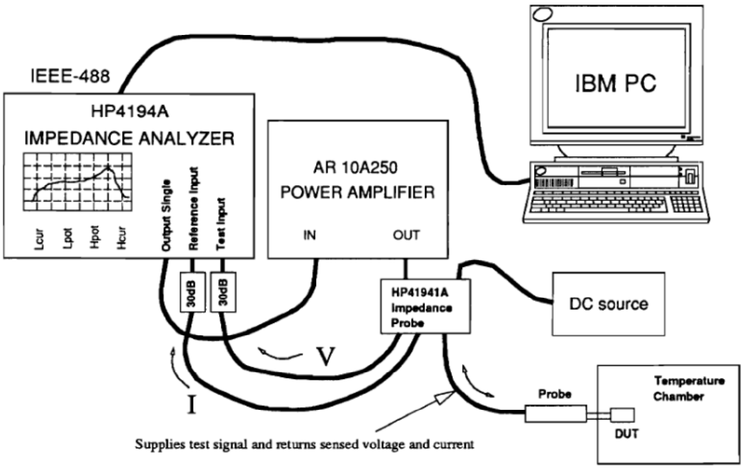

Figure 1.14 Core loss measurement setup based on impedance analyzer

Generally speaking, the impedance based methods have the advantages of simple implementation and fast data acquisition. The disadvantages are:

1. The winding loss is hard to be separated from the result. Though calibration can reduce the winding loss's impact, it is not accurate because the winding loss will be affected by the presence of the core especially at high frequency.
2. This method is sensitive to phase errors. When the quality (Q) factor is high, the real part of the impedance is hard to be accurately measured. The detailed analysis is shown in Chapter two.
3. It is limited to sinusoidal waveforms only.

1.2.3 Wattmeter Method

The Wattmeter or two-winding method is a popular method to test the core loss [45][46][47]. Its schematic is shown in Fig. 1.15.

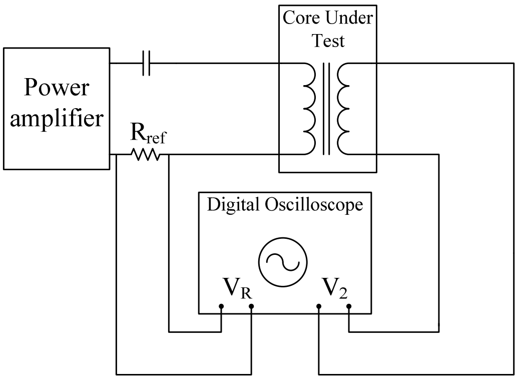

Figure 1.15 Two winding method

The core-under-test (CUT) carries two windings; the excitation winding and the sensing winding. An oscilloscope is used to measure the voltage on the sensing winding and the current through the excitation winding. Integrating the product of the voltage and current waveforms will give the loss consumed by the core-under-test. This method doesn't have significant drawbacks in principle, and it excludes the winding loss from the measured core loss, which is its biggest advantage. However, in practice it is sensitive to phase discrepancy [48][49]. Usually the phase discrepancies come from the current-sensing resistor's parasitic inductance, mismatch between probes and oscilloscope's sampling resolution. Thus it is not accurate when testing high-frequency loss, especially when the material is low permeability and low loss.

This method uses the integration between sensing winding voltage v_2 and current sensor voltage v_R to get the core loss, as shown in (1.4).

$$P_{core} = \frac{1}{TR_{ref}} \int_T v_2 v_R dt \tag{1.4}$$

In (1.2), R_{ref} is the current sensing resistance, and T is the period of the excitation frequency. Because the impedance of magnetizing inductor L_m is usually much larger than the equivalent core loss resistance R_{core}, the phase difference between v_2 and v_R is much close to 90°. This means a small phase discrepancy will lead to a significant loss error after the integration. The detailed analysis of this sensitivity is discussed in Chapter two.

There are some commercial test instruments which use this method to test the core loss with larger enough excitations. They are Clark-Hess power meter 2335A, Ferroxcube EMMA 2.1, Iwatsu SY8128/8129. The highest measurable frequency of these instruments is up to 1MHz, 3MHz and 10MHz, respectively.

The core loss under DC bias can be measured with the test circuit below[49][50]. Two identical samples are needed to reject the AC voltage on the DC source. But still, this method suffers from the sensitivity to phase errors. Although, the two winding method automatically excludes the winding loss, and can measure the core loss under sinusoidal and non-sinusoidal waveforms.

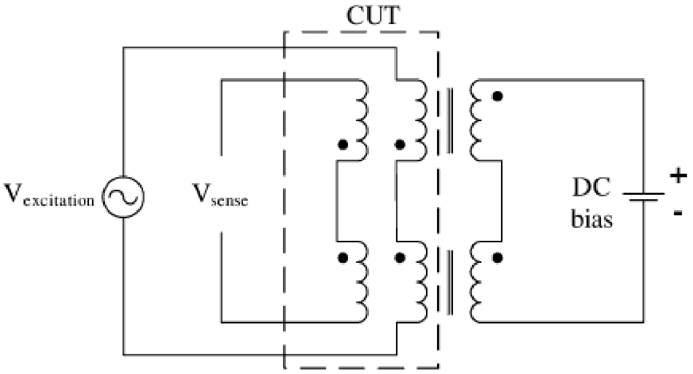

Figure 1.16 Core loss test circuit under DC bias

1.2.4 Resonant Method

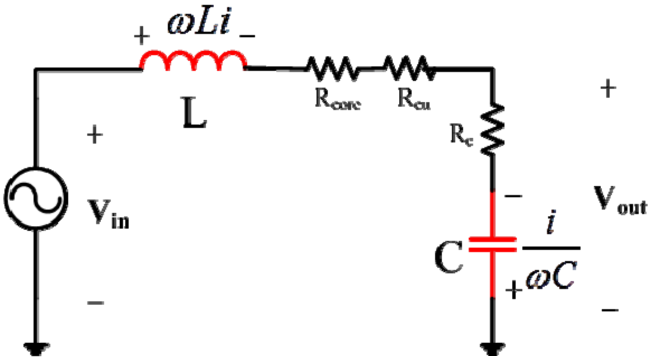

Figure 1.17 RLC method

Another method for core loss measurement is so-called R-L-C method, as shown in Fig.1.17. It connects a capacitor in series or in parallel with the inductor of the core under test[51][52]. In reference [51], the series capacitor is finely tuned to resonate with the inductor at the test frequency. Because the voltages on the inductor and capacitor cancel each other, the resistance in this RLC network can be easily measured.

$$\frac{V_{out-pk}}{V_{in-pk}} = \left| \frac{R_c + \frac{1}{j\omega C}}{R_{core} + R_{cu} + R_c} \right| \approx \frac{1}{\omega C(R_{core} + R_{cu} + R_c)} \tag{1.5}$$

After compensating the parasitic resistance, such as the winding resistance and the resonant capacitor ESR, the core loss can be calculated by knowing the core loss resistor.

$$R_{core} \approx \frac{1}{\omega C} \frac{V_{in-pk}}{V_{out-pk}} - R_{cu} - R_c \tag{1.6}$$

This method is not sensitive to phase discrepancy, because it only uses the voltage amplitude ratio to calculate loss. However, it is difficult to compensate the winding losses, which can't be estimated very accurately at higher frequencies, because the current distribution is affected by the existence of the core. When the core is of low permeability, the winding loss will be a considerably part of the total inductor loss. The compensation will then become difficult. Additionally, the resonant capacitance's value is critical; it should be the exact value that will resonate with the inductor at a given frequency. It will need extra efforts to fine tune the capacitor.

Another version of the resonant method is by putting a capacitor in parallel with the inductor or transformer [52]. The schematic is shown in Fig. 1.18. This method tests the sensing winding’s voltage and the total current of the capacitor and transformer primary inductor. When the measured voltage and current are in phase, integration of the product of the voltage and current will give the core loss. This method ignored the winding resistance’s impact to the measured loss. Careful analysis shows that the measured loss actually includes the winding loss.

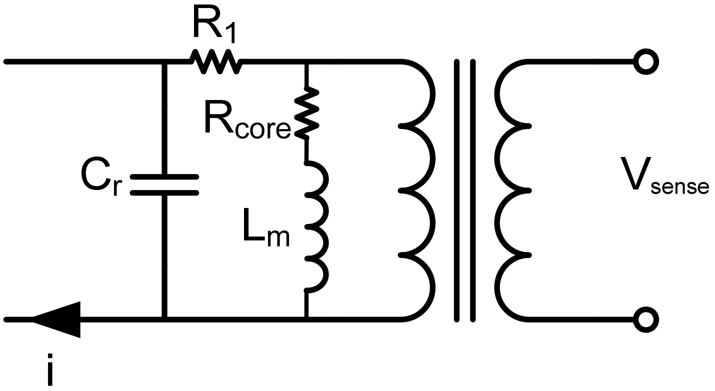

Figure 1.18 Parallel resonant method

The above two resonant methods reduce the sensitivity to phase errors, which is a problematic issue with the two-winding methods when the core sample has high Q. The disadvantages of these methods are:

1. They can't separate the winding loss from the core loss. When the core material has low permeability (e.g. smaller than 300), the winding loss can be comparable to the core loss. Careful compensation is required for such situations.
2. The winding loss is difficult to predict when operating at high frequency and adjacent to strong flux.
3. They can only measure loss for sinusoidal excitations which are not the practical in most power converters.
4. More efforts are needed to find tune the resonant capacitor value. This limits the capability of fast measurement of large amount of samples.

1.2.5 H-Bridge Method

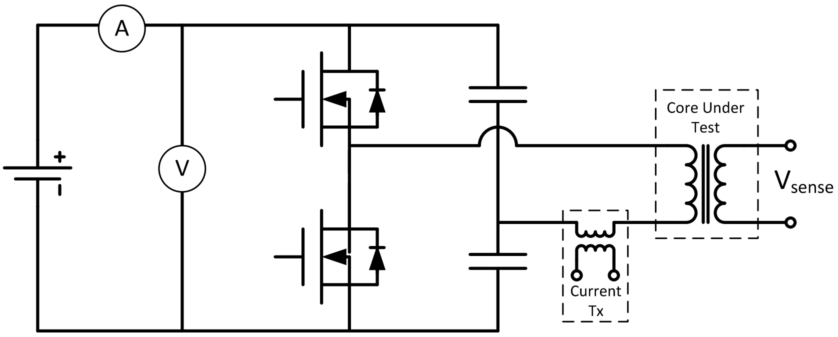

Figure 1.19 H-bridge method

The bridge type method uses the core under test as the transformer in a half or full bridge converter.[54] The secondary winding is left open for voltage sensing. The converter is optimized so that all of the switches are achieving ZVS to minimize the switching loss. In this way the converter's total loss is mainly due to the core loss. Because the converter's loss can be easily measured by testing the input DC voltage and DC current, this method is simple and fast. The disadvantages are:

1. There are numerous sources of loss that need to be compensated: devices switching loss (mainly turn-off) and conduction loss, winding conduction loss and input capacitor loss. To reduce the switches' conduction loss, larger devices with more parasitic C_{ds} should be used. On the other hand, to achieve ZVS, the current in the primary winding can't be too small. Therefore, careful trade-offs must be made between devices, current and inductance.
2. Limited waveform. It only supports rectangular voltage.
3. Limited frequency range, the highest reported frequency is below 5MHz.

In conclusion, all core loss measurements discussed so far have one or more drawbacks from the following:

a) Difficult to compensate winding loss for low permeability materials

b) Sensitive to phase errors

c) Limited waveform shapes

d) Time consuming

Thus new core loss measurement techniques are needed to address these problems.

1.3 Review of the Steinmetz Equation Based Core Loss Models for Non-sinusoidal Waveforms and DC Bias

Many engineers prefer Steinmetz equation, due to its simplicity and straightforward approach. The Steinmetz equation is derived by curve-fitting the measured data under sinusoidal excitation, as is given by

$$P_{core} = kf^{\alpha} B_m^{\beta} \tag{1.7}$$

f is the frequency, B_m is the AC flux density magnitude. The k, α and β are the parameters which keep the fitted curve match the measurement. Material manufacturers commonly provide the Pv-B graph to describe the core loss density of a material, as was shown earlier in Fig.1.3. These data are tested under sinusoidal excitation without DC bias.

For most power converters, the voltage waveforms are mostly rectangular or composite of rectangular shapes. The waveform will have an impact to the value of core loss, as proven by a lot of experimental data, as discussed before. Different waveforms give different shape of B-H loops, which represent the core loss. In many applications, there will also be DC current through the inductor, which will affect the core loss.

The best way to know the core loss under various waveforms and bias is to measure it. However, sometimes it is not practical due to limited time and capability. As a result, core loss model is a way to give engineers a quick estimation. Many modeling works try to model the core loss of different waveforms based on the sinusoidal loss. Such kind of models usually only need limited extra measurement effort other than the datasheet, so they are preferred by the engineers.

1.3.1 Modified Steinmetz Equation (MSE)

The modified Steinmetz equation was published in 1996 [20]. It assumes that the average flux changing rate dB/dt is directly related to the core loss. In one cycle, the core losses of different waveforms are the same if the AC flux swing and the average flux changing rate are the same.

If a sinusoidal wave has the same average dB/dt and the AC flux swing as the non-sinusoidal wave, the core loss is assumed to be same. To get the same average dB/dt, the sinusoidal wave's frequency has to be different with the non-sinusoidal one. Assume the sinusoidal frequency is f_{eq}. This is the equivalent sinusoidal frequency which has the same average dB/dt as the non-sinusoidal waveform.

The equivalent sinusoidal frequency can be calculated as

$$f_{eq} = \frac{2}{B_{pp}^{2}\pi^{2}} \int_{T} \left(\frac{dB}{dt}\right)^{2} dt \tag{1.8}$$

Borrowing the formula format of original Steinmetz equation, the energy loss p of every re-magnetization cycle can be determined using this equivalent frequency:

$$p = kf_{eq}^{\alpha-1} B_m^{\beta} \tag{1.9}$$

If the remagnetization is repeated with the frequency *f*, the power losses are:

$$P_v = p \times f = (kf_{eq}^{\alpha-1} B_m^{\beta}) f \tag{1.10}$$

The MSE is the first variation of the Steinmetz equation for non-sinusoidal excitations. The thinking of relating dB/dt to core loss under different waveforms inspired many more variations of the Steinmetz equations. But this method is not self-consistent. Some literatures have discussed the anomalies of MSE [22][26]. This is because of the arbitrary definition of the average dB/dt. Also, the changing α significantly impacts the calculated core loss when the equivalent frequency is high. So α's value is critical for this estimation. The definition of how to choose α is tricky.

1.3.2 Generalized Steinmetz Equation (GSE) and Improved Steinmetz Equation (iGSE)

The generalized Steinmetz equation is published in 2001[22]. It adopts a concept of instantaneous core loss. And, it uses the hypothesis that the instantaneous core loss is related to the instantaneous flux density B(t) and the instantaneous flux changing rate dB/dt. To be consistent with the original Steinmetz Equation, it assumes that one possible form for p(t) would be

$$p(t) = k_1 \left| \frac{dB}{dt} \right|^{\alpha} \left| B(t) \right|^{\beta-\alpha} \tag{1.11}$$

From this hypothesis, a formula that can be used to calculate loss for any waveform results directly:

$$P_v = \frac{1}{T}\int_T k_1 \left|\frac{dB}{dt}\right|^{\alpha} \left|B(t)\right|^{\beta-\alpha} dt \tag{1.12}$$

(1.12) is denoted as the generalized Steinmetz equation. To get consistent with Steinmetz equation, the parameter k_1 should be

$$k_1 = \frac{k}{(2\pi)^{\alpha-1}\int_0^{2\pi} \left|\cos\theta\right|^{\alpha} \left|\sin\theta\right|^{\beta-1} d\theta} \tag{1.13}$$

GSE assumes the instantaneous core loss is related to the instantaneous flux density. This is not consistent with the common knowledge. This makes it less accurate than MSE in some cases. Also, the parameter α should be smaller than β, or (1.12) will produce infinite value when β<α. But in many cases α could be larger than β.

The improved generalized Steinmetz equation (iGSE) modified the ideas of GSE in 2002.[23] Same formula was independently proposed as natural Steinmetz extension (NSE) in 2004[24]. It assumes that the instantaneous core loss is related to the amplitude of the major or minor loop in which the flux density is instantaneous. Therefore, the iGSE changed to

$$P_v = \sum_i \frac{1}{T}\int_T k_i \left|\frac{dB}{dt}\right|^{\alpha} \left|\Delta B\right|^{\beta-\alpha} dt \tag{1.14}$$

ΔB is defined as the peak-peak amplitude of the major or minor loop in which the flux density is at the instantaneous time t. The k_i is defined as (1.15).

$$k_1 = \frac{k}{(2\pi)^{\alpha-1}\int_0^{2\pi} \left|\cos\theta\right|^{\alpha} 2^{\beta-1} d\theta} \tag{1.15}$$

The iGSE has corrected the improper assumption in GSE, so it has better accuracy than GSE in many cases. Also the calculation doesn't have singularity when $\alpha>\beta$. But the method doesn't consider the magnetic relaxation effect. Similar to MSE, the iGSE is sensitive to the choice of α and β, but how choose α and β is not clearly stated. According to some literature, the iGSE is not accurate for the rectangular waveform when the duty cycle is far away from 50% duty cycle (e.g. 15% or 90%). [28]

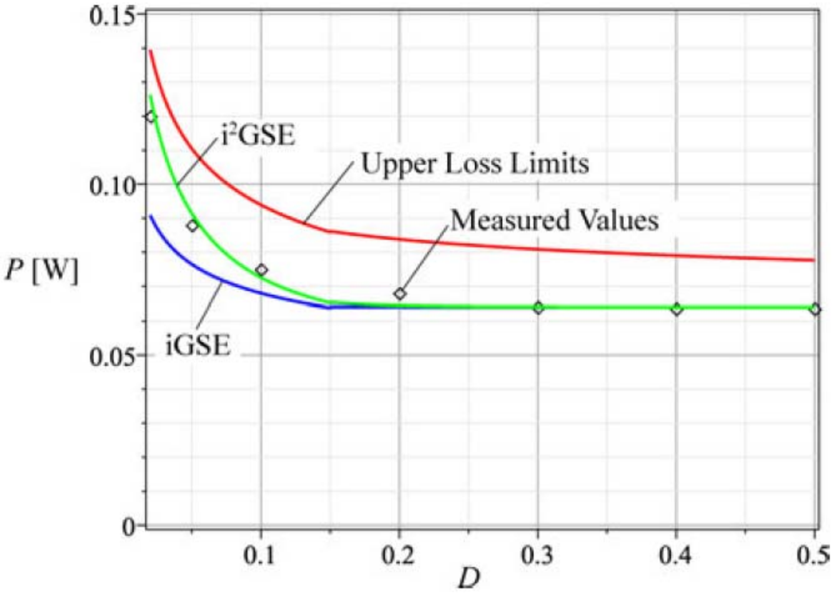

Figure 1.20 The inaccuracy of iGSE under extreme duty cycles [28]

1.3.4 I^2 Generalized Steinmetz equation (i^2GSE)

The improved-improved generalized Steinmetz equation considers the magnetic relaxation effect to the core loss[28]. Due to relaxation effect, the magnetization may change even when the applied field is constant (the magnetization is delayed). Consequently, a residual energy loss still occurs in the period of a constant applied field, as shown in the period of T_1 in Fig. 1.21.

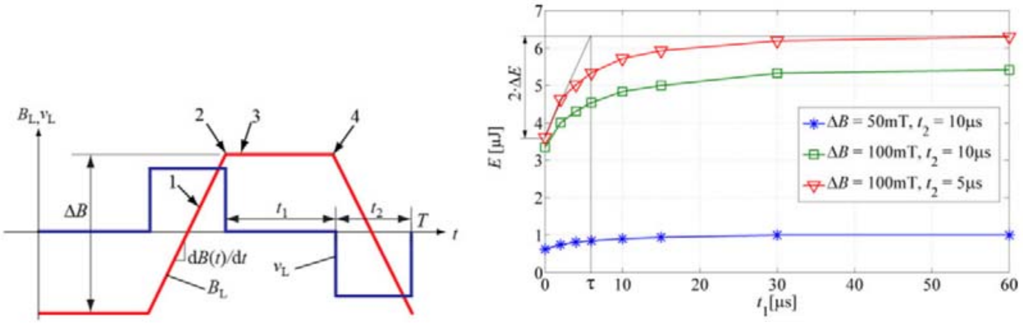

Figure 1.21 Core loss due to relaxation effect

The longer the constant field, the larger the core loss. So it modified the iGSE as

$$P_v = \frac{1}{T}\int_0^T k_i \left|\frac{dB}{dt}\right|^{\alpha} (\Delta B)^{\beta-\alpha}\, dt + \sum_{l=1}^{n} P_{rl} \tag{1.16}$$

in which,

$$P_{rl} = \frac{1}{T} k_r \left|\frac{d}{dt} B\left(t\_\right)\right|^{\alpha_r} (\Delta B)^{\beta_r} (1 - e^{-\frac{t_1}{\tau}}) \tag{1.17}$$

And $Q_{rl} = e^{-q_r\left|\frac{dB(t_+)/dt}{dB(t\_)/dt}\right|}$ (1.18)

The parameter α, β, k_i, k_r, α_r, β_r, τ, q_r are material parameters, and need excess efforts of measurement to determine the core loss. So the model is complicated for practical use.

1.3.5 Waveform-coefficient Steinmetz equation (WcSE)

The waveform-coefficient Steinmetz equation is introduced in 2006 [26]. It assumes that the core loss is related to the integration of the flux density. For a sinusoidal flux and

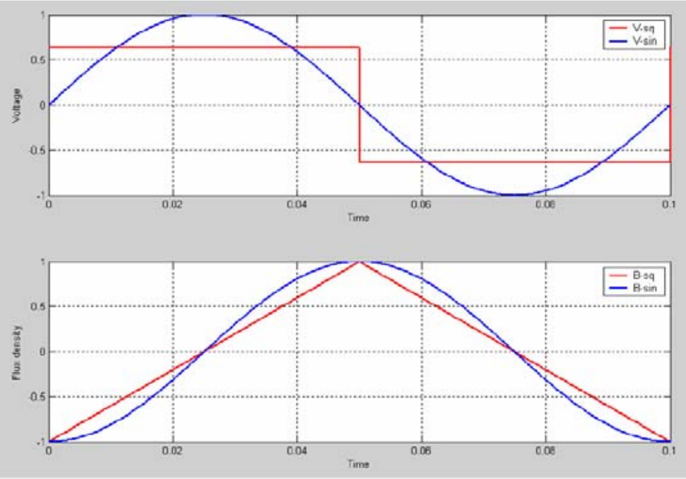

Figure 1.22 Voltage and flux of square and sinusoidal waveform

a triangular flux with the same AC flux amplitude, the ratio between the core losses of the two waveforms equals ratio of the enclosed area by the waveforms.

For sinusoidal flux, the area under a half wave is

$$W_{\sin} = \frac{1}{TB_m}\int_0^{T/2} B_m \sin(\omega t)dt = \frac{2}{\pi} \tag{1.19}$$

Similarly, the area of triangular wave is

$$W_{sq} = \frac{4}{TB_m}\int_0^{T/2} \frac{4B_m t}{T} dt = \frac{1}{2} \tag{1.20}$$

Therefore, the flux waveform coefficient (FWC) of the square voltage waveform (triangular flux waveform) can be defined as:

$$FWC_{sq} = \frac{W_{sq}}{W_{\sin}} = \frac{\pi}{4} \tag{1.21}$$

Multiply the waveform coefficient to the original Steinmetz equation, the square voltage waveform loss can be calculated.

$$P_v = \frac{\pi}{4} k f^{\alpha} B_m^{\beta} \tag{1.22}$$

This model is only limited to the square voltage waveforms, which means the duty cycle is 50%. For other duty cycles, if we still use this hypothesis that the core loss is proportional to the integration of the flux density, the result will be the same as that of 50% duty cycle, which is not correct according to measurement data. The reason is that the hypothesis counters the commonly accepted view, which assumes that the core loss is related to derivative of the flux density.

1.3.6. The Models for Core Loss under Bias Condition

Predicting the core loss of given structures under biased conditions is still a challenge, though there has been much effort spent on modeling the core losses [27][29][31]. Two such core loss models are the J-A model and Preisach Model, which can depict the hysteresis loop of the material [57][58]. This model has physical insights, but is complicated and not practical for engineering.

The physics behind the core loss under bias is very complex, so most work on modeling the impact of DC bias on core loss is based on an empirical curve-fitting methods [32][59].To model the core loss under DC bias, previous literatures usually compensates the core loss under DC bias with a factor defined as

$$P_{v\_bias} = SE \times F_{dc} \tag{1.23}$$

There are several forms of DC factor. They are usually the function of both DC and AC flux density.

$$F_{dc} = 1 + K_1 B_{dc} e^{\frac{-B_{ac}}{K_2}} \tag{1.24}$$

Or $$F_{dc} = \sqrt{\frac{K_{dc} B_{dc}}{B_m} + 1} \tag{1.25}$$

The form of DC factor multiplying the core loss without bias is a common phenomenon observed by many literatures. But the equation is over-simplified to handle most situations. In the above equations, the core loss always increases with DC bias. However, for some materials, the measured core loss does not have a simple exponential or square root relationship to DC bias. [34][35]

These models modify the parameter k to fit the measurement data under bias. Another model modifies parameter k and β to fit the measurement data [33]. This model can fit the data better, but it is much more complicated and according to the measurement, the parameter β is not strongly related to the bias field.

1.4 Review of Finite Element Analysis Approaches of Core loss

The finite element (FE) analysis of core loss is mostly used in motor applications. For power electronics, though the flux path and distribution is relatively simple, the FE core loss analysis is still necessary to predicting core loss and hot spot. Nowadays, the finite element tools have integrated the capability of calculating magnetic core loss once the users define the characteristics of the materials. There are several approaches for the finite element analysis of the core loss in the literatures and several popular FEA tools. The major difference lies in the way core loss is modeled.

1.4.1. FEA Based on Jiles-Atherton Model or Preisach Model

The Jiles-Atherton model and Preisach model are the models to plot the B-H loop. With a few parameters, these models can plot the hysteresis loop dynamically according to the transient excitation waveforms. So these models can accurately predict the core loss under various waveforms including minor loop's loss [61].These approaches require elaborated measurement to get high number of parameters, which prohibit their practical usage.

1.4.2. FEA Based on Loss Separation

As frequency further increase, the eddy current loss becomes a significant source of loss. This approach divides the core loss into three parts: hysteresis loss, classic eddy current loss and excess loss.[60] [63]

$$P_{core} = P_{hysteresis} + P_{eddy} + P_{excess}$$

A series of measurement from low to high frequency is required to determine the coefficient for each part of the loss. Therefore, a lot of measurements are required to abstract the coefficient for each part of the loss. In some popular finite element tools, like Maxwell, the simulator supports such model to define the core loss of iron based material. This approach is limited to ferromagnetic materials, but not all ferrites are covered.

1.4.3. FEA based on Imaginary Permeability

Imaginary permeability can be interpreted as another form of the material loss tangent. Some literatures reported the finite element analysis based on complex permeability.[62] The calculation process is very simple. Once the energy in the core is simulated, the loss is simply the energy times the loss tangent. Because the complex permeability is measured under small signal excitations, this approach is not suitable for large signal analysis. And when there is a bias field, the loss is even more difficult to be calculated accurately.

1.4.4. FEA Based on Steinmetz Equation

The ferrite loss is mostly modeled by Steinmetz equation. There are a few literatures introduced the approach to calculate the core loss using Steinmetz equation or its variations. The Maxwell software has very complete support for ferrite material [59]. It uses the instantaneous core loss concept as the iGSE so that the transient core loss can be calculated dynamically. Its drawback is the limited support for the permeability and core loss under DC bias. The simulator interprets the nonlinear permeability by the taking tangent of B-H curve. However, the incremental permeability is not the tangent of the large signal derived B-H curve [78]. When the core is biased close to saturation, the nonlinearity of the permeability will significantly affect the flux density and its distribution. The DC bias factor is limited to the simple form as shown in (1.25) and as discussed in 1.3.6, this form is too simple to model various materials.

1.5 Challenges

There are still several challenges for the core loss measurement, modeling and analysis. The first challenge is the measurement technique. To find a low loss material, core loss measurement technique is critical for the fundamental research. There are quite a few core loss measurement instruments or setup on the market and in the lab. But they have the problems like sensitive to phase error, hard to separate from winding loss, limited waveforms or time consuming. These limitations are mainly from measurement principle, and partially come from difficult measurement implementation.

The second challenge is the core loss model. There are numerous core loss models. These models have limited verification and comparison. Sometimes the users will be confused when choosing the correct equation or correct parameters, which will significantly affect the accuracy of the modeled loss. Some models need too many parameters other than the Steinmetz parameters, and excess measurement is required to determine the coefficient. Therefore, these models are not practical to use. Also, the impact of waveforms with the presence of DC bias doesn’t have enough experimental verification.

The third challenge is how to use the model to analyze the core loss when the core is highly biased. In many situations, the core is pushed close to saturation for soft saturation. The soft saturation is preferred in some applications (like buck POL) because it will benefit the light load efficiency. When the core is partially saturated, the nonlinearity of the core is very obvious. The saturation may cause the flux distribution hard to predict. Very few researches have discussed the core loss analysis when the core is close to saturation, and the commercial FEA tools have limited support to the core loss analysis under biased conditions.

In conclusion, the measurement technique, modeling and analysis for magnetic core loss are still challenges.

1.6 Dissertation Outline

This dissertation mainly studied the characterization method, modeling and finite analysis of the high frequency magnetic core loss.

The first chapter introduces the background of the magnetic core loss and the previous arts of testing, modeling and analyzing core loss. How to test the core loss of high frequency materials and model/analyze the core loss in the power magnetic components are the challenges for power electronics.

The second chapter proposes a new high frequency core loss measurement method for sinusoidal excitation. The conventional measurement methods have the limitations of low accuracy or time consuming. The proposed method improves the disadvantages of the standard two-winding method by adding a resonant capacitor to reduce the sensitivity to phase error, which is the detrimental error source for high frequency core loss measurement. Detailed error analysis and measurement considerations are discussed.

Chapter three proposes another core loss measurement method, for arbitrary excitation. The sinusoidal excitation is enough for material manufacturer, but not for power electronics engineers. The real working waveform is not simple sinusoidal. The two-winding method still has the problem of high sensitivity to phase error, and the method proposed in chapter two can’t work for other meaningful waveforms other than sinusoidal. Thus another testing circuit is proposed, employing the similar principle as the method in chapter two but can work with non-sinusoidal waveforms. The phase error sensitivity and measurement considerations are discussed. Based on the same idea, an inductor loss measurement method is also introduced.

In the fourth chapter, several popular non-sinusoidal waveform core loss models are compared with measurement data. Based on sufficient amount of measurement data of some commercial MnZn ferrites, a new model for rectangular AC voltage is proposed with a compact form and better accuracy. Then the DC bias impact is investigated by experiments.

Chapter five characterized low temperature co-fired ceramic ferrites which have not been full characterized for power electronics before. The incremental permeability and core loss under bias of these materials are tested. These data provide a clue for choosing proper material for different applications. According to the measurement result and the application desired property, an improved LTCC material process is proposed. The new laminated LTCC material has higher incremental permeability than the best available LTCC material on the market. A 3D integrated power module built with the new LTCC material is demonstrated and tested.

In chapter six, a finite element analysis method for inductor core loss is proposed, based on the curved fitted material characterization. A lateral flux planar inductor is used to demonstrate the method. With FEA, some interesting phenomenon of the planar inductor are observed and studied. Finally, the simulated inductor core loss is verified by experiments.

Chapter seven proposes some directions for future research that can be extended based on the study in this dissertation.

Chapter Two New High Frequency Core Loss Measurement Method for Sinusoidal Excitations

Measurement is not only a technique, but also an art. Better quantization of the core loss can help scientists and engineers optimize the materials and reduce the components loss. In addition, knowing the magnetic components provide a way to understand the loss in other components of the converter, for example the switching devices loss. Accurate measurement of the core loss is a challenge for low loss and high frequency materials and components. This chapter brings a new method to solve this problem.

2.1 Proposed Method with Capacitive Cancellation

2.1.1 Sensitivity Analysis of the Two-winding Method

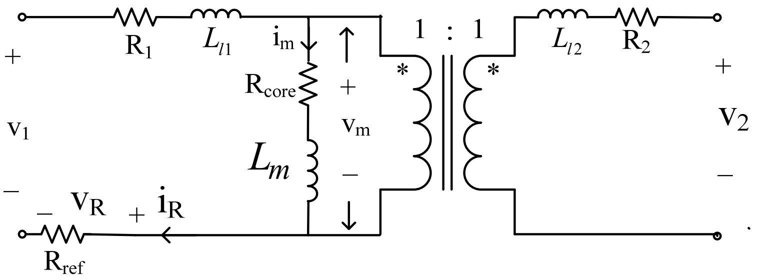

Figure 2.1 Two-winding method equivalent model

Before introducing the proposed method, it is necessary to discuss the sensitivity to phase discrepancy of the classic two-winding method in Fig. 1.15. The transformer equivalent model is in Fig. 2.1. In this model, the core loss is represented by an equivalent resistor in connection with an ideal inductor. There are two ways of arrangement the resistor. One is in series; the other is in parallel, as shown in Fig.1.10. Both of the representations can be used for core loss. Some may argue that the parallel resistor presentation is more meaningful than the series connection. This is because: First, the core loss is produced due to magnetization. And the magnetization is related to voltage, not to current. For a gapped core, no matter what the gap is, R_{core} is the same when the voltage-second is kept the same. Second, the DC flux doesn't generate core loss. However, core loss is a nonlinear phenomenon, so the linear representation only makes sense from average perspective. The resistor only stands for a loss consumption in the core, and not necessary a time-invariant value. If we look at the resistor in this way, both series and parallel resistor can be used to model the core loss. In this dissertation, either of the representations will be chosen for ease of explanation or calculation.

The two-winding method uses the integration between sensing winding voltage v_2 and current sensor voltage v_R to get the core loss, as shown in (2.1).

$$P_{core} = \frac{1}{TR_{ref}} \int_T v_2 v_R dt \tag{2.1}$$

In (2.1), R_{ref} is the current sensing resistance, and T is the period of the excitation frequency. Because the impedance of magnetizing inductor L_m is usually much larger than the equivalent core loss resistance R_{core}, the phase difference between v_2 and v_R is much close to 90°. This means a small phase discrepancy will lead to a significant loss error after the integration. Assuming the excitation is sinusoidal, the sensitivity to phase discrepancy is given by the equation:[49]

$$\Delta = \tan(\varphi_{v-i}) \times \Delta\varphi \tag{2.2}$$

where $\varphi_{v\text{-}i}$ is the phase angle between the two terms for integration: voltage and current. When the voltage and current have nearly 90° phase difference, the small phase discrepancy $\Delta\varphi$ will be amplified by $tan(\varphi_{v\text{-}i})$. The sensitivity can be further illustrated with the voltage and current phasors. When the phase angle is quite close to 90°, a little phase error will cause the voltage projection to the current phasor changes a lot. The situation is getting worse as the phase angle approaching 90°.

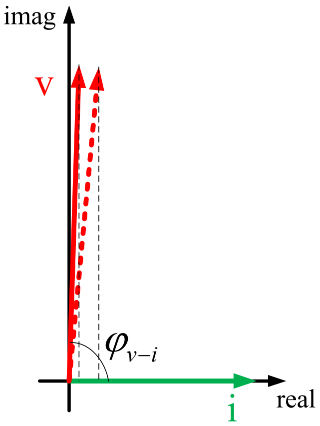

Figure 2.2 The relationship of voltage and current phasors

For low-frequency measurements, the parasitic effect in the test circuit is small, so the phase discrepancy is small and won't cause significant error. As the frequency increases, the measurement imperfections, such as the parasitic of the current sensing resistor, mismatches of two probes, the oscilloscope sample rate limitation and the parasitic coupling in the test circuit begin to emerge. For example, a 2Ω sensing resistor with 1nH will produce 0.9° phase discrepancy at 5MHz. For a 5GS/s digital oscilloscope, the minimum sampling period is 200ps, which is 0.36° at 5MHz. Fig. 2.3 shows the percentage of error that 0.1°, 1° and 10° phase discrepancy will cause at different phase angles between v_2 and i_R. We can see that at near 90°, it will produce over 100% error for

1° phase discrepancy. This type of error is more severe if the measuring frequency is high and the target material's quality factor is high. High frequency will increase the phase discrepancy; low loss will make the first term of (2.2) much closer to infinite. So this method has limitations for high frequency high quality factor core loss test.

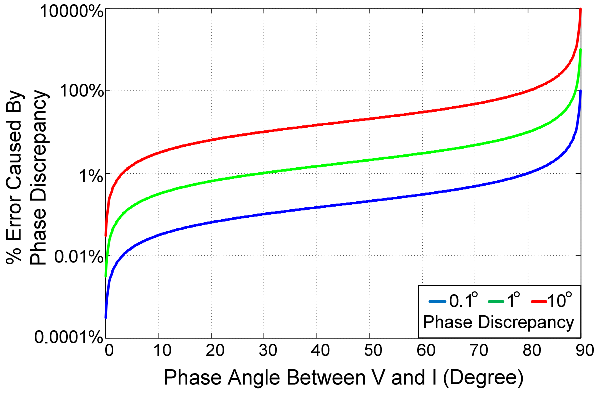

Figure 2.3 Loss error induced by phase discrepancy at different phase angles between v_2 and v_R.

2.1.2 New Method with Resonant Capacitor

To alleviate the sensitivity of the classic two-winding method as discussed in chapter one, a new method for sinusoidal excitation is proposed. The improved method is shown in Fig. 2.4. The core-under-test still carries an excitation winding and a sensing winding, whose turn ratio is 1:1. One terminal of the sensing winding is connected to the same-polarity terminal of the excitation winding. A resonant capacitor is added in series with the excitation winding at this connected terminal. Now three voltages should be monitored: sensing winding voltage v_2, the current sensor's voltage v_R, and the new voltage v_3. v_3 is the sum of sensing the winding voltage and the resonant capacitor voltage.

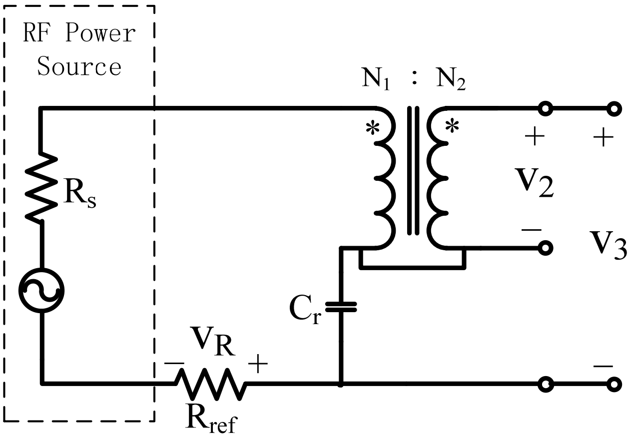

(a) Improved method

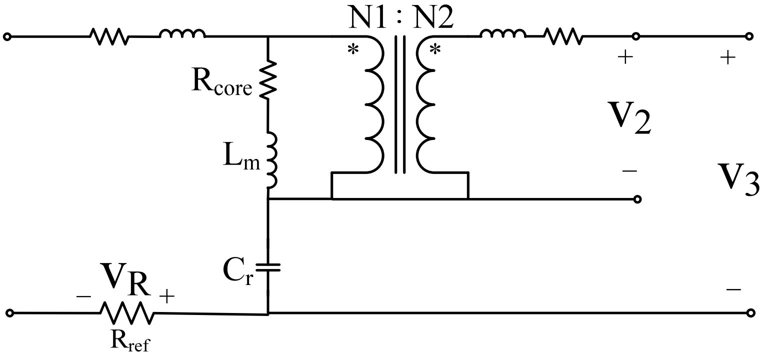

(b) Equivalent model

Figure 2.4 Proposed measurement setup and equivalent model

The purpose of adding the series resonant capacitor C_r is to cancel the voltage on the magnetizing inductor L_m. If the transformer turns ratio is 1:1, and C_r resonates with L_m at the input frequency, their voltages are the same in magnitude but 180° out of phase. As a result, v_3 is equal to the voltage on the equivalent core loss resistance R_{core}, and it is in phase with the current through excitation winding i_R. It is also in phase with the sensing resistor's voltage v_R. We know that the integration of $v_3 * v_R$ will produce the loss consumed on R_{core}, because L_m and C_r don't consume real power. As v_3 and v_R are in phase, the integration of their product is not sensitive to phase discrepancy, which is shown in Fig. 2.3. Another major advantage of this method is that it automatically excludes the winding loss from the measurement, because the secondary winding won't 'see' the voltage on the primary winding resistor.

Though C_r is used to cancel the voltage on the inductor, it doesn't have to completely cancel L_m's voltage. Fig. 2.3 shows that when the phase angle is 30°, the power error is only 1% for 1° phase discrepancy, which is sufficiently small. That means the resonant capacitor C_r could be in a relatively wide range, and it doesn't have to exactly resonate with L_m at the input frequency. It only needs to keep the phase angle between v_3 and v_R far from 90°. When the turn ratio is N_1:N_2, the C_r value should be close to:

$$C_r = \frac{N_2}{N_1 (2\pi f)^2 L_m} \tag{2.3}$$

If the turn ratio is 1:1, C_r is simply the resonant capacitor for L_m at the measuring frequency.

The phase angle between v_R and v_3 is described in (2.4).

$$\varphi_{v_3 - i_R} = \tan^{-1}\left(\frac{\omega L_m - \dfrac{N_1}{N_2 \omega C_r}}{R_{core}}\right) \tag{2.4}$$

By selecting the correct resonant capacitor C_r, we can move the phase angle between v_3 and v_R far away from 90°.

The formulas for the flux density and core loss calculation are

$$B = \frac{1}{N_2 A_e} \int_0^T v_2 dt \tag{2.5}$$

$$P_{core} = \frac{N_1}{N_2 T R_{ref}} \int_0^T v_3 v_r dt \tag{2.6}$$

where N_2 is the sensing winding turn number, T is the period of sinusoidal waveform, and R_{ref} is the current-sensing resistance, A_e is the equivalent core cross section area, V_e is the equivalent volume. If the core under test is a thin toroid core, we can assume the flux density flow in the core is almost uniform. Dividing the core loss by the equivalent volume V_e, we can obtain the core loss density at the specific flux density. Hence the core loss density is:

$$P_v = \frac{N_1}{N_2 T R_{ref} V_e} \int_0^T v_3 v_r dt \tag{2.7}$$

2.2 Measurement Considerations

Details are critical for the measurement. A careless mistake can ruin the test. The following aspects should be paid with close attention during the test.

2.2.1 Probes and Waveform acquisition

It is better to choose the same model for all three probes, so that their propagation delays are identical. Though one can compensate the propagation delay for different probes, the compensation performed at one frequency may become invalid at another frequency. To further verify that the probes match well, we can use them to test a square wave simultaneously, and check if their rising edges are close to each other in the oscilloscope. In addition, v_3 and v_R's probes should be exchanged during the test. If two groups of data are close enough, we can believe that their time delay difference won't produce significant error.

The probes should have low input impedance, which means high input impedance low capacitance. Not high enough input impedance will cause loading effect to the test circuit.

All three voltages should be measured simultaneously. v_3 cannot be obtained by measuring v_2 and v_c separately and then summing them. Because v_3's value is much smaller than that of v_2 and v_c, a small phase discrepancy in v_2 or v_c will produce significant error in v_3, so the cancelled voltage v_3 should be measured by a single probe.

Averaging acquisition can be used to reduce the noise and stabilize the result.

2.2.2 Components

It is recommended to use the bifilar winding on the core under test as shown in Fig. 2.5, though theoretically the turn ratio could be a value other than 1:1 and not in a bifilar way. It is because this will automatically guarantee the turn ratio to be 1:1, regardless of the leakage inductance. In addition, the effect of the inter-winding capacitance is minimized if using bifilar type winding when the two same-polarity terminals are connected together, which is the case in this test circuit.

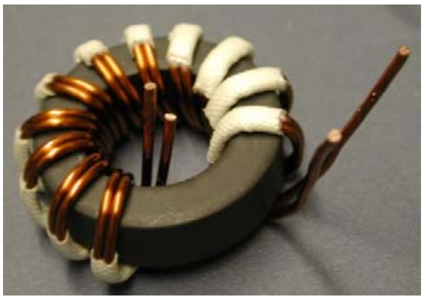

Figure 2.5 Toroid sample with bifilar winding

The current sensing component is a very critical part in the test. It is usually the major source of the phase error. There are several choices of current sensing component. The biggest concern for the current sensing part is the parasitic inductance. The resistive current sensor is a good choice for the test here.(Fig. 2.6) The coaxial current shunt has very low parasitic inductance and high bandwidth, like the SDN-10 produce by T&M Research®. But the BNC connector has the different delay from the voltage probe. Though it has superior bandwidth, it is not recommended. The surface-mount film resistors are a good choice for the current sensing resistor. It has relatively low parasitic inductance, and can be easily mounted, paralleled and changed. The parasitic inductance is larger than the coaxial shunt, but such inductance is tolerable in this core loss measurement method.

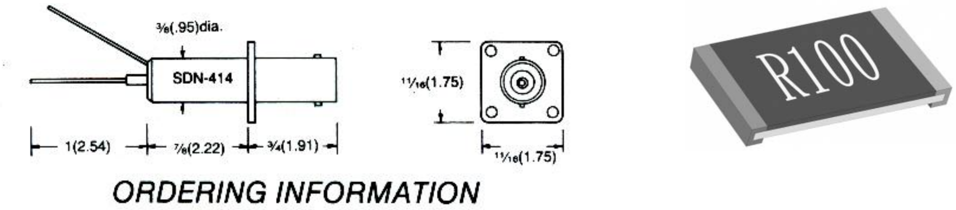

(a) current shunt (b) SM thick film resistor

Figure 2.6 Current sensors

If want to further reduce the phase discrepancy caused by its ESL, we can parallel multiple larger resistors which has the same parasitic inductance.[21] However, too many resistors in parallel will cause additional lead parasitics, so it is recommended to use only a few current-sensing resistors in parallel. Other than parasitic inductance of the resistor, the power rating should also be considered.

High quality factor capacitors are preferred for the resonant capacitor. The loss on the resonant capacitor is included in the measured loss, so high-Q capacitors like silver mica or RF porcelain capacitors are recommended (Fig. 2.7), and their loss should be compensated from the measured core loss.

(a) Silver mica capacitor (b) RF porcelain capacitor

Figure 2.7 Resonant capacitors

During the test, the magnetizing inductance tends to change due to environmental changes, such as temperature and AC flux amplitude, so the resonant capacitor may be tuned a little bit to keep the phase angle between v_3 and v_R far away from 90°. A combination of high-Q capacitor and a variable capacitor is preferable to make the fine tune easier.

2.2.3 Grounding and Some Other Circuit Considerations

The grounding can be problematic. Three probes, power amplifier and maybe other power source may need ground. If use differential probes, there will be no ground conflict between the probes and the power sources. If using passive probe which require a common ground, then the grounding should be carefully arranged. A complete schematic of the test circuit considering the grounding and impedance matching is shown in Fig. 2.8.

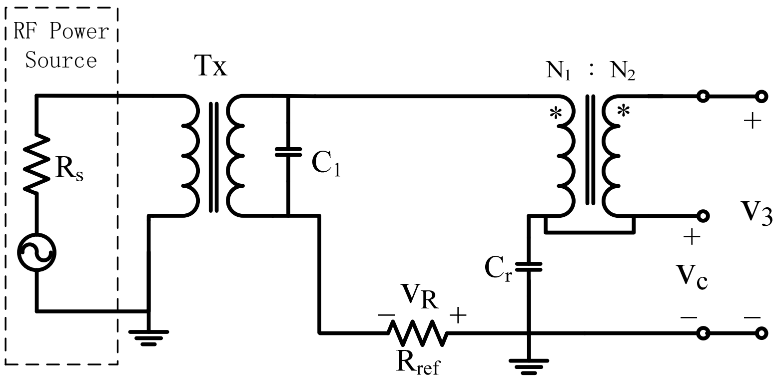

Figure 2.8 Complete test circuit

A transformer Tx is used to provide the freedom for arranging desired ground on both sides. One the right side of the transformer, the pad connecting resonant capacitor C_r and the sensing resistor R_{ref} can be assigned as the common ground for the probes. V_3 and V_R are measured, the same as the test circuit in Fig. 2.4(b). V_2 is no longer directly measured. Instead, a probe measures the voltage on the resonant capacitor, which is noted as V_c in Fig. 2.8. The voltage on the sensing winding V_2 can be got by subtracting V_c from V_3. Because this calculation is performed on a small amplitude waveform and a large amplitude waveform, the result is accurate.

C_1 is a filtering capacitor. This capacitor is used to boost the voltage swing on the core under test, and filter high frequency noise.

2.2.4 Waveform Distortion

Sometimes, when the core loss is fairly small or the core is tested under biased conditions, the voltage waveform of v_3 will not be a good sinusoidal shape. As a result, it is difficult to judge if v_3 is in phase with the v_R or not. A recommended method is to add a small delay perturbation (e.g. 1°) on one channel in the deskew tab of the scope, and compare the difference between the loss measurement result before and after the delay. If the difference is sufficiently small, we can believe the waveforms are close to in-phase and the result is accurate.

2.3 Measurement Setup and an Example

To demonstrate the method, the core loss density of the commercial magnetic material 4F1 (NiZn Ferrite) from Ferroxcube® is tested and compared with its datasheet value, which is believed to have been measured with a high-accuracy calorimetric method.

The test setup is shown in Fig. 2.9. Fig. 2.9(a) shows that a 4F1 toroid sample is wound as a transformer. The transformer's excitation winding is excited by the voltage from the power amplifier (Amplifier Research® 25A250A) driven by the 10MHz sine signal from the function generator. The core under test is immersed in the oil bath on a hot plate, and its temperature is supervised by the thermal coupler and controlled to be 100°C. The waveform from the digital oscilloscope is shown in Fig. 2.10. We can see that v_3 is 20.2° leading v_R, which means their phase angle is far away from 90°. So an integration of v_3 and v_R will have less phase-induced error. The measured core loss is compared with the datasheet result in Fig. 2.11, which shows that they are in good agreement. The results of measuring with the conventional method using the same equipment are also displayed; these results are much too high and are not accurate.

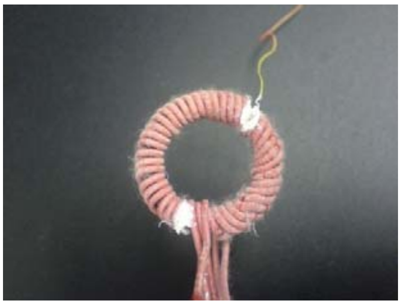

(a) Core under test (NiZn ferrite)

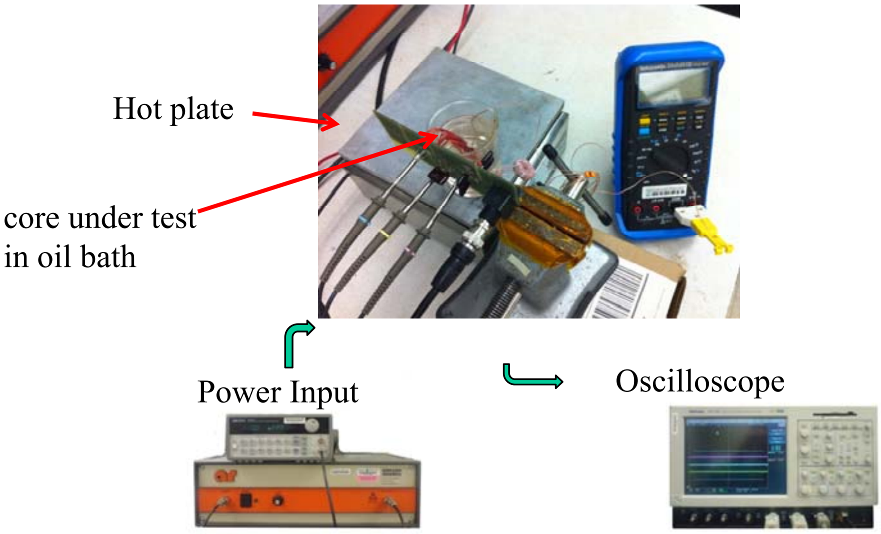

(b) Test setup

Figure 2.9 An improved core loss measurement setup

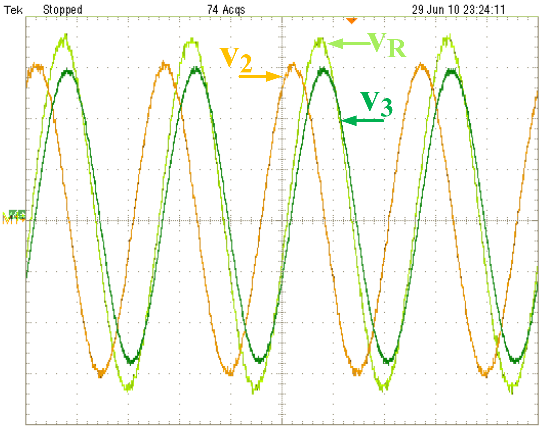

Figure 2.10 Working waveform in the improved method (10MHz)

V_2 in 10V/div, V_r in 100mV/div, V_3 in 2V/div.

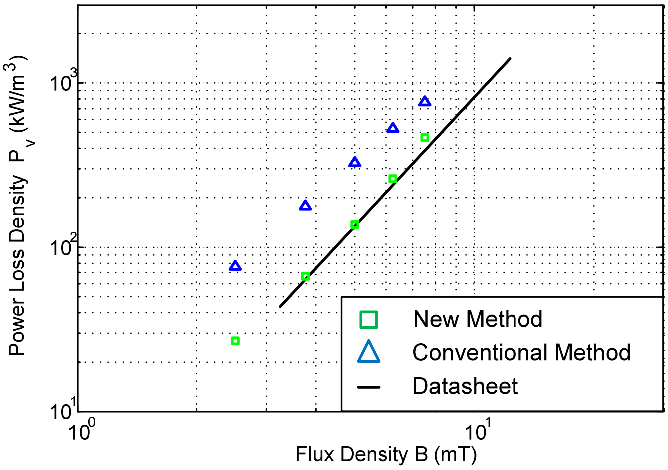

Figure 2.11 Conventional and proposed methods compared with datasheet

2.4 Error Analysis

The error sources in the above measurement example include phase discrepancy, resonant capacitor ESR and parasitic capacitances.

2.4.1 Phase Discrepancy

As stated above, the phase error is greatly reduced to below 5% if we properly adjust the phase angle. From Fig. 2.3, we know if the phase discrepancy is below 1°, a 20° phase angle between v_3 and v_R is enough to guarantee <1% loss error. Thus this part of the error is not a significant contributor to overall error.

2.4.2 Error Caused by ESR of the Resonant Capacitor

The capacitor will introduce ESR into the measurement. To estimate and compensate this error, the equivalent core loss resistance needs to be calculated. The measured power loss in previous section is converted into the equivalent core loss resistance R_{core}, as shown in Fig. 2.12. From Fig. 2.12, we can see that R_{core} is around 1Ω, and varies with the flux density from 0.8Ω to 1.6Ω.

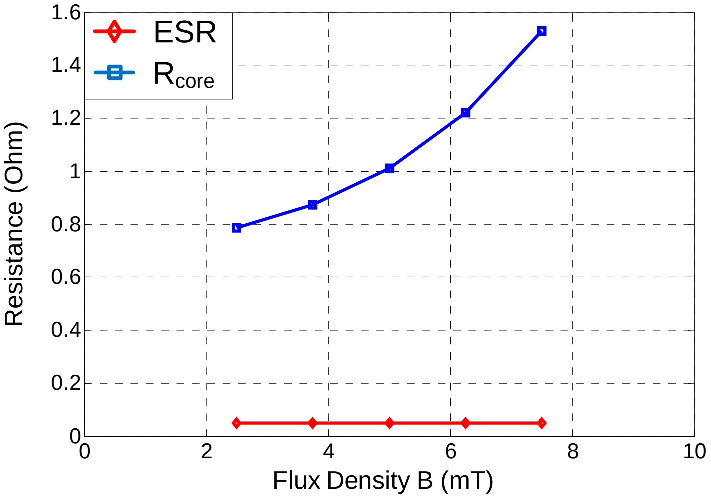

Figure 2.12 Resonant capacitor ESR compared with R_{core}

In the measurement, we use two parallel 68pF mica capacitors to resonate with the magnetizing inductor. The total ESR is about 50mΩ, and is compared with R_{core} in Fig.

2.12. The loss error caused by ESR ranges from 3.3% to 6.4%, and this part of error can be compensated accordingly.

2.4.3 Error Caused by Parasitic Capacitances

Because the probe's impedance is not infinite and the transformer has intra-winding parasitic capacitances, there will be a small current flowing through the sensing winding, which will invalidate the assumption that the sensing winding is open when the parasitic capacitance is too big. The simplified equivalent circuit, including the parasitic capacitance, is shown in Fig. 2.13. Though v_3 and v_R's probes also have parasitic capacitances, their loading effect is much smaller than v_2's probe. This is because the magnitude of v_3 and v_R are much smaller than v_2, so the currents flowing through their probes' input capacitors are much smaller than v_2's probe. Thus when we analyze the loading effect of v_2's probe, we can safely assume the other two probes are open.

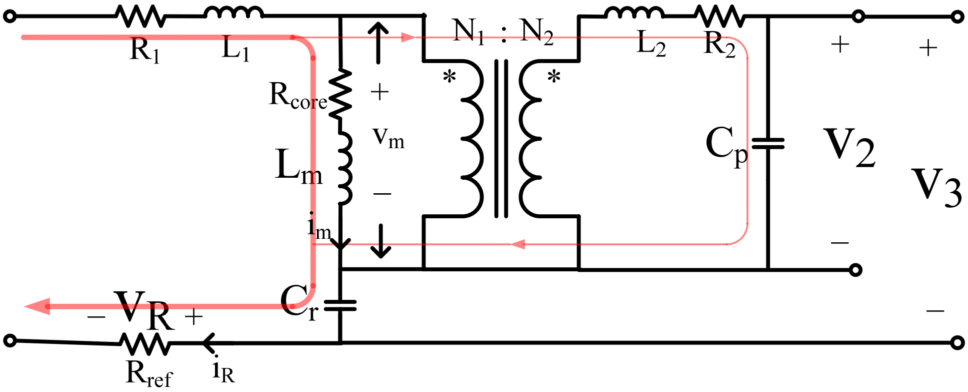

Figure 2.13 Simplified circuit of parallel parasitic capacitance

In Fig. 2.13, C_p is the total parasitic capacitance in parallel, including the probe's input capacitor and the winding parasitic capacitances from both windings. As a result, a small current flows through C_p. This current will then induce voltage drop on the sensing winding's leakage inductor L_2 and winding resistor R_2, which means v_2 will be different than the voltage on L_m and R_{core}, which is v_m. When the measurement frequency is high, this difference cannot be ignored. Furthermore, the current measured by current sensor i_R is not equal to the current flow through magnetizing inductor i_m.

To quantify the error caused by the parallel parasitic capacitance, we assume

$$R_{core} << \omega L_m, \tag{2.8}$$

$$\omega L_m << 1/\omega C_p, \tag{2.9}$$

$$R_1,\ R_2,\ \omega L_1, L_2 << 1/\omega C_p. \tag{2.10}$$

Under these assumptions, we can approximate the error percentage as

$$\begin{aligned}\Delta &= \frac{P_{measured} - P_{actual}}{P_{actual}} = \frac{\int (v_3 i_R - v_m i_m)dt}{\int v_m i_m dt} \\ &\approx \frac{R_2 \omega^2 L_m C_p}{R_{core}} + \omega^2 L_2 C_p\end{aligned} \tag{2.11}$$

The derivation of (2.11) is complicated, so the final approximated equation is given directly here. Simulation proves that this approximated equation can fairly accurately estimate the error caused by C_p if the assumptions in (2.8), (2.9), and (2.10) are true.

For the measurement setup in the previous section, $C_p \approx 10\text{pF}$, $L_m \approx 2\mu\text{H}$, $L_2 \approx 200\text{nH}$, $R_2 \approx 0.2\Omega$, and $\omega = 2\pi \times 10\text{MHz}$. With the value of R_{core} in Fig. 2.12, we can calculate the error percentage for the example in above.

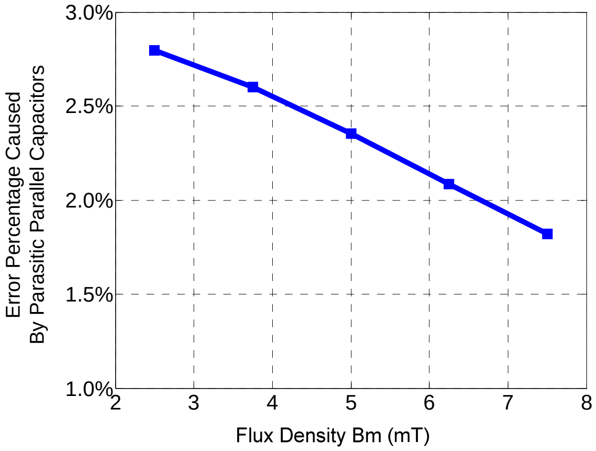

Figure 2.14 Error caused by the parallel parasitic capacitances

From (2.11), we know that this error increases very fast as the frequency goes up. To reduce this error, the sensing winding's resistance R_2 should be small, the ratio of L_m to R_{core} should be small (which means the magnetizing inductor's quality factor is low, and this is predetermined by the core material), and parasitic capacitance C_p is small. Thus the parasitic capacitance of the transformer should be well-controlled, and a low-input-capacitance probe is preferred. In addition, to reduce the loading effect of the probe, an improved version of the proposed method is shown in Fig. 2.15. It is actually the same as the circuit in Fig. 2.8. By measuring this way, the current through the sensing winding is much reduced, and C_{probe} is merged into the resonant capacitance C_r. So this circuit is recommended not only for single-ended probe, but also for differential probes.

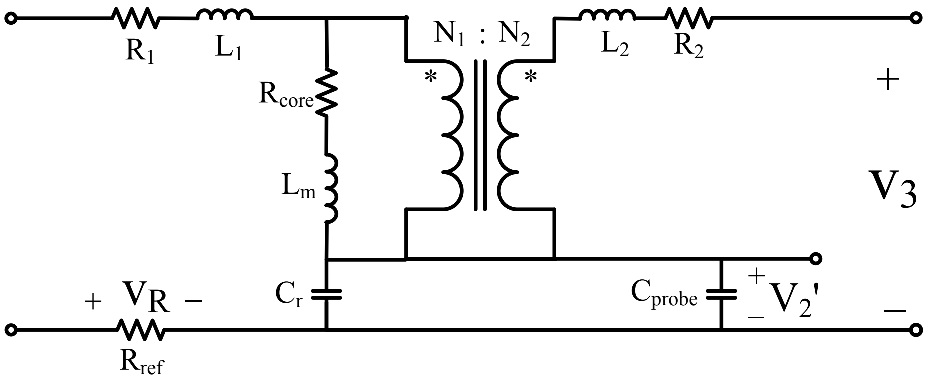

Figure 2.15 Improved version of proposed method

Another parasitic capacitance is the transformer inter-winding capacitance. Figure 2.16 shows a simplified transformer model with inter-winding capacitor C_{ww}. If there is a voltage difference between the two windings, there will be a small current flow through C_{ww} and the sensing winding. So when the two windings are bifilar windings, the current flow through C_{ww} is at its minimum.

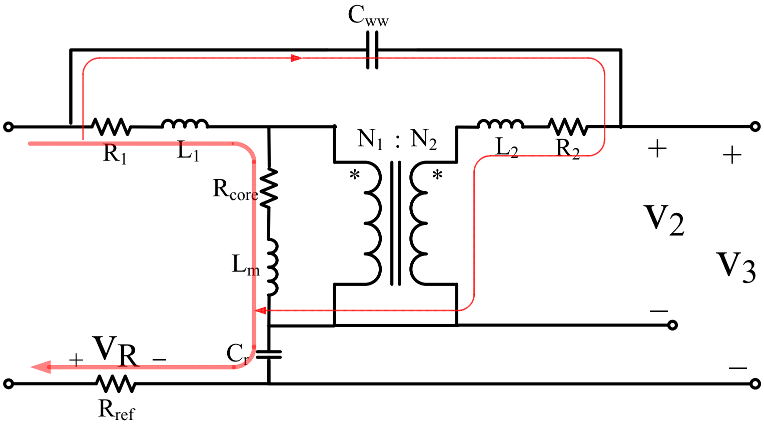

Figure 2.16 Equivalent circuit model with transformer inter-winding capacitor

Assuming

$R_{core} << \omega L_m,$ (2.12)

$\omega L_m << 1/\omega C_{ww},$ (2.13)

$$R_1,\ R_2,\ \omega L_1, L_2 << 1/\omega C_{ww}, \tag{2.14}$$

the error caused by the inter-winding capacitance can be simplified as

$$\begin{aligned}\Delta &= \frac{P_{measured} - P_{actual}}{P_{actual}} = \frac{\int (v_3 i_R - v_m i_m)dt}{\int v_m i_m dt} \\ &\approx \Big(\frac{-N_1^2 R_1 \omega L_2 - N_1^2 R_2 \omega L_1 - N_1^2 R_2 \omega L_m - N_1^2 R_{core} \omega L_2 + N_1 N_2 R_1 \omega L_m + N_1 N_2 R_2 \omega L_m}{N_1 N_2 R_{core}} + \\ &\quad \frac{-N_1 N_2 R_{core} \omega L_1 + N_1 N_2 R_{core} \omega L_2 - N_2^2 R_1 \omega L_m + N_2^2 R_{core} \omega L_1}{N_1 N_2 R_{core}}\Big)\omega C_{ww}\end{aligned} \tag{2.15}$$

If the windings are wound in the bifilar way, $N_1=N_2$, and the equation is simplified to

$$\Delta \approx -\frac{R_1 \omega L_2 + R_2 \omega L_1}{R_{core}} \omega C_{ww} \tag{2.16}$$

For the measurement in the example, $R_1 \approx R_2 \approx 0.2\Omega$, $L_1 \approx L_2 \approx 200$nH, $C_{ww} \approx 20$pF, $\omega = 2\pi \times 10$MHz, the turns ratio is 1:1, the equivalent core loss resistance is as in Fig. 2.12, and the measurement error is plotted in Fig. 2.17.

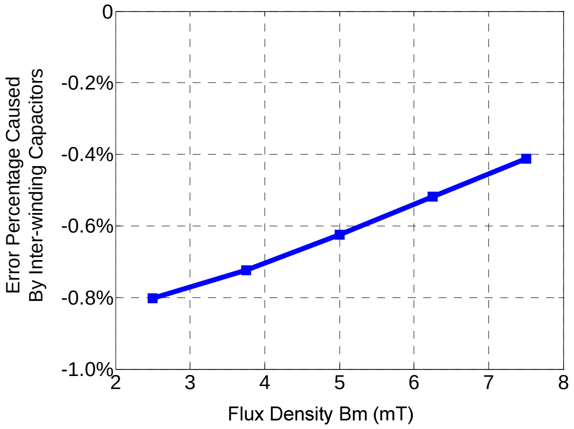

Figure 2.17 Error caused by parasitic inter-winding capacitance of the transformer

2.4.4 Other Error Sources

There are some additional error sources, such as the oscilloscope’s magnitude error, interconnect resistance, current-sensing resistance variation, and noise. Because these errors are small and don’t increase significantly with frequency, the errors from these sources are well under control.

2.5 Core Loss Measurement under DC Bias Condition

In many situations, the core loss under DC bias condition is needed. To test the properties of the materials at certain DC pre-magnetization conditions, one solution is to add a third winding to the core and a DC current source is used to control the DC current through this additional winding, as shown in Fig.2.18. According to *Ampere's Law*, the DC magnetic field strength H_{dc} can be calculated as

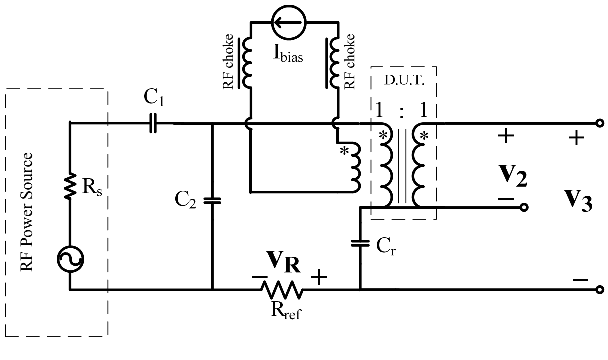

Figure 2.18 Measurement with DC pre-magnetization

$$H_{dc} = \frac{NI_{bias}}{l_m} \tag{2.17}$$

I_{bias} is the DC current through the third winding; N is the turn number of the third winding, l_m is the magnetic path length of the sample.

Figure 2.19 Choke inductor with stacked cores

To block the AC signal that may flow into the third winding, two large choke inductors are connected in series with the DC winding and the DC current source. Because the third winding is coupled with the other two windings, the choke inductors and the DC source are in parallel with the transformer's magnetizing inductor. If the impedance of the choke inductor and the non-ideal current source is not big enough, considerable AC current will flow through this branch, and the current measured by current sensing resistor is no longer the current flow through the magnetizing inductor of the core under test. In order to prevent this error, the total inductance of the two chokes should be kept at least 100 times larger than the magnetizing inductance of the transformer, and high frequency magnetic material should be used for these chock inductors. So that only negligible amount of AC current will flow through the third winding, and it won't affect the measured result much. An easy way to check if the DC winding lead to large measurement error is to compare the result of two cases: one is leaving the third winding open, the other is connecting the third winding with choke and current source but set the DC current to 0 A. If the two results have little difference, we are assured that the loss error caused by this path is negligible.

Another consideration about the DC winding path is when a high DC current flow through the winding, the choke inductors might be close to saturation and their inductance may drop and lose the AC blocking capability. In order to increase the saturation current of the choke inductors, stacked toroid cores with less turns number is used, as shown in Fig.2.19. With less turns number, the core will be less vulnerable to saturation at certain DC current. With stacked cores, the cross section area of the inductor is increased, so the inductance will be raised even though the turn number is reduced.

For some situations when the magnetizing inductance value of the core under test is high, it is hard to find a high frequency choke inductor which keeps high inductance at high current level. Then measurement circuit in Fig.2.18 will inevitably bring considerable error to the result. To solve this problem, the method in Fig.2.18 is modified to the method in Fig.2.20, using the differential voltage cancellation technique in [49][50] In the modified method, two identical samples are used and each carries three windings, for excitation, sensing and DC bias respectively. The turn numbers of the two transformers are the same. Two winded samples are connected in series, primary with primary, secondary with secondary and third with third. Because the turn number and the DC current are the same, two cores are working at the same DC pre-magnetization condition. The polarity of the windings should be carefully arranged according to the schematic in Fig.2.20. The polarity of the primary and secondary are the same for both transformers. The polarity of the one transformer’s DC bias winding is set to be the same, the other's is set to be opposite. The AC voltages on the DC bias windings of the two transformers are similar in magnitude but out-of-phase. So the AC voltage saw by chokes and DC current source are very small. This configuration reduces the AC voltage on the current source and RF chokes, so less AC current will flow through the third winding, and the DC winding will have minimum effect to the measurement accuracy.

Due to the polarity, the voltage v_2 is the sum of the voltage on the magnetizing inductors of the two transformers. Integrating the product of v_3 and v_R will give the total core loss of the two samples. Because the working conditions of the two samples are the same, dividing the loss by two will produce the core loss consumed by each core.

Under highly saturated region, the permeability is not piece-wise linear. As a result, measurement waveforms will have a small high order harmonics. Even though v_2 and v_R look like sinusoidal because the fundamental still dominates, v_3 will see a strong second-order harmonics since the fundamental has already been largely cancelled. Under such situation, observing the waveforms to judge their phase relationship will not be practical. One solution is that using the deskew tool of the scope. Purposely add a small phase error in one channel, for example 1° phase error in the v_R's channel, and record the core loss before and after this change. If the core loss change is within certain range, say 5%, we know the result is less sensitive to phase error.

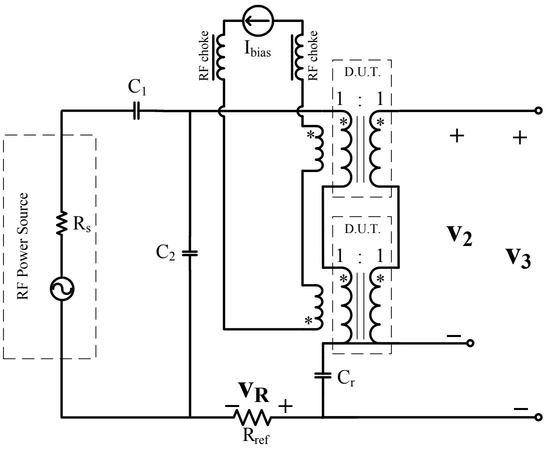

Figure 2.20 Improved scheme with two identical samples

With the waveform measurement of v_2, v_3 and v_R, the flux density B, relative incremental permeability $\mu_{\Delta r}$ and the corresponding core loss density P_v at certain H_{dc} can be calculated as

$$B = \frac{1}{2NA_e}\int_T v_2(t)dt \tag{2.18}$$

$$\mu_{\Delta r} = \frac{l_e R_{ref}}{\mu_0 N^2 A_e \omega}\frac{|V_{2\max}|}{|V_{R\max}|} \tag{2.19}$$

$$P_v = \frac{1}{2A_e l_e R_{ref} T}\int_T v_3(t)v_R(t)dt \tag{2.20}$$

N is the turn number of the primary or the secondary winding. A_e is the cross section of the thin toroid core, l_e is the magnetic path length of the core. R_{ref} is the current sensing resistance, ω is the excitation angular frequency, T is the excitation period.

The measurement setup is shown in Fig. 2.21. The sinusoidal excitation signal is generated by the power amplifier 1000L from Amplifier Research®. Three differential probes P6251 from Tektronix® are used due its high bandwidth and low parasitics. The digital oscilloscope TDS7054 is used to monitor the waveform and directly calculate the loss from measured waveforms. The core under test is immersed in oil bath and the temperature is controlled at 100°C.

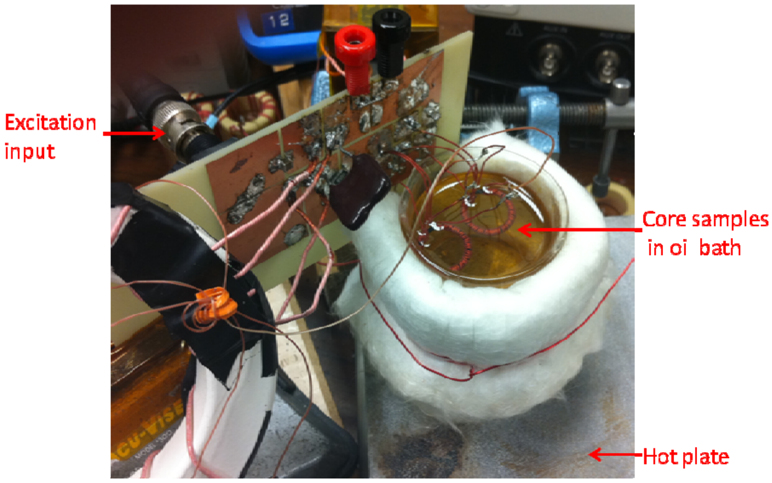

Figure 2.21 Measurement setup

2.6 Verification of the Measurement Setup Using a Simple Calorimeter

To verify the setup, a simple calorimeter is built. The principle is shown in Fig. 1.7. The setup is shown in Fig. 2.22. There is certain amount of thermal liquid in a thermal pot. The reference resistor or the core under test with windings is immersed in the liquid. A thermal coupler is used to test the temperature rise of the liquid. All of the wires are through a hole on the cap of the thermal pot. The hole is sealed with silica gel.

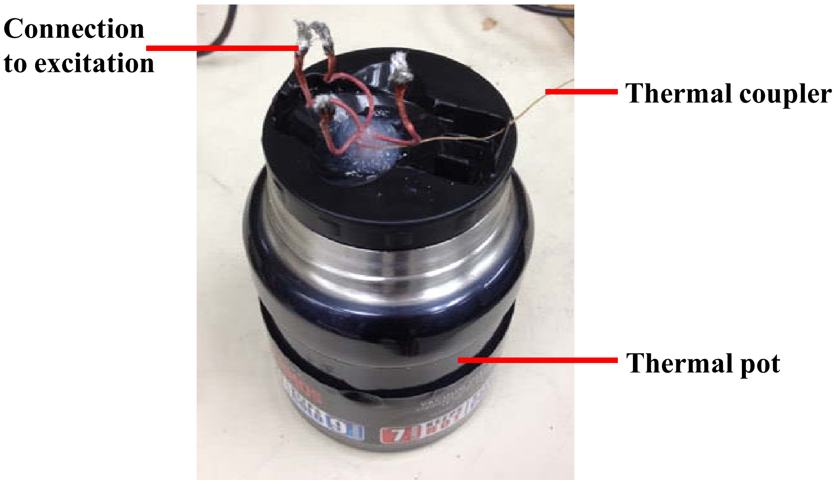

Figure 2.22 Simple calorimeter

At the beginning, the reference resistor is heated by a fixed amount of DC current. The power dissipation should be large enough so that the temperature has noticeable change. Stirring or gentle shaking is necessary to make sure the temperature is uniform in the liquid. After a fixed period of time, like ten minutes, stop the excitation. And read the temperature rise in the pot. Repeating the process for different power loss, one can plot the relationship between the power loss and temperature rise.

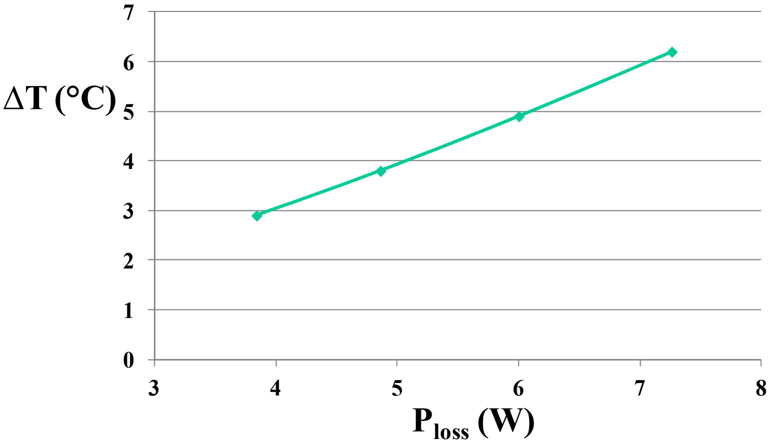

Figure 2.23 Temperature rise vs. power loss

As shown in Fig. 2.23, the loss and temperature rise is in a linear relationship. After got this relationship, replace the reference resistor by core under test with windings. Since here we want to verify the core loss test setup, the core is winded as a transformer. To reduce the winding loss's impact, a high permeability material is used (3F3) so that the AC current through the winding is very small. Excite the core and measure the power loss by using the proposed resonant method. Keep the measured loss at a fix value. After ten minutes, stop the excitation and read the temperature rise in the pot. With the temperature rise, we can read the power loss from Fig. 2.24. Comparing the power loss predicted by calorimeter and the direct measured loss by the electrical method, I find the result matches pretty well, as shown in the figure below. So the measurement setup is verified by the calorimeter method.

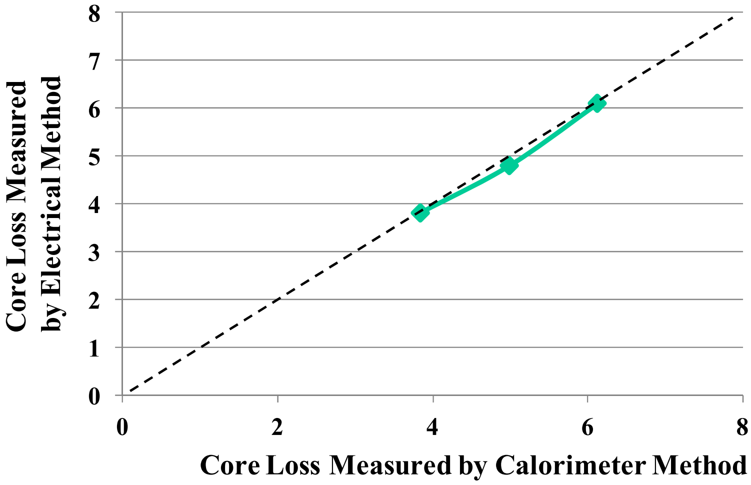

Figure 2.24 Comparison of two methods

Chapter Three New High Frequency Core Loss Measurement Method for Non-sinusoidal Excitations

In previous chapter, the high frequency core loss measurement for sinusoidal excitation is tackled. But it is not suitable for non-sinusoidal waveform measurement. The core loss under other waveforms, particularly rectangular waveforms, is interesting for pulse-width modulation (PWM) converters. However, precise measurement is difficult with classic two-winding methods for high frequency low loss magnetic components, because of the sensitivity to phase discrepancy. In this chapter, a new method is proposed for high frequency core loss measurement under non-sinusoidal excitations.

3.1 The Sensitivity to Phase Discrepancy for Rectangular AC Voltage

The classic two-winding method can measure the sinusoidal waveform's core loss, and it can measure the core loss under other kinds of waveforms as well, like rectangular wave. The circuit of the two-winding method is shown in Fig. 3.1.

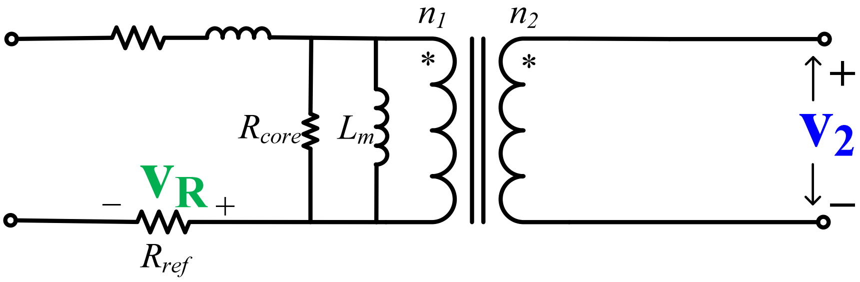

Figure 3.1 Two-winding method

When a rectangular voltage is added on the transformer primary side, the measured waveform on 3F3 toroid sample is drawn in Fig. 3.2(a). The current through the primary side ideally is a triangular wave as the dashed waveform in Fig.3.2 (b). Due to core loss, the current waveforms will looks like a step wave plus triangular wave, as shown in Fig.3.2. The small current step i_{pp} is caused by the core loss. Usually, this current step change is not noticeable for low permeability or gapped core.

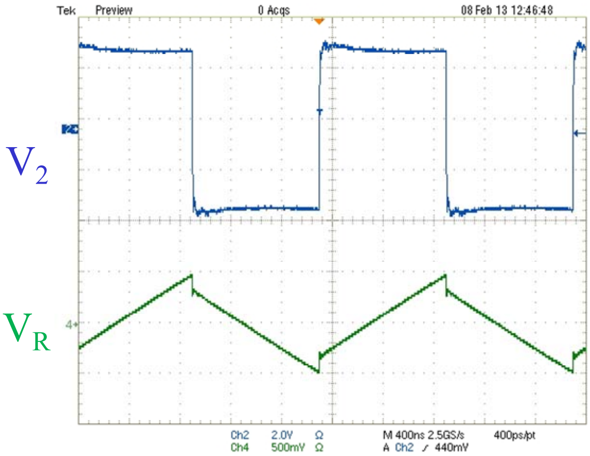

(a) Measured waveforms

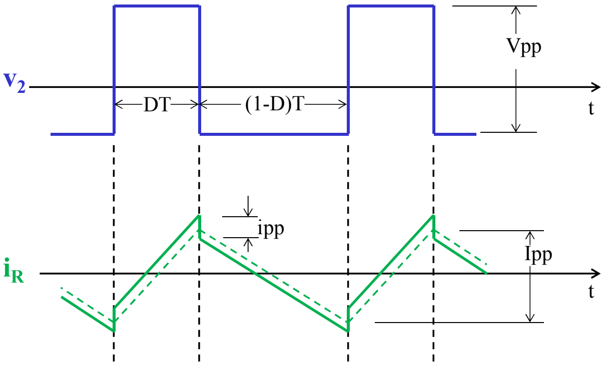

(b) Waveforms with annotations

Figure 3.2 Waveform measured by two-winding method

With the noted value in Fig. 3.2 (b), the core loss can be calculated as

$$P_{core} = D(1-D)^2 V_{pp} I_{pp} + (1-D)D^2 V_{pp} I_{pp} = D(1-D)V_{pp} I_{pp} \tag{3.1}$$

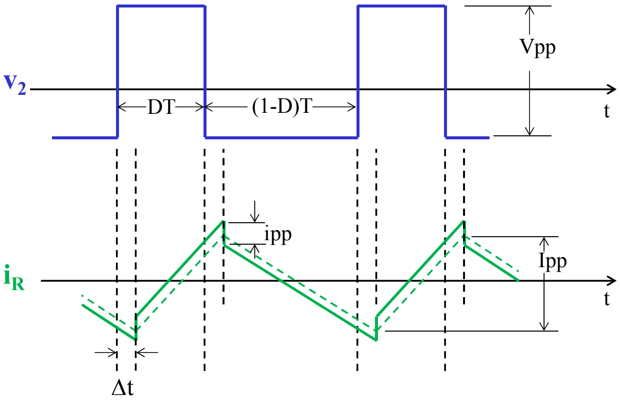

Figure 3.3 Waveforms with a small time delay

When there is a small phase discrepancy in the test, like the probe delay difference or the current sensing phase error, there will be a small time delay. Assume the measured current is delayed by a small time interval Δt, as shown in Fig.3.3.

The error caused by the small time delay is

$$\Delta P_{core} = \frac{V_{pp}(I_{pp} - i_{pp})\Delta t}{T} \tag{3.2}$$

So the error percentage due to the time delay is calculated as

$$\Delta = \frac{\Delta P_{core}}{P_{core}} = \frac{I_{pp} - i_{pp}}{D(1-D)i_{pp}} \cdot \frac{\Delta t}{T} \tag{3.3}$$

We can see that when $I_{pp} >> i_{pp}$, which means the core is low loss or high Q, the value of the first term in (3.3) will be very big. Then this error will be amplified. Also when the frequency is high, the period T is becoming smaller, which will also raise the error. If we assume the time delay is 1° of the measurement period, the relationship between the core loss measurement error and the ratio of I_{pp}/i_{pp} is plotted in the figure below.

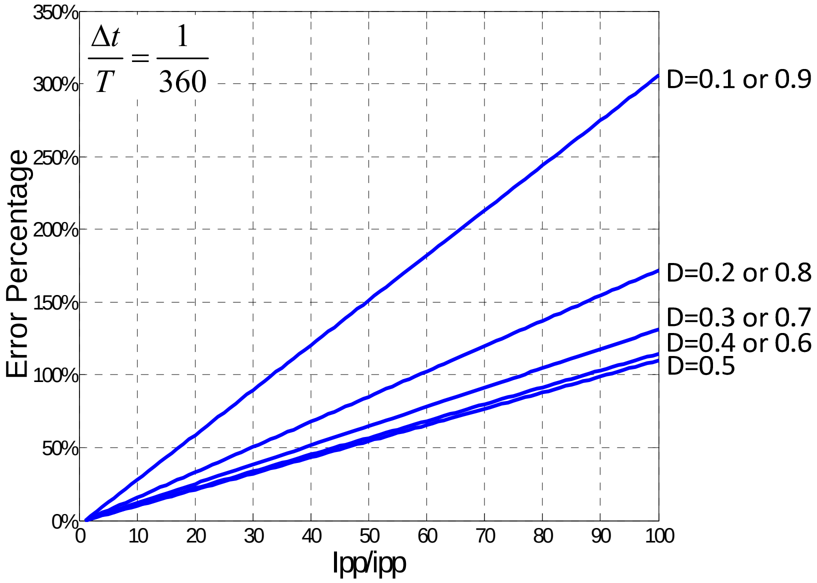

Figure 3.4 Two-winding method's sensitivity to phase error

Given 1° phase error, the measurement error increases as the core becomes high Q. When I_{pp}/i_{pp} reaches 100, the error is higher than 100%. If the waveform duty cycle is 0.1 or 0.9, the error can be as high as 300%.

So for rectangular voltage excitation, the conventional two-winding method has the similar sensitivity problem as the sinusoidal excitation.

3.2 Proposed Core Loss Measurement Method with Inductive Cancellation

The principle of the proposed method with resonant capacitor in Chapter two is using the capacitor to cancel the reactive voltage on the magnetizing inductor, so the phase difference between v_3 and v_R will be close to 0°, and the integration of their product will be less sensitive to phase discrepancy. The schematic is redrawn in Fig.3.5.

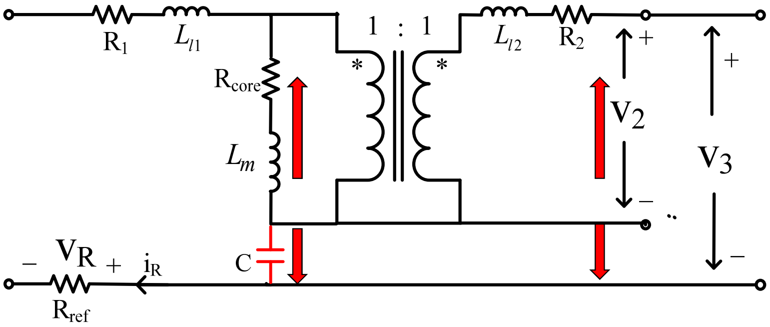

Figure 3.5 Core loss measurement method with capacitive cancellation

The method in Fig. 3.5 is only for sinusoidal excitation, because it only cancels the reactive voltage at a single frequency. Following the principle of cancelling reactive voltage, we can get another circuit. To cancel the reactive voltage on the magnetizing inductor over the entire frequency range, the capacitor is replaced with an ideal inductor and the polarity of the transformer is changed, as shown in Fig. 3.6(a). In principle, the core loss resistor should be in parallel with the magnetizing inductor. For analytical simplicity, the core loss resistor R_{core} is placed in series with the magnetizing inductor, and its resistance could be time-variant. If N_1:N_2=1:1, v_3 is the sum of the inductor voltage v_L and $-v_m$.

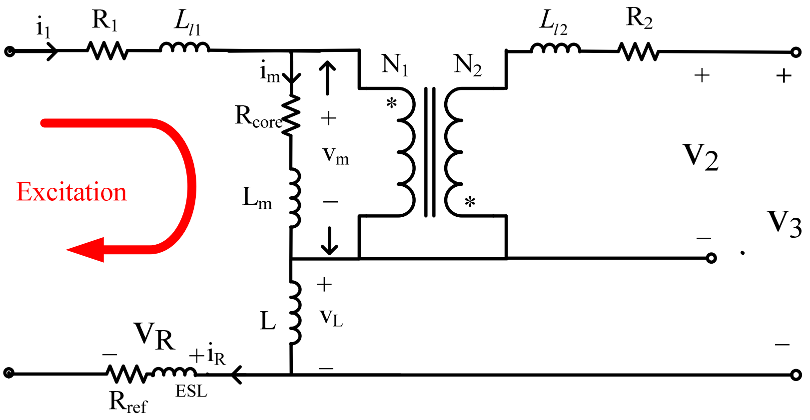

(a) Proposed method with ideal inductor

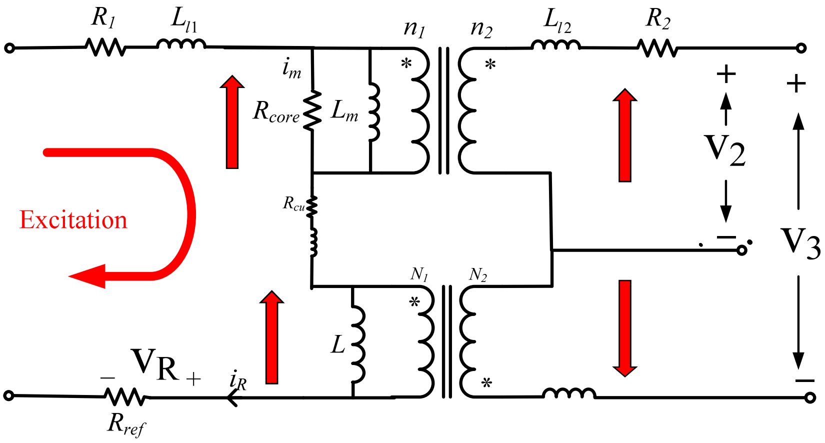

(b) Proposed method with air core transformer

Figure 3.6 Proposed method for non-sinusoidal excitation

$$v_3 = (R_{core} + sL_m - sL)i_m \tag{3.4}$$

If $L=L_m$, the voltage on the magnetizing inductor will be cancelled out for any frequency. v_3 will equal to the voltage on the equivalent core loss resistor and in phase with the v_R. Integrating the product of v_3 and v_R will be the loss on R_{core}, and less sensitive to phase discrepancy. However, if the inductor is not ideal, the winding loss on the added inductor L will affect the accuracy of the measured result. So the circuit in Fig. 3.6(b) is proposed. It uses the sensing winding voltage of an air core transformer to cancel the reactive voltage on the magnetizing inductor. Because the air core doesn't have core loss, we can use its magnetizing inductor to be the ideal inductor in Fig. 3.6(a).

According to the new measurement method, the core loss can be calculated as

$$P_{core} = \frac{1}{TR_{ref}} \int_0^T v_3 v_r dt \tag{3.5}$$

T is the excitation period; R_{ref} is the current sensing resistance.

With this arrangement of two transformers, this method gets to the similar principle as the method in Fig. 2.4: most reactive power in the core under test is cancelled with the reactive power in the air core, leaving only the resistive power which is consumed by the core under test. If the power is more resistive, it will be much easier to be measured.

From another perspective, the proposed method can be interpreted as comparing the core under test with a reference core, which is the air core in Fig. 3.6(b). Their power difference is the core loss of the core under test. In some situations, the air core may not be a good choice as the reference core. For example, when the magnetizing inductance of the core under test is high, a big air core transformer is needed. It will introduce non-negligible parasitic capacitors. A low-loss core could be used as the reference core, and its size and parasitic capacitors can be much smaller than the air core. If its loss is much smaller than the core under test, the error can be tolerable.

3.3 Choice of Reference Transformer

The design of reference transformer is critical for the measurement accuracy. This transformer should be:

1) low core loss
2) low parasitic
3) easy to tune the magnetizing inductance value

There are several choices of this transformer.

3.3.1 Air Core Transformer

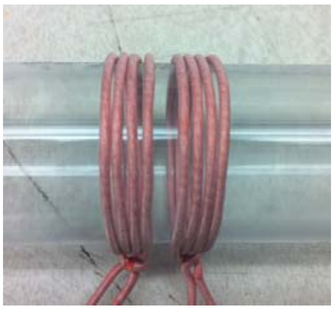

Figure 3.7 Air core transformer

Figure 3.7 shows an air core transformer composed of two parallel windings on a plastic tube. Apparently, air core doesn't have core loss. And its magnetizing inductance can be tuned by adjusting the distance between the two windings. So it meets the requirement (1) and (3). However, the air core transformers have large parasitic when the inductance required is high. These parasitic inductors and capacitors can be detrimental to the waveforms and accuracy. Unless the inductance of the core under test is small (below a few hundreds of nano-henries), air core transformer is not preferred.

3.3.2 Toroid Inductor Made of Low-loss Material

The transformer made of low loss toroid core is a good choice because of its low parasitic. The loss in the reference core should be much smaller than the core under test. So that a low permeability and low loss material is the preferred candidate.

Figure 3.8 Transformer made of low loss toroid core

If it is hard to find a much better material than the core under test, a gapped core made of the best available reference core can be used. The gap can reduce the effective permeability of the core. As a result, more tunes will be needed to achieve required inductance. Increased number of turns will reduce the flux density, due to

$$B_{ac} = \frac{1}{NA_e} \int v(t)dt \tag{3.6}$$

As the flux density reduced, the core loss of the reference core is reduced. Since the winding loss is automatically excluded from the test, the increased turn number won't increase this part of loss.

The drawback is inconvenient to tune the inductance value continuously. The inductance value is to the square of the turn number, so if there is a need to fine tune the inductance, one needs to change the turns number and ratio.

3.3.3 Variable Transformer by Adjusting the Gap Distance

There are many ways to realize a variable inductance transformer. Figure 3.9 shows one kind of variable inductance transformer. Two pieces of the U core are fixed on a vise. The gap between two U cores can be adjusted by a micrometer. By adjusting the air gap, the magnetizing inductance of the transformer can be tuned conveniently. So it can meet all of three requirements for the preferred reference transformer.

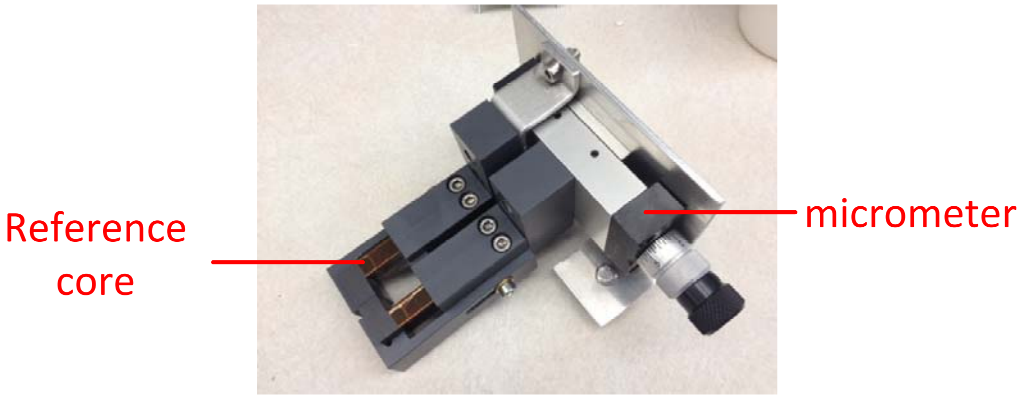

Figure 3.9 Transformer with adjustable air gap

The core in the adjustable transformer is made of 4F1, which has very good low loss performance at high frequency above 3MHz. And the existence of gap will further reduce the core loss as discuss before. So it is a good choice for reference transformer.

3.4 Measurement Considerations

This measurement method has higher requirement of circuit design, because the harmonics of the non-sinusoidal excitations will be much higher than the fundamental frequency and the high-order harmonic ringing will ruin the waveforms. Close attention should be paid to the following issues.

3.4.1 Parasitic Capacitors

The transformer inevitably has parasitic capacitors: the intra- and inter-winding capacitors. As shown in Fig.3.10. These parasitic capacitors will cause ringing problems during the test.

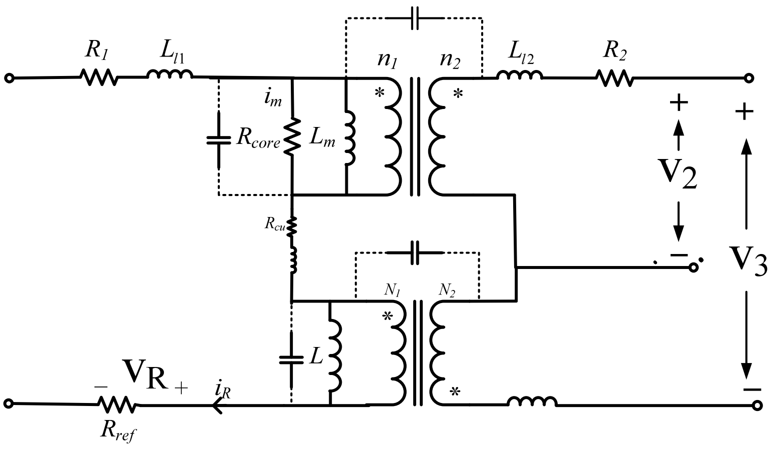

Figure 3.10 Parasitic capacitors on the transformers

The parasitic capacitors can be reduced by carefully winding. Bifilar winding is recommended on the core under test, because bifilar winding can provide the best coupling to the transformer. To make the measurement accurate, the coupling of the core under test transformer should be as high as possible. What is more, it is better to sparsely distribute the winding on the core so that the intra-winding capacitor is reduced. To further reduce the parasitic capacitor and push the transformer self-resonant frequency caused by parasitic capacitors, a smaller sample is recommended. Smaller sample means smaller inductance, shorter winding and smaller parasitic capacitors. In addition, the reference core can also benefit from smaller inductance and parasitic. Fig. 3.11 shows a TN13/7/6 core and a sliced core. The original core sample from the manufacturer is too thick. The sliced core reduces the thickness to 1.6mm. And the turn number reduces from 6 turns to 4 turns. Accordingly, the turn number of the reference core is greatly reduced. By doing like this, the self-resonant frequency has been raised much higher. In Fig. 3.12 and Fig. 3.13, the measurement waveforms of the original thick core with more turns of

(a) Toroid sample TN13/7/6 (b) Sliced sample

Figure 3.11 Sliced toroid sample

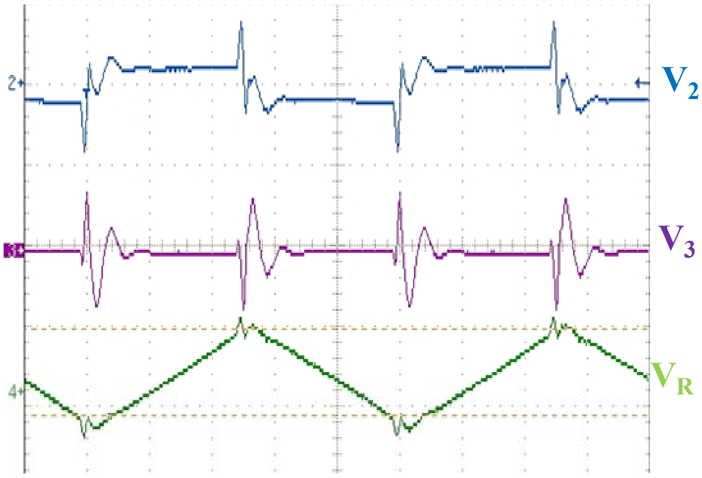

Figure 3.12 Measured waveforms with thick sample and more turn number

Figure 3.13 Measured waveforms with sliced sample and less turn number

winding and the sliced core with less winding are compared. It is obvious that the sliced core will have less ringing and much cleaner.

The connection of the secondary side of the two transformers will also affect the ringing. The secondary windings in Fig.3.10 are floating. Good grounding will reduce the current in the parasitic capacitors and alleviate ringing. The proper connection of the secondary winding to the primary side is shown in Fig. 3.14. The core under test is moved closer to the current sensing resistor. So as the capacitive cancellation method, three probes can find the common ground at the red wire in the figure. Other than providing common ground, this connection can minimize the current through the inter-winding capacitors. Because the core under test's winding is bifilar, the potential between point A and point B is quite similar. As a result, the displacement current through the inter-winding capacitor of the bifilar winding is the minimum, which means the inter-winding capacitor of the core-under-test is absent from the ringing oscillation.

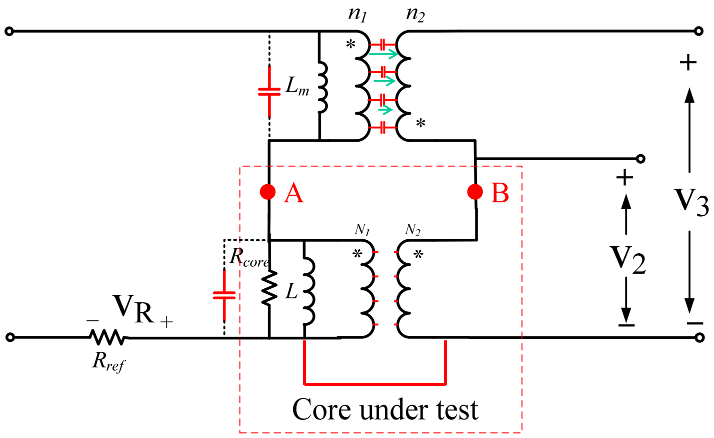

Figure 3.14 Proper connections of the secondary side windings

However, if arrange the connection of the secondary side like the schematic in Fig. 3.15, the current through the inter-winding capacitor will be larger. The current through the reference transformer's inter-winding capacitor is the same as the Fig. 3.14. But the potentials of point A and B are different, so the adjacent primary and secondary winding's potential are quite different. As a result, the displacement current is much higher.

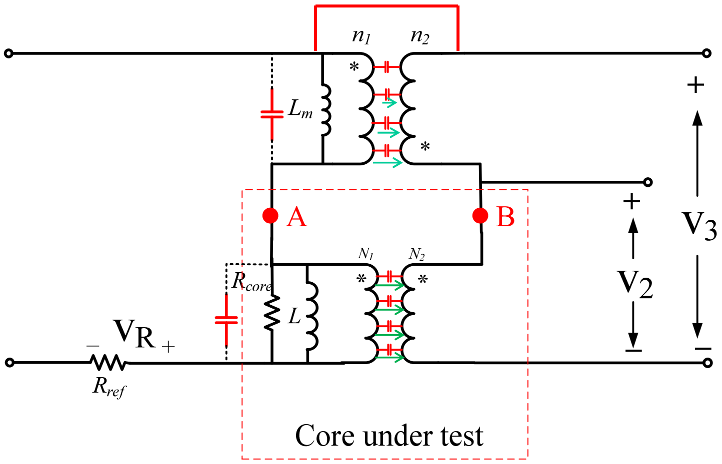

Figure 3.15 Improper connections of the secondary windings

A comparison is made between the two connections using a 4C65 NiZn ferrite samples. 4C65 is a low loss and low permeability material so air core transformer is used as the reference transformer. Three differential probes are monitoring the voltages of v_2, v_3 and v_R in the test circuit in Fig. 3.14 and 3.15. The testing conditions of the comparison are very identical, except the connection of the secondary winding to the primary winding. From the waveforms, we can clearly see that if the secondary side winding is not properly connected, the ringing will be very obvious.

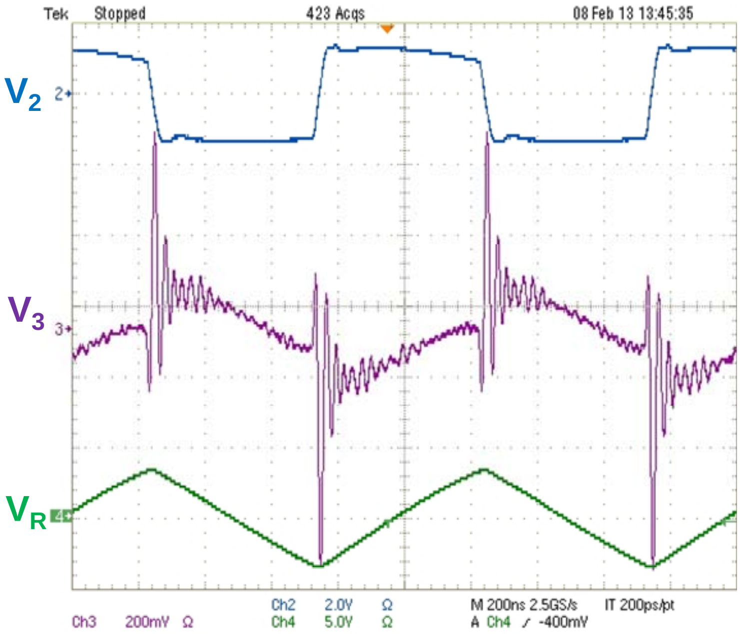

Figure 3.16 Oscillatory waveform using the improper connection of secondary windings

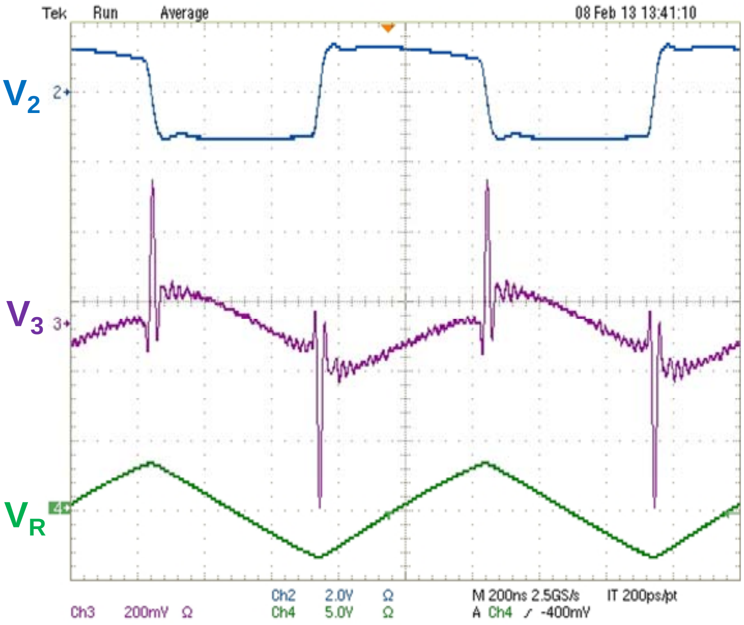

Figure 3.17 More cleaner waveforms using proper connection

3.4.2 Excitation

The AC excitation comes from wide bandwidth RF power amplifier (25W250A or 1000L from Amplifier Research®) driven by arbitrary/function generator (AFG3102 from Tektronix®). There is an alternative choice to excite the inductor. The alternative way is to use the converter in which the inductor is supposed to be used, for example, a bridge converter. The reasons why this excitation method is not preferred are:

(1) The voltage rating of the switches. Since both the inductor under test and the reactive cancellation transformer are excited by the buck converter, so the voltage on the switches is about two times of the voltage on the inductor or transformer. To keep the AC voltage on the inductor-under-test the same as it is used solely in the converter, the voltage rating of the switches is doubled. Sometimes such requirement can't be satisfied.

(2) Hard to control the voltage ringing caused by the parasitic of the switches. The ringing is caused by the parasitic inductor and capacitors in the switching loop, and is detrimental to the measurement waveforms as well as results. Using the driving method of power amplifier, we can control the rising and falling time to control the ringing.

(3) The voltage drop on current sensing resisters. In order to reduce the parasitics' effect to the phase discrepancy, the current sensing resistance is preferred to be larger. So the current sensing resistor will have considerable voltage drop. As a result, the voltage on the inductor under test is no longer rectangular as expected. The top of the voltage is not flat.

The excitation method using amplifier doesn't have the drawbacks listed above, and is more compatible for different shapes of waveforms. With the programmable function generator, the waveforms can be manipulated. So the rising and falling edge of the rectangular voltage can be controlled and the ringing can be reduced. And the descending top of the voltage can be compensated by the waveform with an ascending top.

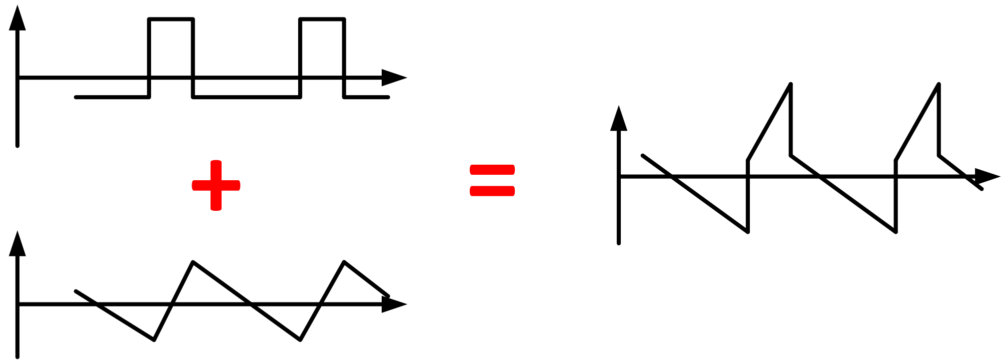

Figure 3.18 Excitation waveform with PA input impedance compensation

Fig.3.18 shows the waveform generated by the arbitrary function generator. It is a superposition of a rectangular and a triangular voltage. Controlling the ratio of their amplitudes can make the excitation on core under test as a rectangular shape.

3.4.3 Isolation Transformer

Because of the grounding requirement, there is a need for an isolation transformer between the amplifier and the test circuit if using single-ended probes. If use differential probes, this transformer will not be necessary.

Because the power amplifier has an output impedance of 50Ω, it is usually much larger than the impedance of the core-under-test transformer, and share much of the voltage of the power amplifier can provide. In addition, this large output impedance will make the descending top more severe. So it is more difficult for the waveform compensation. In order to reduce the voltage drop on the output impedance of the power amplifier, a large turn ratio is chosen in order to transform the impedance to a smaller value. In this setup, turn ratio of 3:1 is selected to transformer 50Ω impedance to about 5.56Ω.

The transformer works at high frequency, so it should keep good transformer behavior at sufficiently high frequency and low parasitic capacitors. To meet these requirements, high frequency magnetic material 4C65 (NiZn ferrite from Ferroxcube®) was selected since its relatively stable permeability up to 30MHz. The transformer is shown in Fig. 3.17, whose core is toroid shape. The winding is Litz wire, and sparsely winded on the core, to reduce the parasitic capacitors between windings.

Figure 3.19 Impedance transformer

3.4.4 Measurement with DC Bias

To measure the core loss with non-sinusoidal wave and DC bias, a similar scheme can be used as Fig. 2.20, except the resonant capacitor is replaced with reference transformer. Two identical samples are used. Each core has three windings: excitation winding, sensing winding and bias winding.

3.5 Measurement Example

Experiments are performed to verify and demonstrate the new method. The core sample is a thin toroid core made of sintered low temperature co-fired ceramic (LTCC) magnetic material (40011 from ESL ElectroScience®). A toroid core made of NiZn Ferrite (4F1 from Ferroxcube®) is chosen as the reference core. To make sure that reference core won't introduce much error, its loss density and core volume should be estimated first. The core loss densities of 4F1 and 40011 are compared in Fig. 3.20, which are measured with the resonant capacitor method in Fig. 2.4. The figure shows that NiZn ferrite has much lower loss than 40011 LTCC material at the same flux density. The transformers winded with the core under test and the reference core are shown in Fig. 3.21(a), both with the 1:1 turn ratio. Calculation shows that their magnetizing inductances and core volumes are similar but the flux density in the NiZn ferrite core is about 1/3 of the flux density in the LTCC core, with the same voltage excitation. So the loss in the NiZn ferrite core is much smaller than the loss in the LTCC core, and we can use the NiZn ferrite core to be the reference core, without introducing significant error. The measurement setup is shown in Fig. 3.21(b). The core under test is immersed in a cup of hot oil to keep the core temperature stable. The temperature of the oil is controlled by the hotplate at the bottom. In following experiments, the temperature is kept at 100°C.

The first experiment measured core loss of 40011 under sinusoidal voltage excitation. The measurement waveforms are shown in Fig. 3.22(a). The cancelled voltage v_3 is in

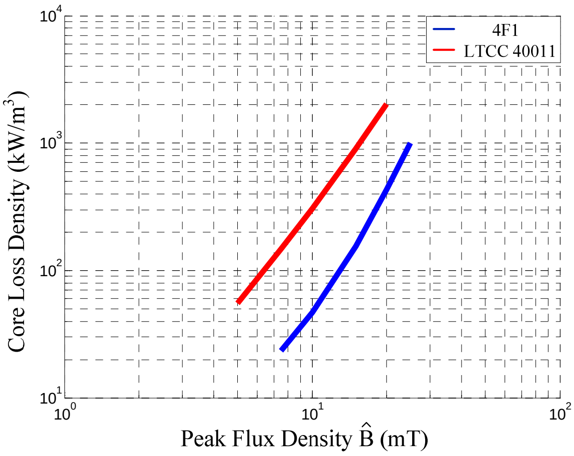

Figure 3.20 Loss comparison between 4F1 and LTCC 40010

(1.5MHz sinusoidal excitation, 100°C)

(a) Core under test (LTCC, left) and reference core (NiZn, right)

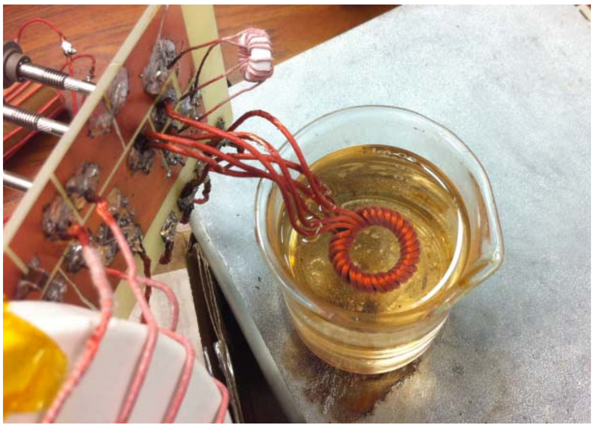

(b) Core under test in oil bath

Figure 3.21 Experiment setup

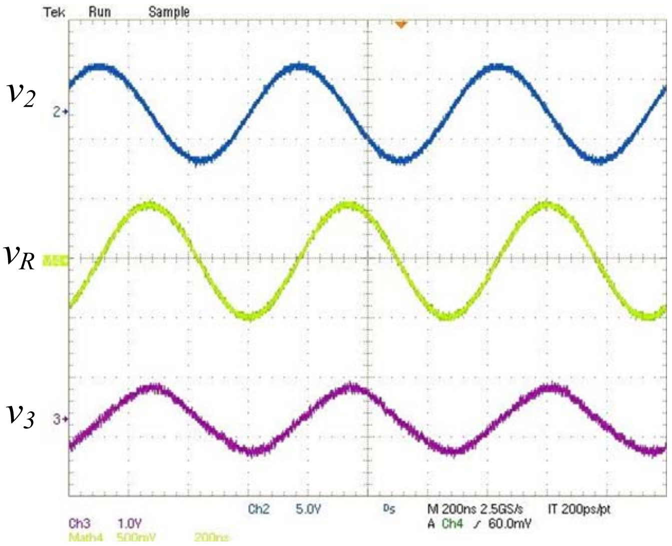

(a) Measurement waveform

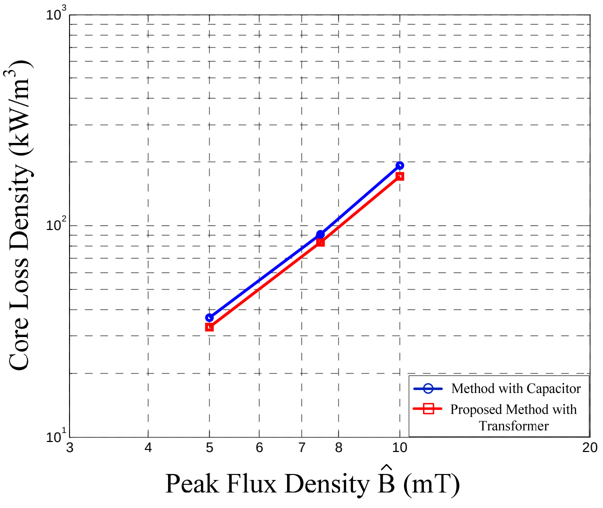

(b) Comparison between two methods

Figure 3.22 Experimental waveforms and results for sinusoidal flux excitation

(LTCC 40011, 1.5MHz, 100°C)

phase with the voltage on the current sensing resistor v_R. So the measured result should be less sensitive to phase discrepancy. The measured core loss density is shown in Fig.

3.22(b), compared with the measured result of the method with resonant capacitor. The results of the two methods are consistent, though with 10% difference.

The second experiment measured the core loss under rectangular voltage excitation. The core losses at different duty cycle are measured. Typical waveforms are shown in Fig. 3.23. The core losses at different duty cycle are shown in Fig. 3.24. The peak flux density is kept the same at 10mT. From the measured result, we can see that core loss varies with different duty cycle. At 50% duty cycle, the core loss is the lowest, and lower than sinusoidal excitation. As the duty cycle increases or decreases, the core loss increases. When the duty cycle is lower than 30% or higher than 70%, the core loss is higher than sinusoidal excitation.

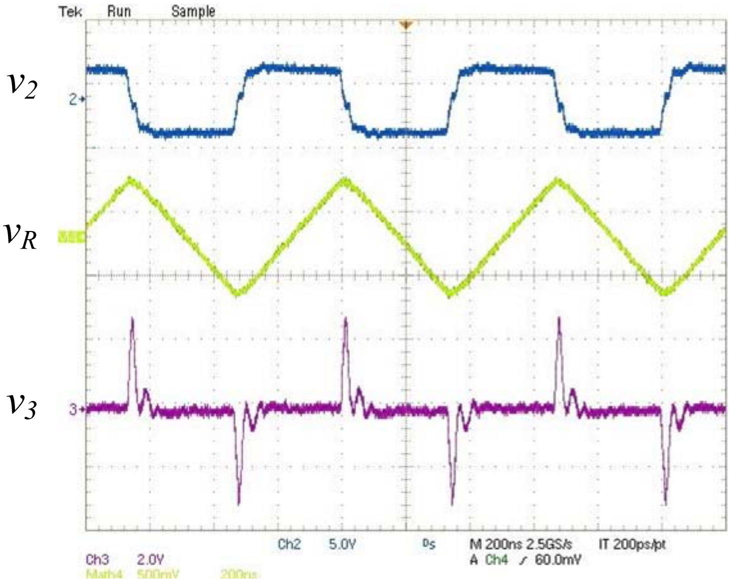

Figure 3.23 Experimental waveform for triangular flux

(LTCC 40011, 1.5MHz, 100°C)

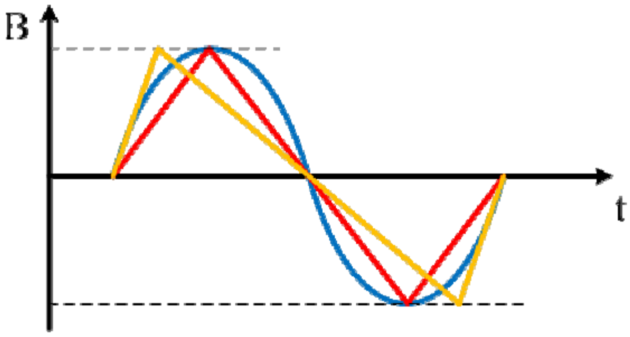

(a) The peak flux densities are kept the same

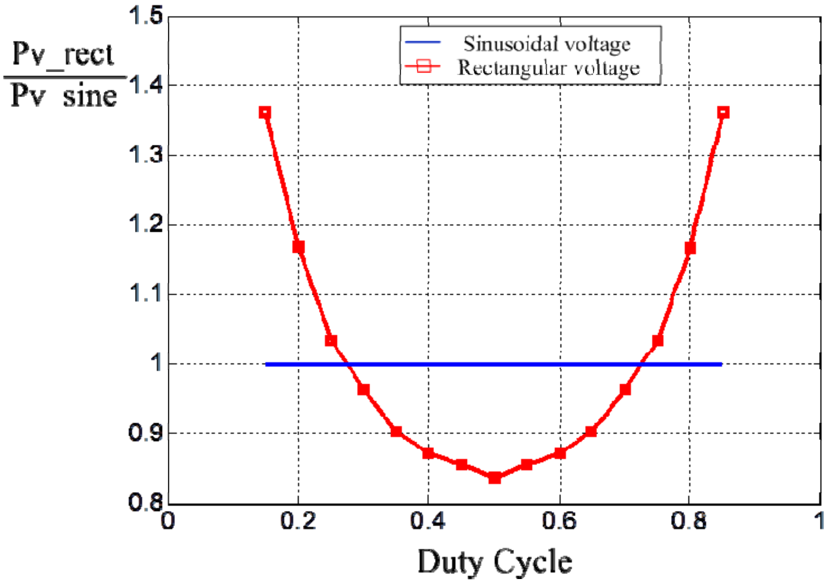

(b) Measured core loss density normalized by sinusoidal loss

Figure 3.24 Measured core loss for different duty cycle triangular flux (LTCC 40011, 1.5MHz, 100°C)

3.6 Measurement Waveforms Explanation and Analysis

The measured waveforms in Fig. 3.23 show that the core loss is measured as a series of spikes in v_3 probe. It seems that the core loss happens at the interval of the rising and falling edge of the rectangular waveform, which counters the intuitive. Further analysis of the circuit principle and the B-H loop, we can explain that these spikes are caused by the dynamic B-H loop.

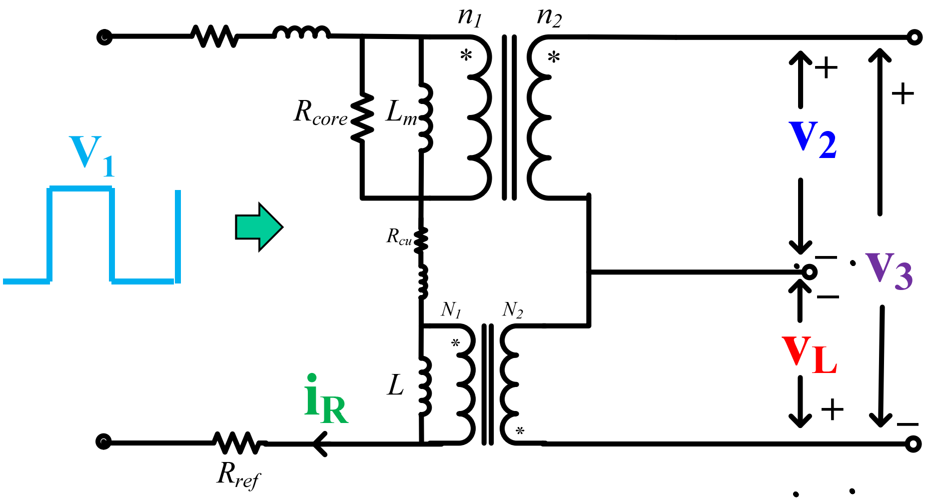

Figure 3.25 Equivalent circuit model

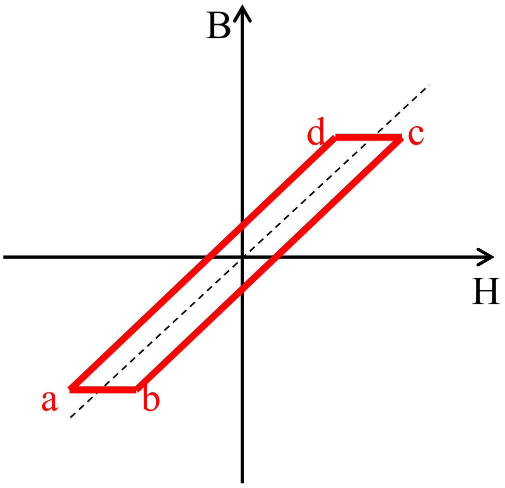

Figure 3.26 Dynamic B-H loop caused by core loss

The dynamic B-H loop is drawn in the Fig.3.26. Because the excitation is rectangular voltage, the B-H loop is parallelogram. The four points of the parallelogram is denoted as a, b, c and d. The simplified waveforms are shown in Fig.3.27.

Assume before time t_0, the input voltage v_1 is negative, and the flux trajectory is approaching from d to a. The core under test and the reference core divide the same

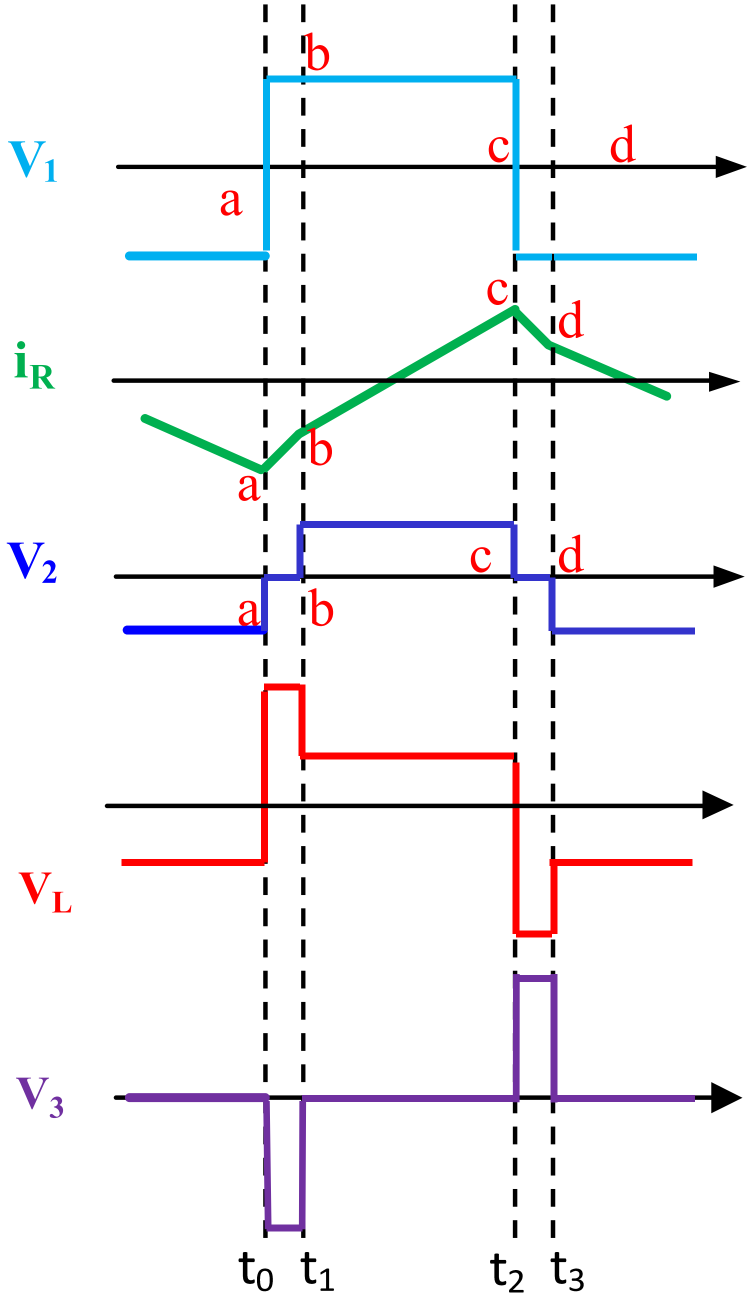

Figure 3.27 Simplified waveforms

voltage from the input, assuming the leakage inductance and other resistor in the excitation loop is small and only share negligible voltage drop. v_3 is zero, as it is the actually the subtract of v_2 and v_L.

At t_0, the flux trajectory reaches point a, and the input voltage starts a step change, then the trajectory moves from point a to b. Because of the core loss, the flux density doesn't have much change while the current keep changing. So the flux density "lags" behind the change of magnetic field. The slope of the line a-b is rather flat, so that the instantaneous permeability of the core under test is very low. On the other hand, the reference core is low loss and response much faster than the core under test. As a result, during the small interval t_0 to t_1, the reference transformer will take over most of the input voltage, while the core under test transformer will have much lower voltage drop. So this causes the plateau in v_2 and the spike in v_L, as shown in Fig.3.27. v_3, the subtraction of v_2 and v_L will be a pulse. The current slope during this interval is approximately doubled, because there is only L in this excitation loop.

After reaching t_1, the core under test starts to response to the excitation. The instantaneous permeability returns to its normal value, so the core starts to share the input voltage. v_3 goes back to zero again and the current slope reduces to normal, until t_2.

During t_2 to t_3, the same phenomenon can be observed.

Experimental waveforms measured from 3F3 toroid sample are shown below. To compare with the new method and the two-winding method, the B-H loops measured with two methods are plotted. (both loops are plotted using v_2 and v_R) The two loops almost completely overlap each other. So it indicates that: in the new method, although the voltage on the core under test is not exactly rectangular because of the small plateau during the t_0-t_1 and t_2-t_3 intervals, this pseudo-rectangular voltage produces the same loss as the rectangular waveform.

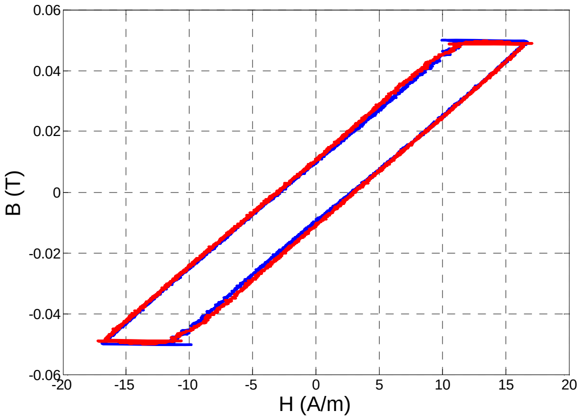

Figure 3.28 Plotted B-H loop with the waveforms by two methods

According to the B-H loop, the losses measured by both methods are the same. But the proposed method is much less sensitive to phase discrepancy. Assume the current in the proposed method is lagged for a small time delay Δt for various reasons. The loss error percentage is calculated as

$$\Delta = \frac{\Delta P_{core}}{P_{core}} \approx \frac{2}{D(1-D)} \times \frac{\Delta t}{T} \tag{3.7}$$

The error percentage is plotted in Fig.3.30. The error is independent of the quality factor of the core. Given 1° phase error, the maximum loss error is limited in 6.2%. The accuracy is much better than the conventional method, especially when the core is low loss.

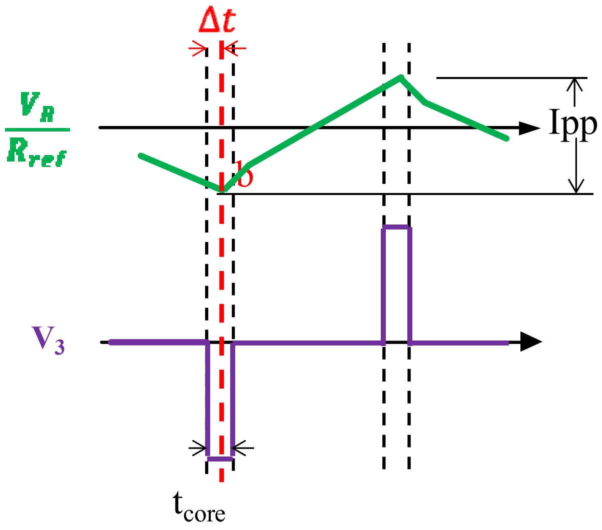

Figure 3.29 Waveforms of new method with small time delay

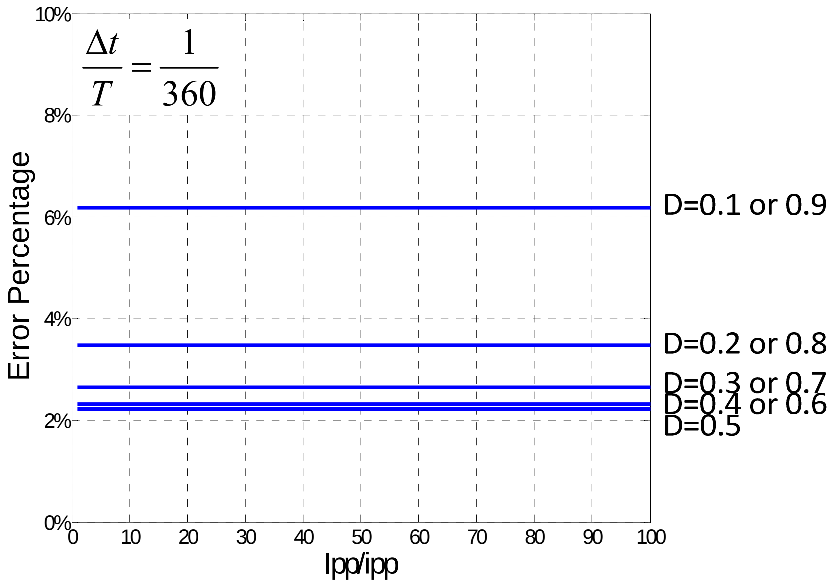

Figure 3.30 Phase error sensitivity of the new method

3.7 Inductor Loss Measurement Method

3.7.1 Test Circuit

The method in previous sections is for core loss measurement. If replacing the transformer with an inductor, the method can measure the total loss of the inductor, including core loss and winding loss. But for many inductors, it is not possible or convenient to add an additional winding for DC current bias. So the method is modified as in Fig.3.31. The major difference is that there is a DC current source in the excitation loop. This DC current source controls the DC current through the inductor under test.

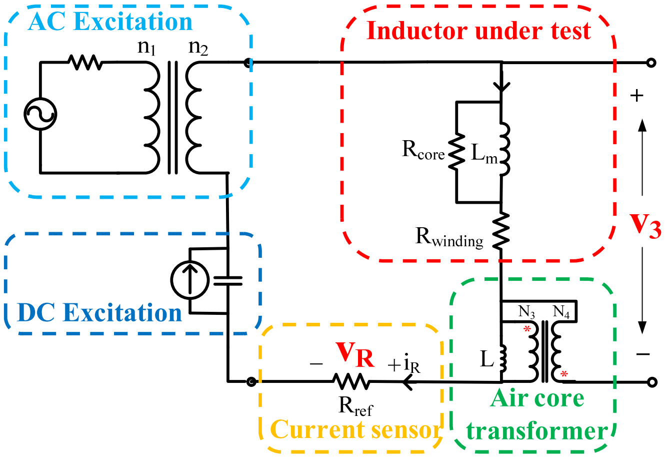

Figure 3.31 Proposed inductor loss measurement circuit

There are basically four parts of the measurement circuit, which are inductor-under-test, air core transformer, current sensor and excitation. The inductor-under-test has two parts of loss: winding loss and core loss. Since the DC winding loss can be conveniently measured by four-terminal multi-meter, the winding loss mentioned here is only AC winding loss. To measure the loss consumed on the inductor, an air core transformer is used to cancel the reactive voltage on the inductor-under-test. The connection and polarity arrangement of the air core transformer is shown in Fig.3.31. The voltage on the magnetizing inductor of the air core transformer is reversed on the secondary side, and the reversed voltage is used to cancel the reactive voltage on the inductor-under-test. If the magnetizing inductor of the air core has the same inductance as the inductor-under-test, the voltage v_3 will be the resistive voltage on the loss resistors of the inductor-under-test. So v_3 will be in phase with the current through the inductor i_R. Integrating the product of v_3 and v_R will be less sensitive to phase discrepancy and more accurate. The principle is the same as the core loss measurement method above. The excitation is composed of two parts. One is a DC voltage source, which controls the DC current through the inductor. The other is AC source, which is generated by the RF power amplifier and added to the inductor via the isolation transformer T_1. With this kind of excitation setup, the circuit can measure the inductor loss under any practical excitations, like rectangular voltage with DC current, which is the case of inductors in PWM converters. With the measured waveforms, the loss can be calculated as

$$P_{loss} = \frac{1}{TR_{ref}} \int_T v_3(t) v_R(t) dt \tag{3.8}$$

The measurement setup is critical for the test accuracy. Some basic consideration is the same as the core loss measurement method. But there is something different.

3.7.2 Grounding Issue

Grounding is more complicated here, because the DC source will need proper grounding also. As previous methods, an isolation transformer is necessary to isolate the ground of the power amplifier and the test circuit. There are two arrangements of the connection of the test circuit. One is as shown in Fig.3.31 the negative of the DC source should be connected to the same ground as the power amplifier to prevent common mode current through the isolation transformer, and the differential probes are used to measure the voltages. If using single-ended probes, the circuit should be modified as the schematic below.

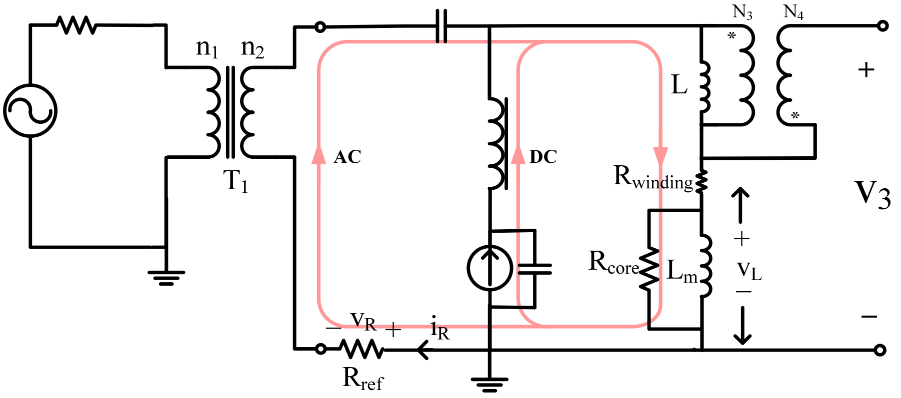

Figure 3.32 Another inductor loss test circuit with DC source

The dc current source is put in parallel with the inductor, and a chock inductor should be connected in series with the DC source to block AC current. At the same time, in the AC loop, a DC block capacitor is used to block the DC component. So the AC and DC current have the separate loop. A common ground can be found as displayed in the schematic. Another benefit of this schematic is the low requirement of the power rating of the current sensing resistor. The sensed the current is only the AC current, so the dissipated loss is much lower than the circuit in Fig.3.31. As a result, higher value resistors can be used to reduce the phase error and increase measured voltage amplitude. The potential problem of this scheme is that a high frequency chock inductor in series with the DC source. This inductor should be much larger than total inductance of the inductor under test and the reference transformer, or some AC current will go through the DC source and the test result is less accurate. Also the parasitic capacitors on the chock inductor can cause oscillatory ringing on the waveform if the measurement frequency is high.

3.7.3 Measurement Example

The inductor sample used in this measurement is Coilcraft® SLC7649, the inductance value is 120nH. In this example, air core transformer is chosen because the target inductor's inductance is only a few hundred nano-henries, which can be easily matched by air core transformer with only a few turns.

The air core transformer is simply two windings in parallel, shown in Fig. 3.33. The magnetizing inductance of the transformer can be adjusted by the distance of the two windings.

Figure 3.33 Air core transformer

In this measurement setup, two probes of P6251 from Tektronix are used. The bandwidth is 1GHz and the input capacitance is smaller than 0.1pF. Because they are differential probes, the schematic in Fig. 3.31 can be used and the potential problematic RF chock can be saved.

The oscilloscope used in this measurement is TDS7054. It is a digital oscilloscope with 500MHz bandwidth and 5GHz sample rate.

The measurement setup is shown in Fig. 3.34.

Figure 3.34 The inductor loss measurement setup

The excitation is 1MHz 6A peak-peak triangular AC current with 10A DC current through the inductor. The measurement waveforms of inductor voltage v_2, current sensing voltage v_R and cancelled voltage v_3 are shown in Fig. 3.35. The voltage on the inductor is rectangular so the current is triangular. Due to probe's connection setup, the current measured here is $-i_R$, so v_R has 180° phase angle difference with v_2. The cancelled voltage v_3 has a series of spikes and in phase with the current. These spikes are caused by the parallelogram B-H loop of the core, as discussed in previous section. And the little slope between the spikes is caused by the droop on winding resistance of the inductor. Because of the two parts of loss, v_3 is the sum of a small triangular voltage and a series of spikes. The measured AC loss of the inductor is 109mW.

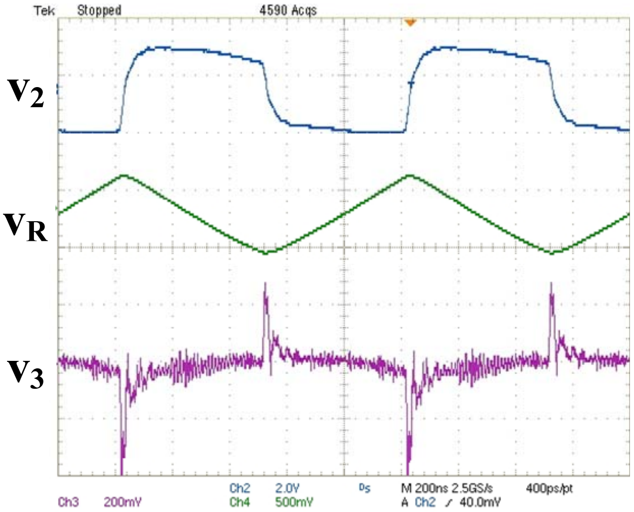

Figure 3.35 Measurement waveforms

Chapter Four Core Loss under Rectangular AC Voltage and DC Bias Current

The AC excitation waveform and DC bias will have impact to the value of core loss, proven by a lot of experimental data [17][20][21][22][24][25][27][28][32][33][34][35]. The best way to know the core loss is to test it under desired working condition. However, it needs extended efforts. People tried to model the core loss with limited labor on measurement. This chapter investigates the core loss under rectangular AC voltage and DC bias, and proposes a new core loss based on test results of some commercially available materials.

4.1. Experimental Verification of Some Existing Core Loss Models

The different waveforms will change the waveforms of the B-H loops, which represent the core loss. In Fig.4.1, the measured sinusoidal B-H loop and rectangular waveform B-H loop at different duty cycles are plotted and compared. The maximum flux swings are kept the same. The thinnest B-H loop happens at 50% percent duty cycle. As duty cycle approaching 10% or 90%, the core loss will increase. However, the magnetic material manufacturers only provide sinusoidal core loss.

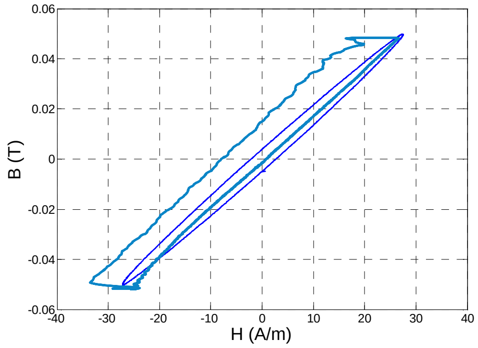

(a) D=0.1

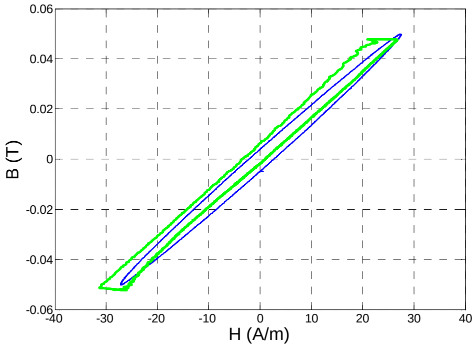

(b) D=0.2

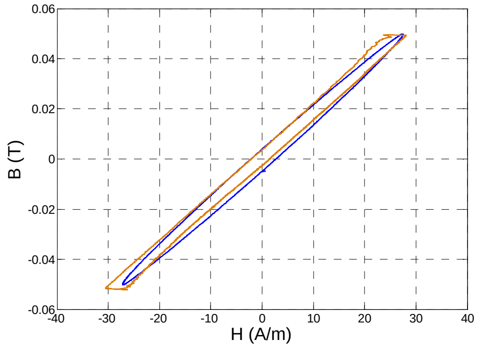

(c) D=0.1

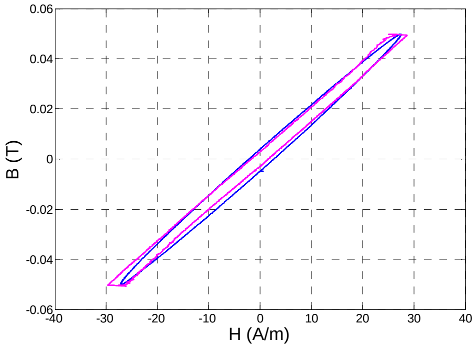

(d) D=0.2

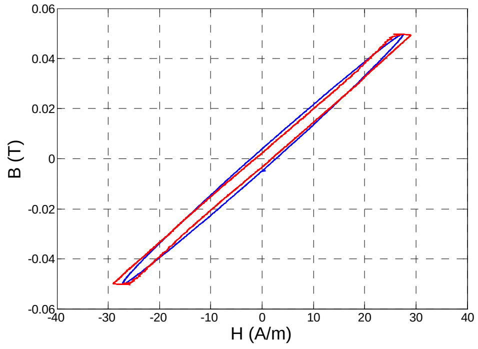

(e) D=0.5

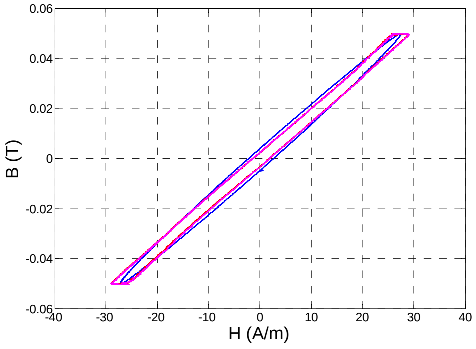

(f) D=0.6

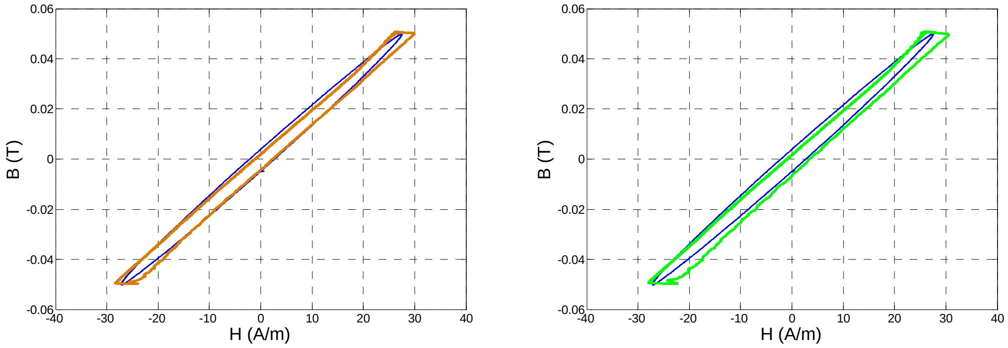

(g) D=0.7 (h) D=0.8

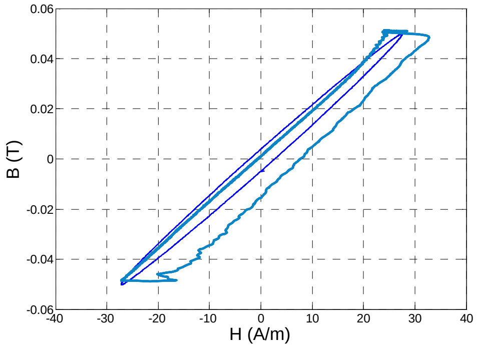

(i) D=0.9

Figure 4.1 Comparison of B-H loops under sinusoidal and rectangular voltages

There are numerous core loss models in literatures. Here the investigated waveforms are limited to rectangular because this is the most frequently seen waveform in power electronics applications. MSE, GSE and iGSE are three most referred formulas for such kind of waveforms.

3F35 is a commercial MnZn ferrite suitable for high frequency power transformers. The suggested working frequency range is from 500kHz to 1MHz, according to the manufacturer's datasheet. The sinusoidal core loss of 3F35 MnZn ferrite is measured from 200kHz to 1.7MHz, as shown in Fig.4.2. The core loss can be modeled as Steinmetz equation by curve fitting.

$$P_{core} = kf^{\alpha} B_m^{\beta} \tag{4.1}$$

Because of the nonlinearity, the Steinmetz parameter α, β are not constant. Fig.4.3 shows the incremental α and β curve-fitted by using the core loss of two or three nearest frequencies' data. α increases from about 1.4 to 2.7. β decreases from 2.7 to 2.3.

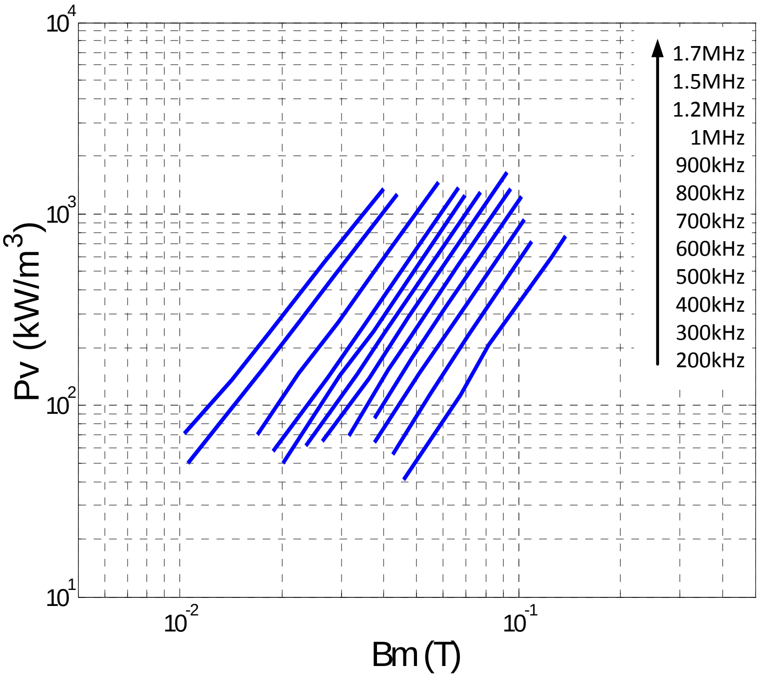

Figure 4.2 Measured core loss of 3F35 (sinusoidal, RT)

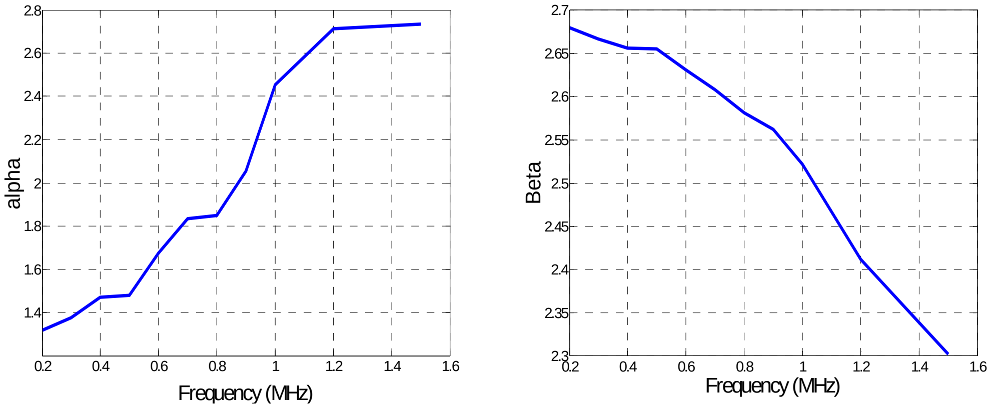

(a) α as a function of frequency (b) β as a function of frequency

Figure 4.3 α and β change with excitation frequency

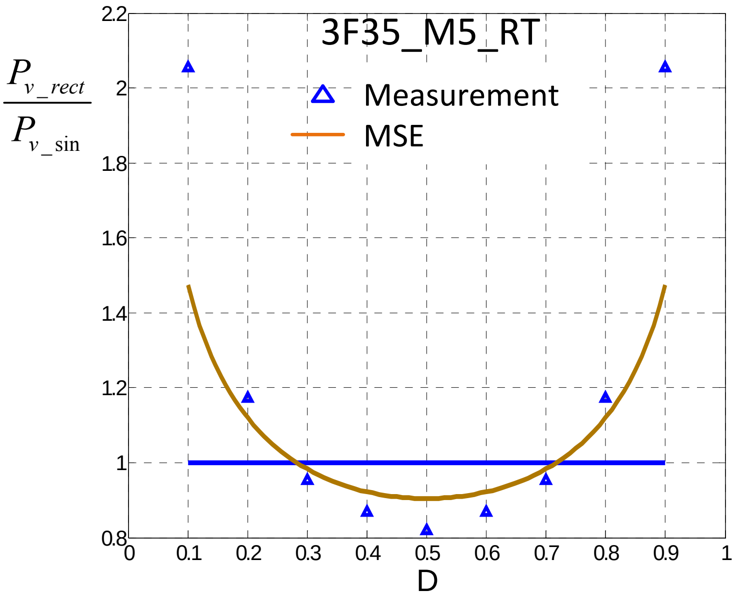

Figure 4.4 Measured core loss and prediction of MSE

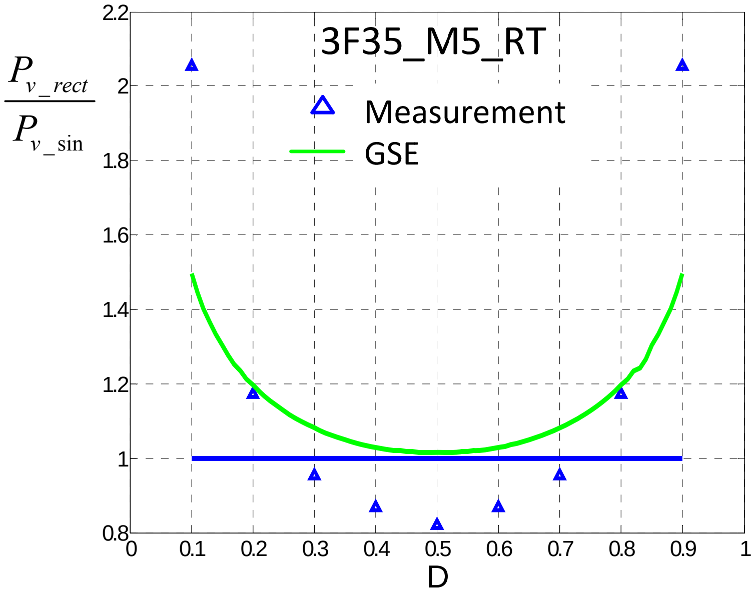

Figure 4.5 Measured core loss and prediction of GSE

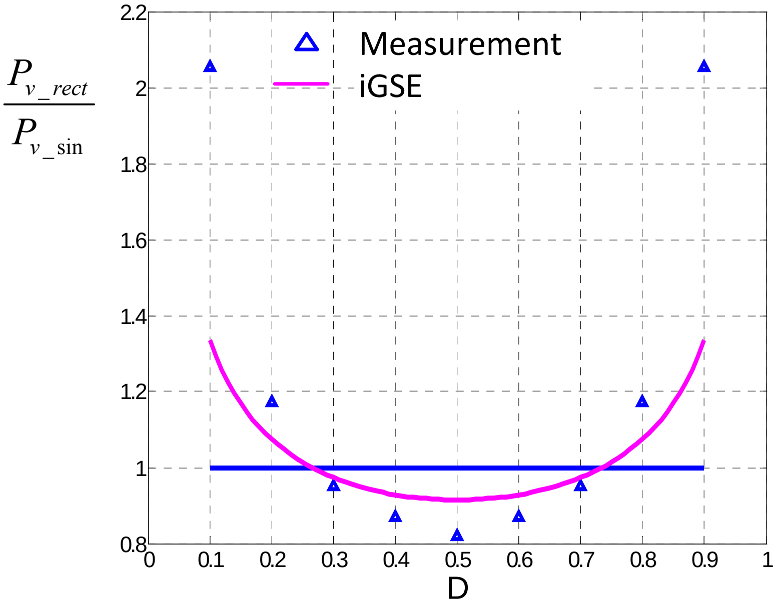

Figure 4.6 Measured core loss and prediction of iGSE

Implementing the MSE, GSE and iGSE using the α and β value in Fig. 4.3, we can see that none of them give satisfactory prediction, as shown in Fig.4.4, 4.5, 4.6. So a new model is proposed to better fit the core loss under the rectangular wave's core loss.

4.2 Proposed Core Loss Model for Rectangular AC Voltage

4.2.1 Equivalent Core Loss Resistor at Different Waveforms

The previous models all use hypothesis to derive the equations. The MSE assumes that the average core loss in one period is related to *dB/dt* and magnitude B_m. The iGSE defines the instantaneous core loss, and assumes this loss is related to the instantaneous *dB/dt* and B_m. Both MSE and iGSE try to be consistent with the original Steinmetz equation, to derive their modified parameters. These two equations tried to be universal, but ignored the reality that the physics of core loss is so complicated. Universal means not accurate. On some cases, it is good to use, while on other cases, it is not. The waveforms investigated in this chapter are focused on rectangular voltage waveforms with different duty cycles which are the most common waveform in power converters.

Other than making hypothesis, we can consider that the core loss can be modeled as a parallel equivalent core loss resistor with an ideal inductor. As discussed in chapter two, the equivalent resistor represents the average loss consumed by the core. The instantaneous resistor can be time-variant. But we can use a time-invariant resistor to model the loss consumed on the core, if the average loss equals the actual core loss. The reason to choose parallel representation is because the core is usually voltage excited. Assume AC voltage *v(t)* is exerted on the core. The ideal inductor will store some energy.

The resistor will consume certain loss, which is the core loss. It is reasonable to assume that the resistor R_c is a function of flux density and waveform. Since our discussion is limited to rectangular waveform, duty cycle will represent the shape of waveform. So now

$$R_c = R_c(B_m, D) \tag{4.2}$$

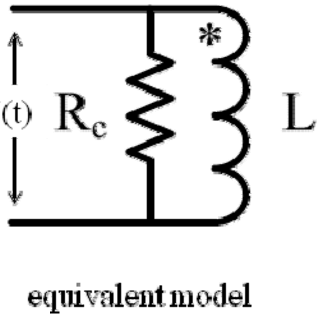

Figure 4.7 Core loss model

If the voltage waveform is know, then the core loss can be calculated as

$$P_v V_e = \frac{\frac{1}{T}\int_T v(t)^2\,dt}{R_c} = \frac{\frac{1}{TNA_e}\int_T (\frac{dB}{dt})^2\,dt}{R_c} \tag{4.3}$$

T is the period of the AC voltage, N is the inductor turn number, A_e is the equivalent area of the cross section of the core.

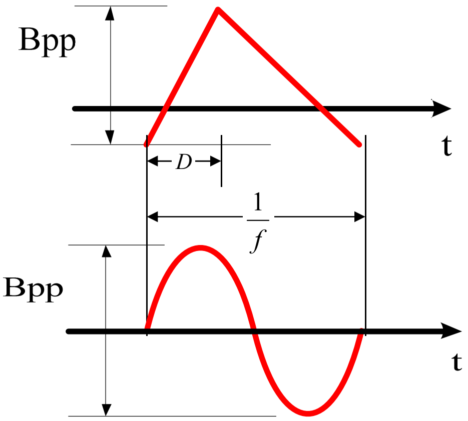

Figure 4.8 Different flux waveforms with the same amplitude

Now let's compare the rectangular and sinusoidal voltage. The rectangular voltage will excite triangular flux density in the core. If keeping peak-to-peak value of triangular and sinusoidal flux density the same as shown in Fig.4.8, the loss consumed by each waveform is

$$P_{v\_rect} = \frac{\int_T (\frac{dB}{dt})^2 dt}{V_e T N A_e R_c} = \frac{B_{pp}^2}{V_e T^2 D(1-D) N A_e R_{c\_rect}(B_m, D)} \tag{4.4}$$

$$P_{v\_\sin} = \frac{\int_T (\frac{dB}{dt})^2 dt}{V_e T N A_e R_c} = \frac{\pi^2 B_{pp}^2}{2 V_e T^2 N A_e R_{c\_\sin}(B_m)} \tag{4.5}$$

The equivalent core loss resistors in the above two equations depend on the flux density magnitude and waveform, so they are not necessarily the same. To find the ratio between the two losses, let's put P_{loss_rect} over P_{loss_sin}. The ratio can be simplified as

$$\frac{P_{v\_rect}}{P_{v\_\sin}} = \frac{2}{\pi^2 D(1-D)} \times \frac{R_{c\_\sin}(B_m)}{R_{c\_rect}(B_m, D)} \tag{4.6}$$

Once the ratio of the equivalent core loss resistors is known, the core loss ratio can be revealed. Since we have some experimental results, we can check what the relationship between the two resistors is.

$$\frac{R_{c\_rect}(B_m, D)}{R_{c\_\sin}(B_m)} = \frac{2}{\pi^2 D(1-D)} \times \frac{P_{v\_\sin}}{P_{v\_rect}} \tag{4.7}$$

For example, the rectangular wave core loss of 3F35 at 500 kHz is measured, which is already shown in Fig. 4.4 – Fig. 4.6. The measured core loss density of rectangular voltage is normalized by the core loss of sinusoidal waveform, and plotted in Fig.4.9. The flux densities of rectangular and sinusoidal wave are kept the same. The investigated core loss density is within the range from 100 kW/m^3 to 2000 kW/m^3, in which the power transformers are usually designed. The core loss ratio will vary with different flux density, even the duty cycles are the same. But the difference is relatively small. The ratio shown in Fig.4.9 is the averaged ratio measured at different flux densities.

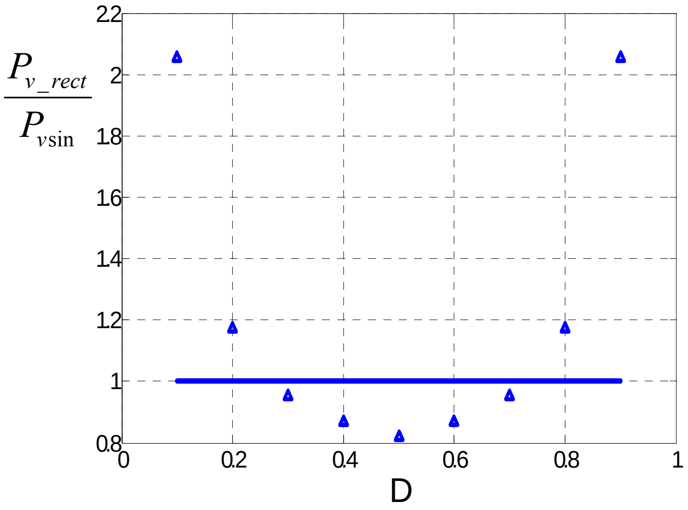

Figure 4.9 Measured core loss of 3F35 (0.5MHz, RT)

Using the measured the data, the ratio of the two resistors can be plotted, as shown in Fig. 4.10. It is interesting that the ratio of the two resistors is pretty close to 1, which means that when the magnitude of the flux density is the same, the equivalent core loss resistors of rectangular waveform and sinusoidal waveform are almost equal.

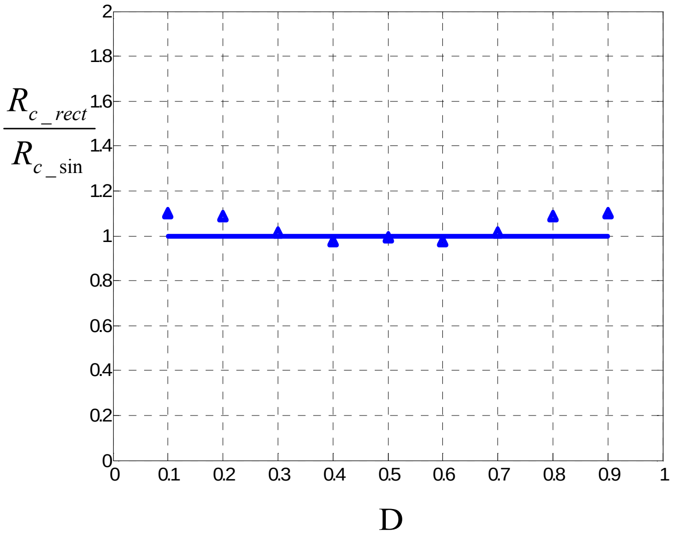

Figure 4.10 Equivalent core loss model of 3F35 (0.5MHz, RT)

By modeling the equivalent core loss resistor, we can model the rectangular core loss ratio to the sinusoidal core loss.

4.2.3 Normalized Core Loss Resistors for Various Ferrite Materials

Several ferrites (3C90, 3F3, 3F35, 3F5, N49, PC90, DMR50B) from different manufacturers (Ferroxcube, Epcos, TDK, DMEGC) are tested at 200kHz, 500kHz and 1MHz, respectively. The core loss ratios are plotted in Fig. 4.11, 4.13, 4.15. The resistor ratios are plotted in Fig. 4.12, 4.14, 4.16.

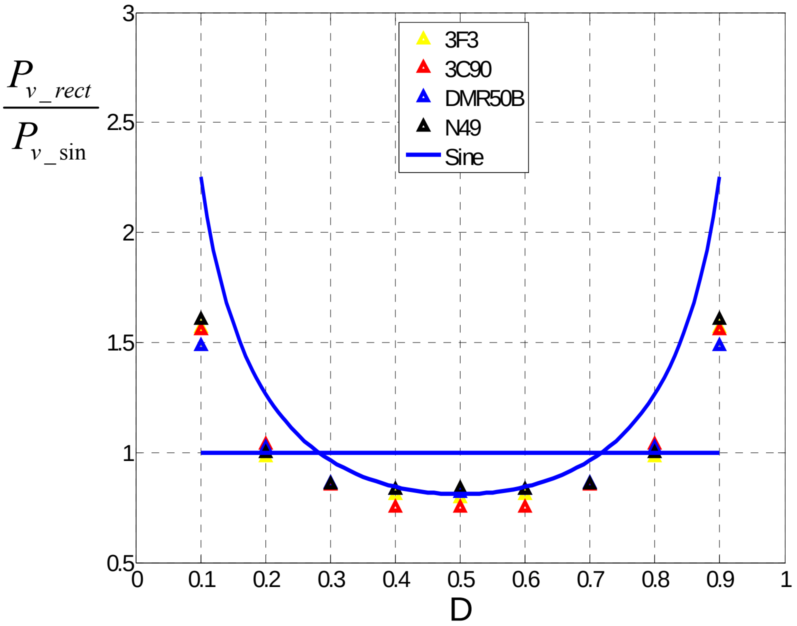

Figure 4.11 Measured core loss (0.2MHz, RT)

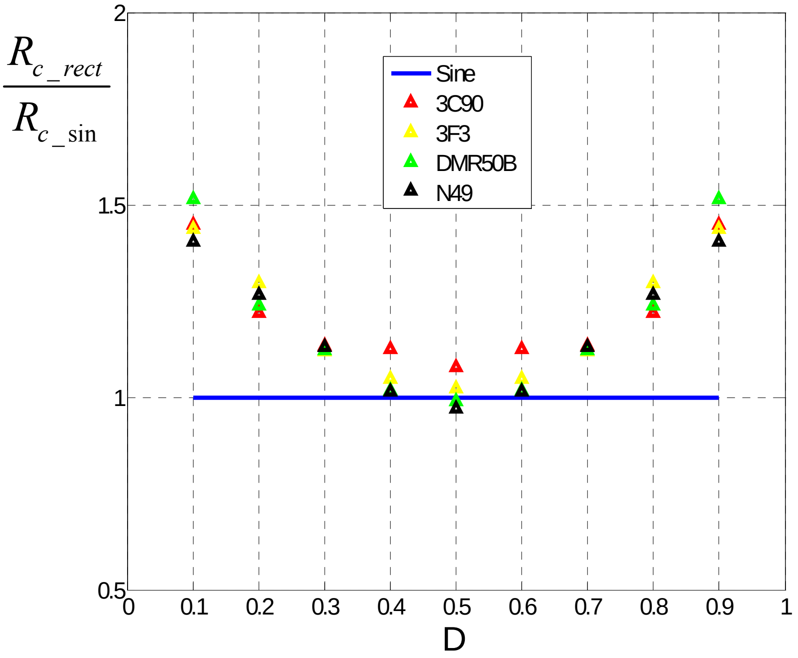

Figure 4.12 Equivalent core loss resistor (0.2MHz, RT)

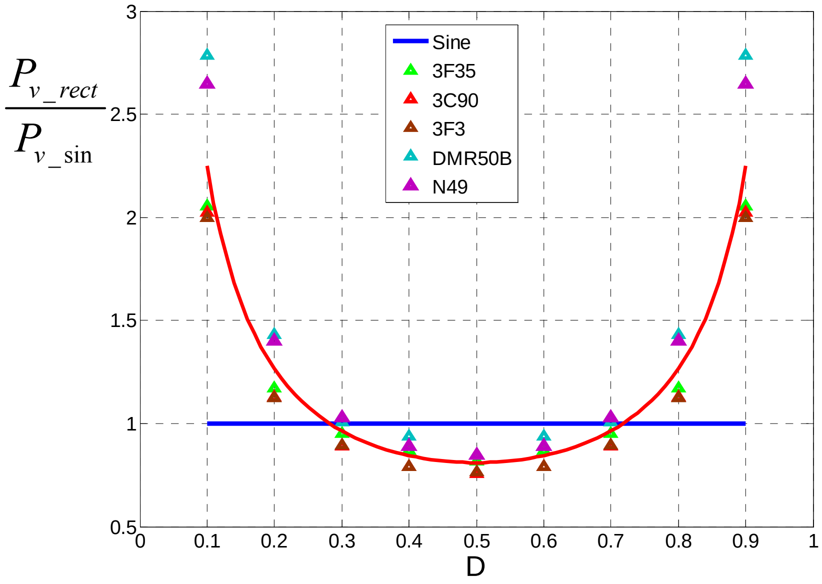

Figure 4.13 Measured core loss (0.5MHz, RT)

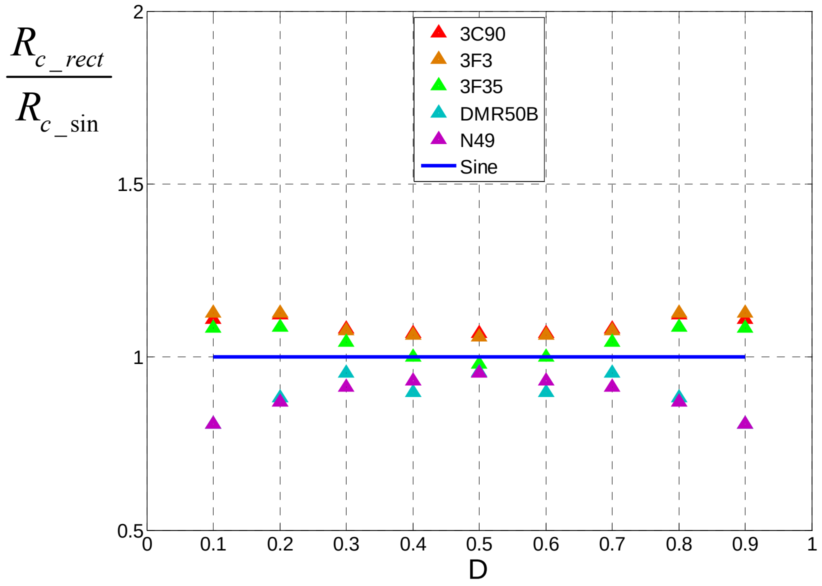

Figure 4.14 Equivalent core loss resistor (0.5MHz, RT)

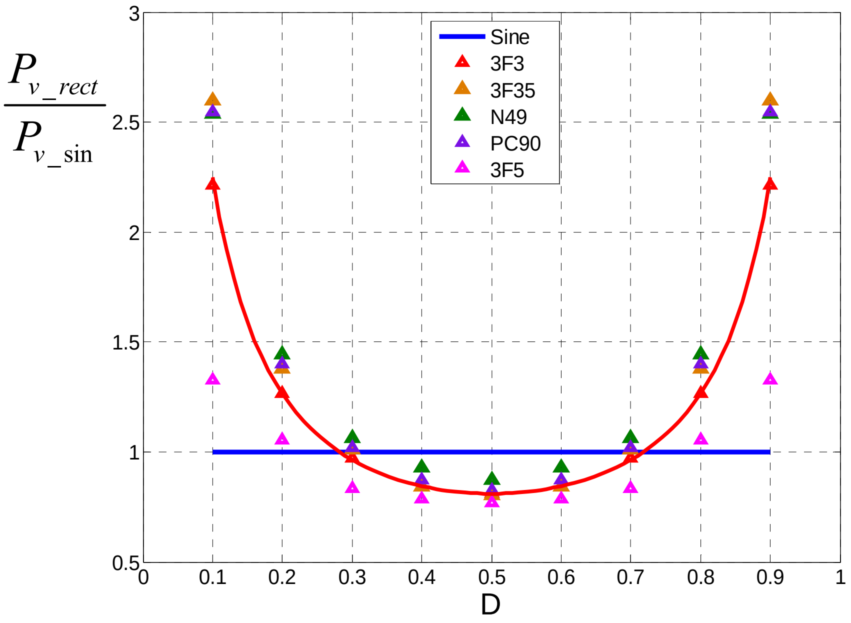

Figure 4.15 Measured core loss (1MHz, RT)

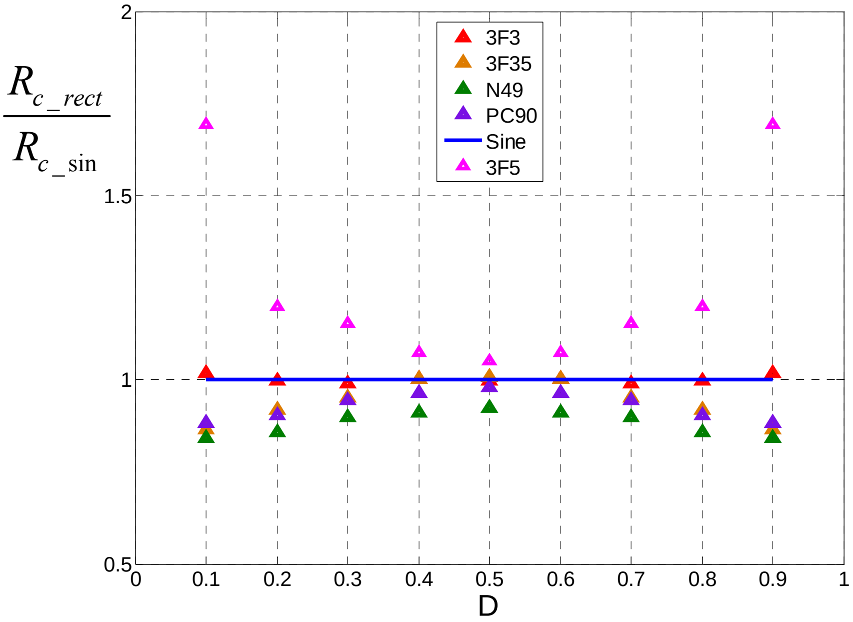

Figure 4.16 Equivalent core loss resistor (1MHz, RT)

From these measurement results, we can see the normalized equivalent core loss resistor at 50% duty cycle is always close to 1. It means at this duty cycle, the core loss can be predicted with sinusoidal loss based on the same equivalent parallel resistance. The explanation for this phenomenon is the fundamental component dominates symmetric triangular flux waveform.[19] So the equivalent core loss resistor is about the same. As the duty cycle increases or decreases, the high order harmonics components have stronger impact, which makes the normalized resistor larger or smaller than 1.

According this observation, the normalized equivalent core loss resistor can be expressed as

$$\frac{R_{c\_rect}}{R_{c\_\sin}} = [4D(1-D)]^{\gamma} \tag{4.8}$$

γ is a factor to modify the bending of the equivalent core loss resistor's shape. When the duty cycle is 50%, the normalized resistor is always 1. When $\gamma < 0$, the core loss resistor will not be smaller than 1; when $\gamma > 0$, the core loss resistor will not be larger than 1. With the normalized resistor expression, the core loss ratio between rectangular wave and sinusoidal wave can be written as

$$\frac{P_{v\_rect}}{P_{v\_\sin}} = \frac{8}{\pi^2 [4D(1-D)]^{\gamma+1}} \tag{4.9}$$

So far, the parameter γ has to be derived by fitting the measurement data. It is observed that it depends on frequency and temperature. This parameter can be provided by the manufacturers for power electronics application. With γ, the rectangular wave core loss can be calculated as

$$P_{v\_rect} = \frac{8}{\pi^2[4D(1-D)]^{\gamma+1}} kf^{\alpha} B^{\beta} \tag{4.10}$$

(4.10) is the rectangular extension of Steinmetz equation (RESE).

4.2.4 Comparison between Core Loss Models

The comparison of MSE, GSE, iGSE and RESE are shown in Fig.4.17 – Fig. 4.19.

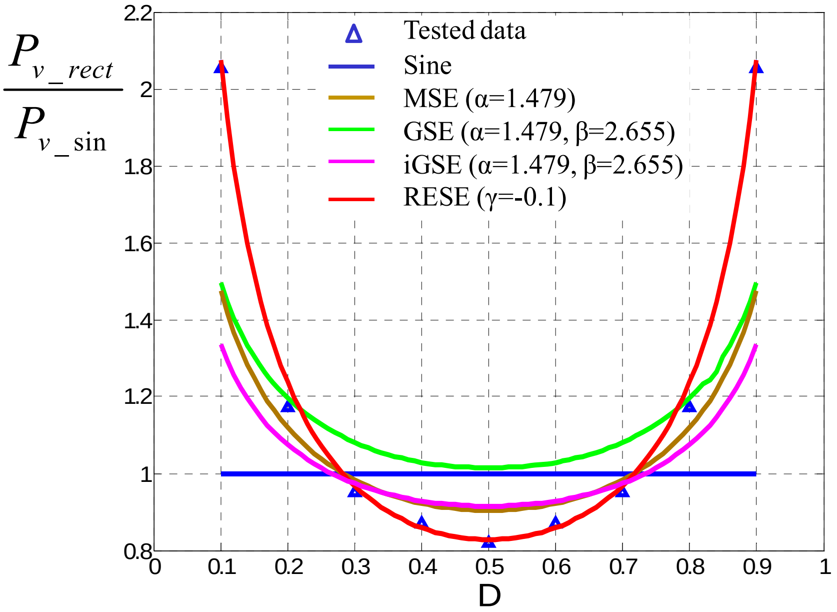

Figure 4.17 Core loss model comparison on 3F35 (0.5MHz, RT, γ= -0.1)

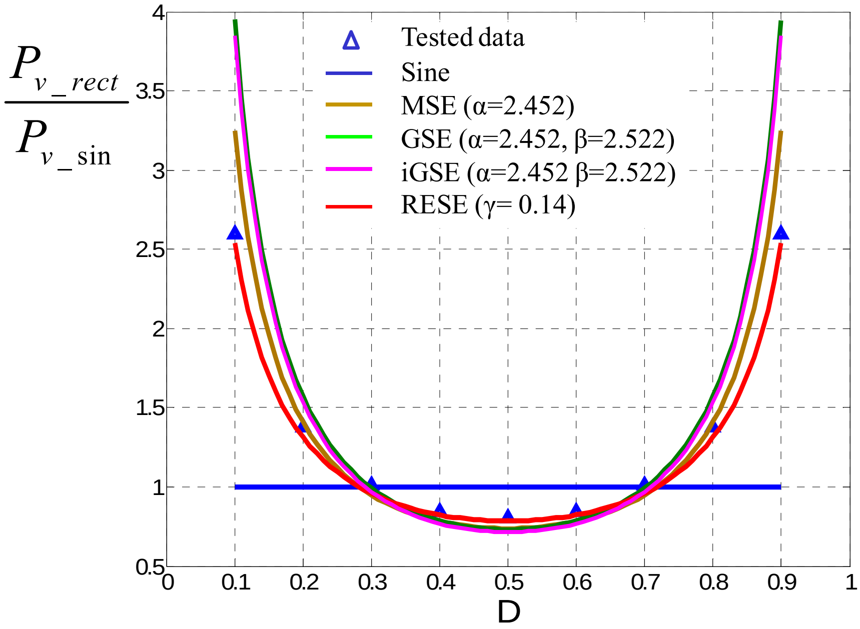

Figure 4.18 Core loss model comparison on 3F35 (1MHz, RT, γ= 0.14)

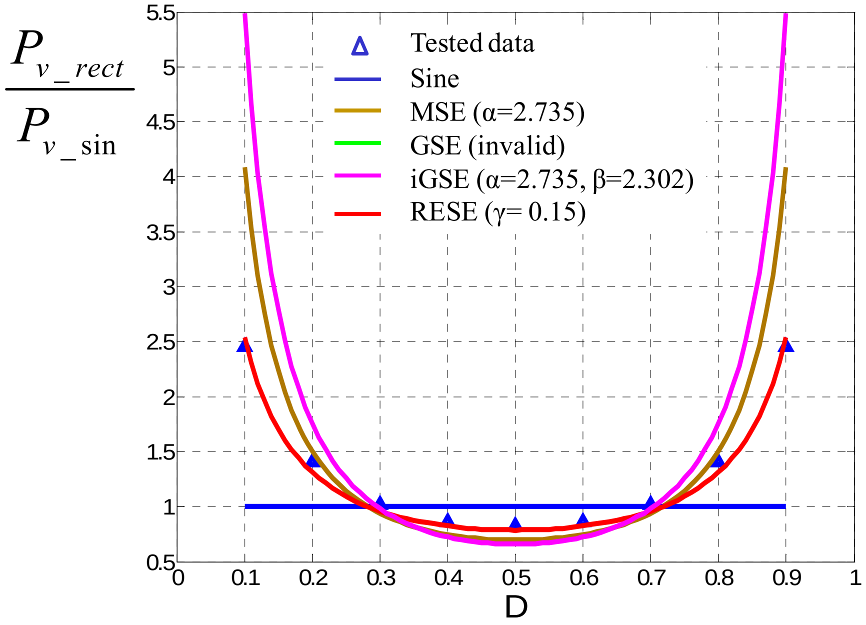

Figure 4.19 Core loss model comparison on 3F35 (1.5MHz, RT, γ= 0.15)

In Fig. 4.19, the estimation of GSE is not shown because α is larger than β so that GSE is not valid. From the comparison, we can see that the new model gives better core loss prediction.

4.3 Core Loss with Rectangular AC Voltage and DC Bias Current

The core loss under both rectangular AC voltage and DC bias is investigated in this section. In this dissertation, the core loss under bias is modeled with the DC bias field, instead of DC flux. One reason is that the incremental permeability is usually defined with the bias field, so it will be easier to analyze if the core loss density is also defined with the DC bias field. The other reason is that the DC bias field is easier to measure than DC flux density, since only DC current is required to calculate the DC bias field using Ampere’s Law. For DC flux, usually there are three ways to test it. One is integrating the voltage on the sensing winding, which requires a high-accuracy integrator. If there is remanence B_r in the core before the test, the integrated flux density will not be the correct value. The second way is testing the static B-H curve or amplitude permeability first, and multiplying the DC field H_{dc} with amplitude permeability. This approach requires additional effort to test the static B-H curve, and the B-H curve should be tested under the same environment (e.g. temperature) as the other tests. The third way is to test a gapped core. When the core’s permeability is very high, the gap determines the effective permeability. Then the DC flux can be estimated with the DC current and the effective permeability. The potential problems of this approach are: first, the gap may introduce some eddy current loss due to the fringing effect. Second, it is difficult to estimate the incremental permeability under biased condition because the effective permeability is dominated by the gap. Third, it may require large DC current to bias the core. Due to above reasons, H_{dc} is used in this model. If one wants to convert to B_{dc}, the B-H curve should be tested.

Two materials (3F35 and PC90) are investigated for rectangular AC voltage and DC bias.

4.3.1 *Test and Modeling of 3F35*

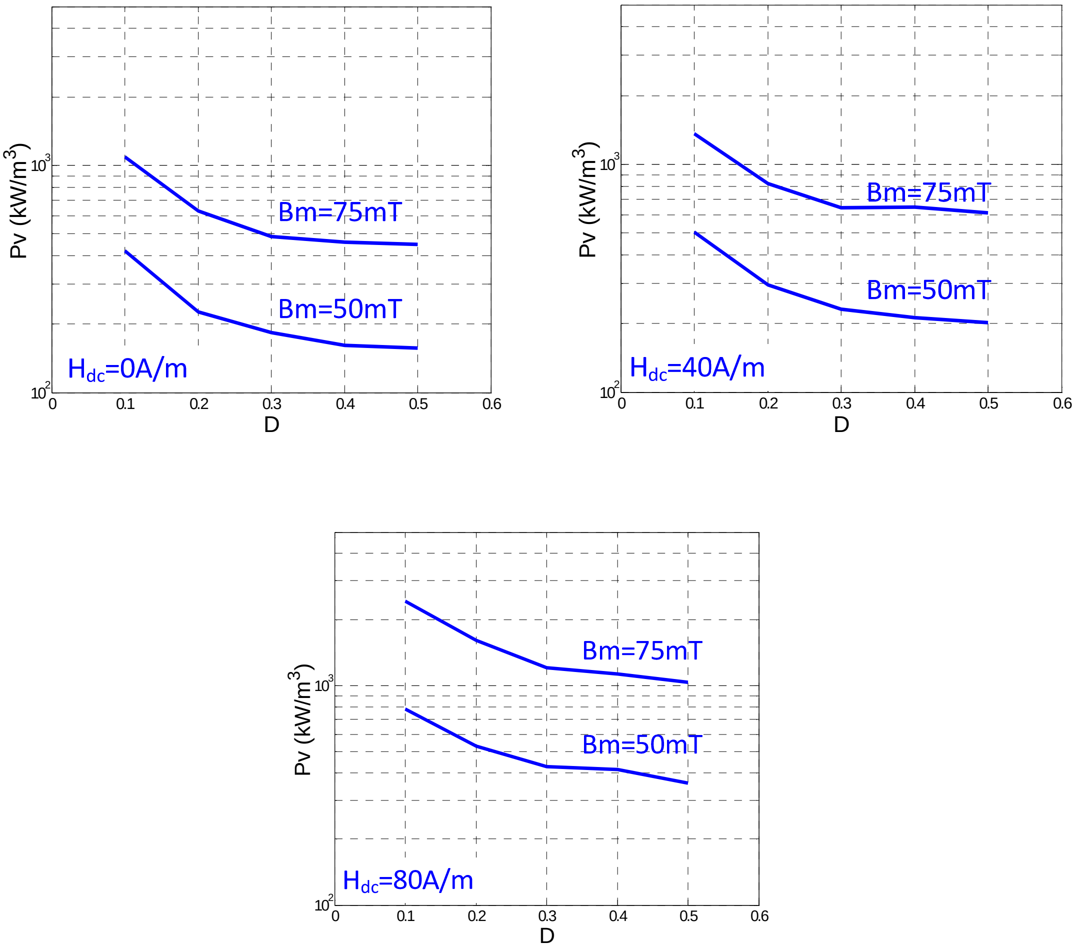

Figure 4.20 Core loss under AC rectangular voltage and DC bias

(3F35, 0.5MHz, RT)

The test results are listed in Fig.4.22. To investigate the bias's impact to the waveform factor, the waveform ratios of each flux density at each DC bias are plotted in one picture. From Fig.4.23, we can see that the DC bias will change the waveform factor, but it has limited impact. At extreme duty cycle, like 10%, the deviation is most obvious. The waveform factor will have about 20% error than the measurement.

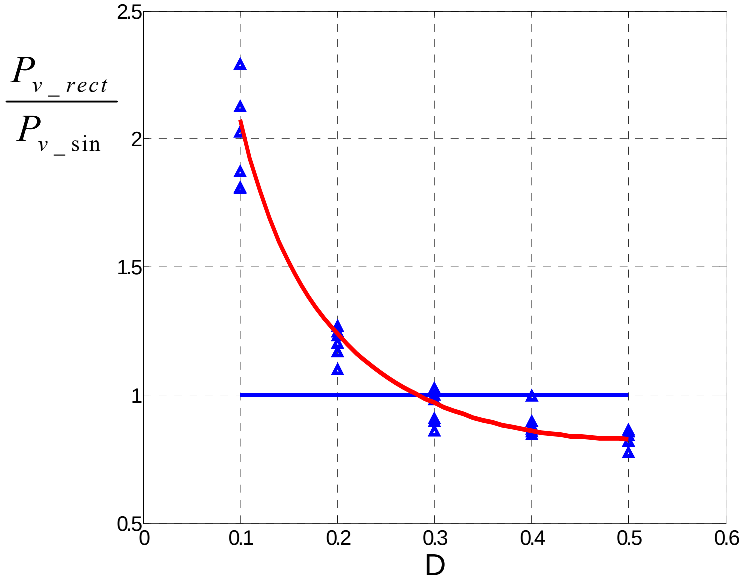

Figure 4.21 Normalized core loss vs. duty cycle

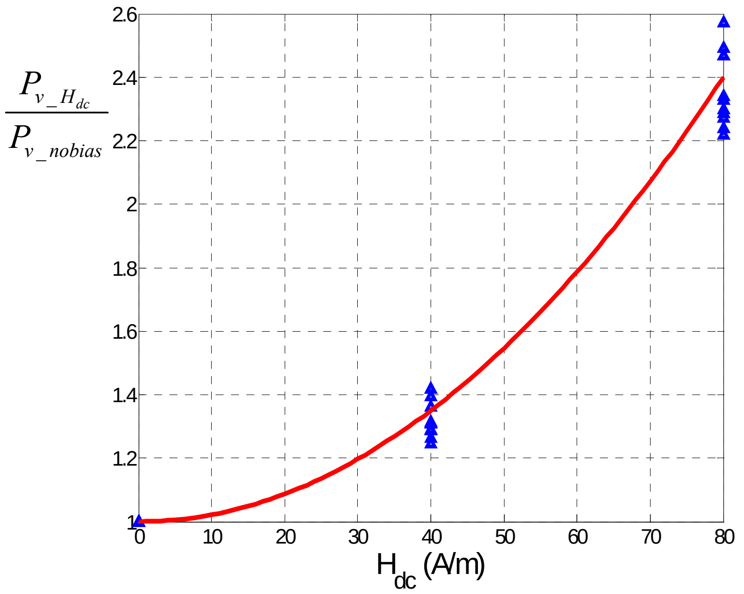

Figure 4.22 Normalized core loss vs. H_{dc}

To understand the waveform's impact to the DC bias, the core loss under bias is normalized by the core loss without bias, as shown in Fig. 4.24. It can be seen that the DC bias impacts the core loss independently in general. So it is plausible to model the core loss in the form of

$$P_v = \frac{8}{\pi^2[4D(1-D)]^{0.9}} \times kf^{\alpha} B_m^{\beta} \times F(H_{dc}) \tag{4.11}$$

The core loss generally increases with the bias field, and can be modeled as a bias factor. If use a factor function which takes H_{dc} as the parameter, the DC factor can be modeled as

$$F(H_{dc}) = 2.1875 \times 10^{-4} H_{dc}^2 + 1 \tag{4.12}$$

The factor is plotted as the red curve in Fig.4.24. The error is within 10%.

4.3.2 Test and Modeling of PC90

Another material is investigated to provide more evidence. PC90 is another MnZn ferrite which is tested as the same process above.

The core loss under rectangular wave and DC bias is plotted in Fig.2.25. We can observe the same phenomenon that the waveform and the bias affect the core loss pretty much independently.

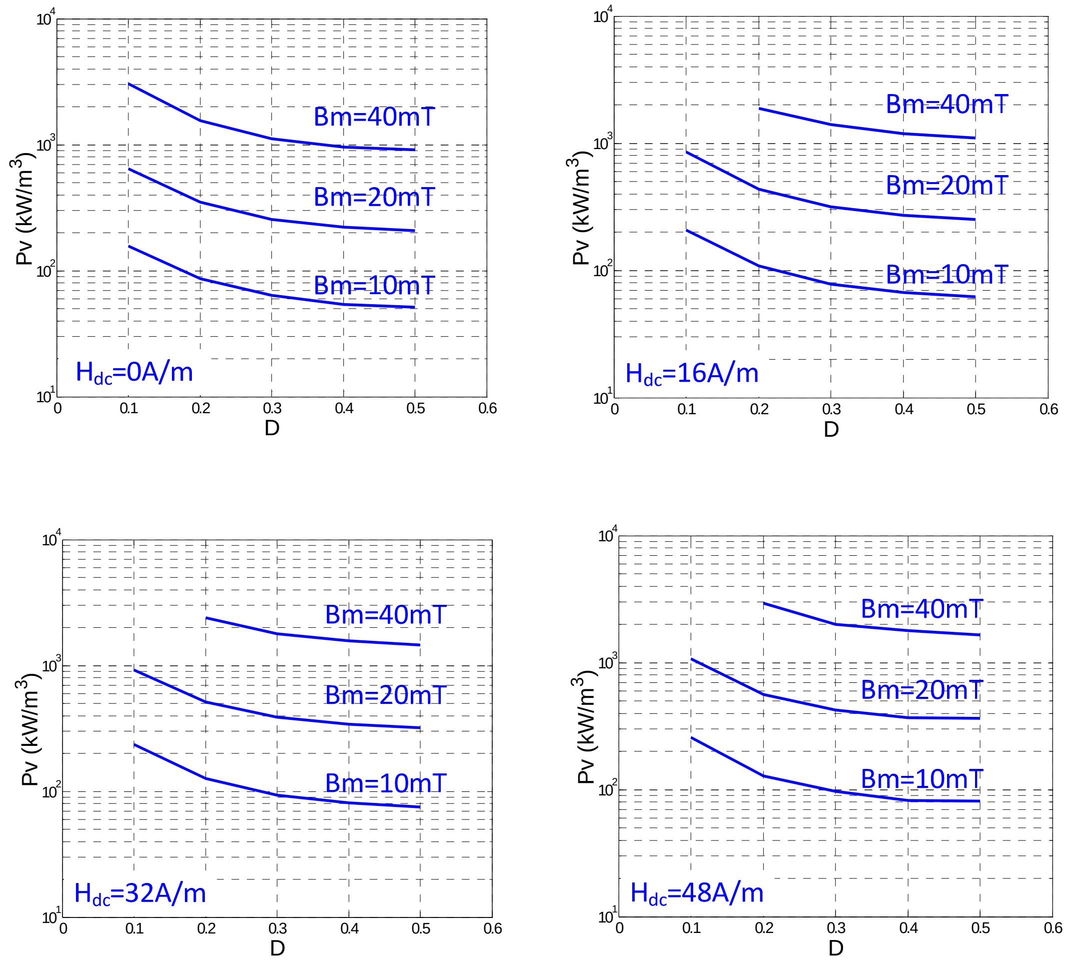

Figure 4.23 Core loss under AC rectangular voltage and DC bias

(PC90, 1MHz, 130°C)

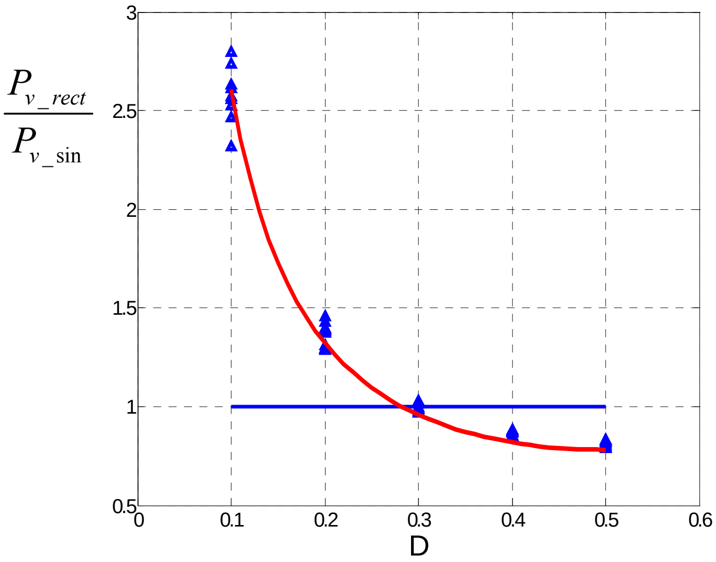

Figure 4.24 Normalized core loss vs. duty cycle

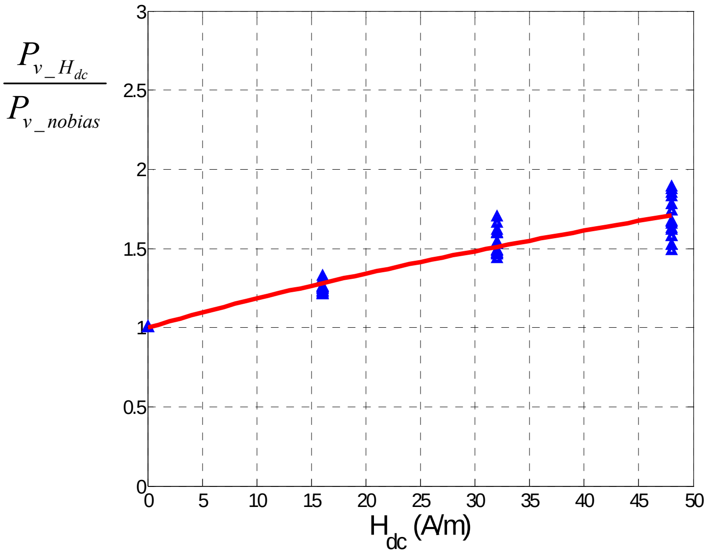

Figure 4.25 Normalized core loss vs. H_{dc}

The core loss of PC90 can also be modeled in the form of

$$P_v = \frac{8}{\pi^2 [4D(1-D)]^{1.18}} \times k f^{\alpha} B_m^{\beta} \times F(H_{dc}) \tag{4.13}$$

In which the DC bias factor can be curve fitted as

$$F(H_{dc}) = \sqrt{0.04 \times H_{dc} + 1} \tag{4.14}$$

Based on the measurement results, it can be discovered that though core loss is a quite nonlinear phenomenon, some general equations can be used to approximate it. The general equation can be in the form of

$$P_{v\_rect} = SteinmetzEqu. \times F_{waveform} \times F_{dc} \tag{4.15}$$

The waveform and DC bias has separate effect to the core loss. This is true when the AC excitation and DC bias is in relatively limited range. If take the temperature into the model, a factor governing the temperature's impact to the core loss may also be added to the general model.

Chapter Five Characterization of Low Temperature Co-fired Ceramic Ferrites and Laminated LTCC Materials

Low temperature co-fired ceramic ferrites have recently been adopted in integrated power supplies. However, the commercially available LTCC ferrites have not been fully characterized and optimized for power electronics, because they were originally targeted for RF system packaging. In this chapter, a series of commercial low-temperature co-fired ceramic ferrites from ESL Science Lab® are characterized. These ferrites are improved by laminating different tapes and co-firing.

5.1 Low Temperature Co-fired Ceramic Technology with 3D Integration

The LTCC processing technique involves screen-printing conductive pastes on the surface of tapes to form conductive patterns. This is a relatively mature technology for radio-frequency (RF) applications, and much research has been published on printing very thin conductive layers with fine pitch on LTCC tape for radio-frequency applications [69], [70]. The LTCC processing technique has better thermo-mechanical performance than traditional PCB substrate.

Table 5.1 compares the thermo-mechanical properties of LTCC and PCB. The thermal conductivity of the LTCC material is around 4, which is much better than traditional PCB material FR4 [71]. Thus, the LTCC substrate can have better thermal performance than PCB substrate. Another benefit of LTCC material is that its coefficient of thermal expansion is very close to that of silicon (CTE of silicon=3-4). Hence the mechanical stresses caused by temperature changes can be reduced when the LTCC components are integrated with silicon components, which can improve the reliability of the integrated module. Furthermore, as a thick film technology, it is very easy to use LTCC technology to fabricate a sufficiently thick magnetic core and winding for high-current applications. In summary, LTCC technology has thermo-mechanical properties suitable for integrating with silicon, and is a promising technique for low-profile electronics. It also has potential for use in low-profile magnetic integration for high-current applications. Therefore, there are many researchers exploring LTCC for power electronics applications.

Table 5.1 Thermal conductivity and CTE of LTCC and FR4

	LTCC	FR4
Thermal conductivity (W/m°C)	2-5	0.3
CTE (ppm/°C)	4-8	17

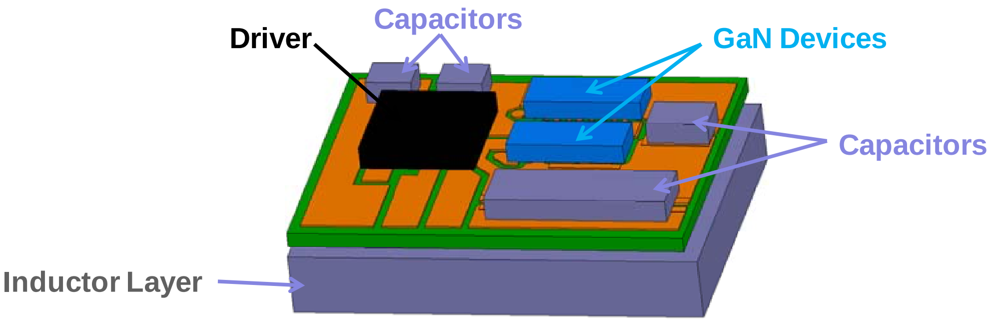

Figure 5.1 3D integrated converter with LTCC substrate

The 3D integration is an emerging structure for power converters [73]- [76]. The active devices are stacked on a magnetic substrate to reduce the footprint and the power density of the converter. To further increase the power density of the 3D integrated converter, lateral flux planar inductors are proposed. Some works on different LTCC magnetic substrate structures for high–frequency, high-current converters have been reported [73]-[76]. The planar magnetic substrate with lateral flux pattern has the advantages of a low profile and nonlinear inductance under light-load conditions. One significant difference between this structure and conventional design is that the area that the flux passes through is very wide. Another difference is that the structure doesn't have an air gap. The flux is confined in the magnetic core, so it undergoes less of fringing effects and fewer EMI problems. The absence of a discrete air gap makes the core easier to saturate, especially in the center space. Thus the inductor is non-linear, and its properties change with different load conditions. The unit cell of the low-profile magnetic substrate structure in [75] is shown in Fig. 5.2(a). When a high DC current flows through the conductor in the middle, the DC pre-magnetization condition in the core is very non-uniform, as the simulation result shown in Fig. 5.2(b). If the DC current is 10A, the maximum H_{dc} in the core structure is about 2700A/m, while the minimum is 500A/m. As we know, the permeability and core loss density is affected by the pre-magnetization [32], [33], [34], [52]. Therefore, to accurately estimate the nonlinear inductance and core loss of the structure, the characteristics of LTCC materials should be measured under wide pre-magnetization conditions.

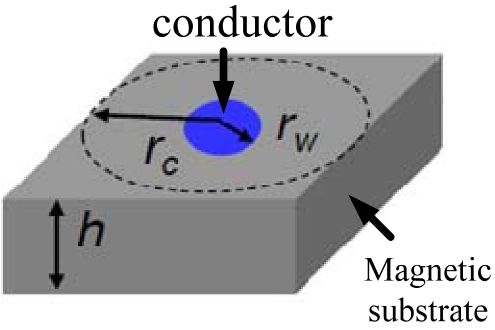

(a) Unit cell of lateral flux structure inductor

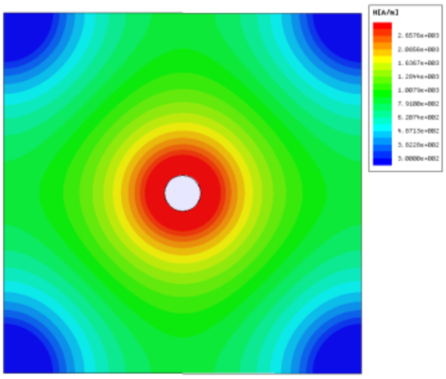

(b) Non-uniform field distribution (top view)

Figure 5.2 Low-profile magnetic substrate structure

5.2 Characterization of Low-temperature Co-fired Ceramic Ferrites

We used commercialized LTCC ferrite tape materials from ESL ElectroScience®: 40010, 40011 and 40012 [72]. When designing an inductor or transformer, the proper material should be chosen first based on its material property, but this process has not been thoroughly discussed in previous LTCC designs. Before choosing the proper material, the magnetic properties of these materials should be characterized and compared.

5.2.1 LTCC Sample Preparation

The property of the LTCC sample depends on its preparation process [72]. For example, a different sintering temperature will affect the permeability of the LTCC material. As shown in Fig. 5.3, as the sintering temperature increases, the permeability also increases.

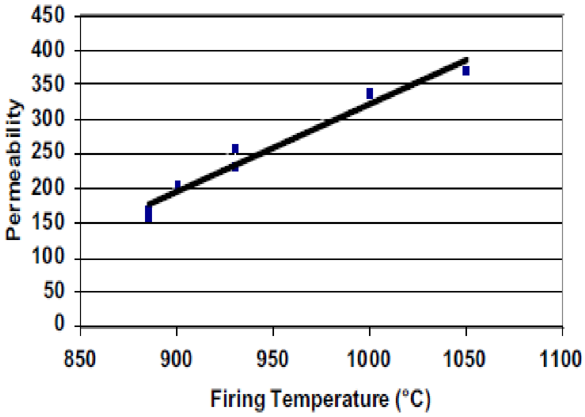

Figure 5.3 Permeability increases with sintering temperature [72]

The samples characterized in this paper are prepared following the process illustrated below. The process starts with the green tape purchased from ESL®. The green tape is cut into small squares and stacked together. The stack is then mechanically pressed into a single bulk unit at 2000psi and 70°C for 15 minutes. After that, the pressed bulk is cut into a thin toroid core shape with a laser cutting machine. The process for un-sintered samples is shown in Fig. 5.4. After the shape is ready, the samples are put into an oven and sintered following the profile in Fig. 5.5. A picture of the sintered sample is shown in Fig. 5.6. The width of the sample is thin enough so that the flux density in the core can be assumed to be uniform.

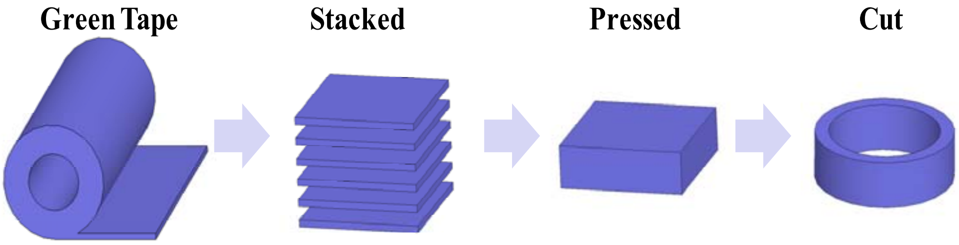

Figure 5.4 Process to prepare the un-sintered LTCC core sample

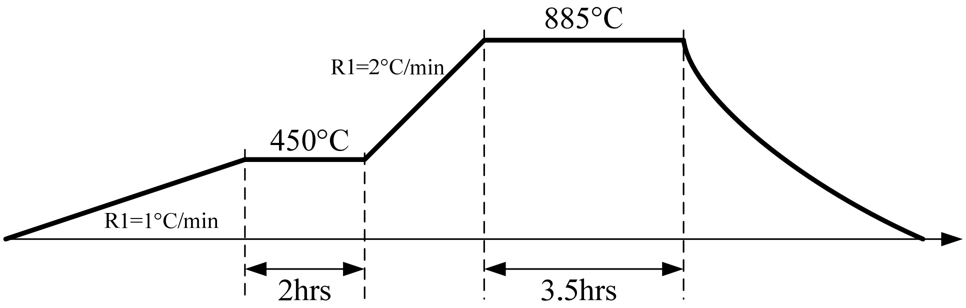

Figure 5.5 Sintering profile

Figure 5.6 Sintered core sample

5.2.2 *Magnetic Characteristics of LTCC*

The measured relationship between incremental permeability and DC pre-magnetization field strength H_{dc} is illustrated in Fig. 5.8. It can be seen that the initial relative permeability for LTCC materials 40010, 40011 and 40012 are close to 50, 200 and 500, respectively. As H_{dc} increases, their incremental permeabilities decrease. LTCC 40012 has the highest initial permeability, but its permeability decreases fastest. LTCC

40010 has the lowest initial permeability, but the permeability decreases more slowly than the other two. From the measured permeability, we can see that though a low-permeability LTCC material has the lowest μ when there is no DC bias; its permeability is higher when H_{dc} is higher than a certain point. LTCC 40012 has the highest permeability below 200A/m, and LTCC 40012 has the highest permeability over 800A/m. LTCC 40011 is the highest in the window of 200-800 A/m. LTCC 40012 has the least distributed air gap, so the material has the top initial permeability but saturates fastest. LTCC 40010 has the largest amount of distributed air gap, so it has the lowest initial permeability but is less vulnerable to high magnetic field bias. For transformers or low-current inductors, LTCC materials 40012 and 40011 would be good candidates, considering their high permeability when there is no bias or low bias. For inductors in high-current converters, LTCC 40010 would be a better choice in terms of inductance density.

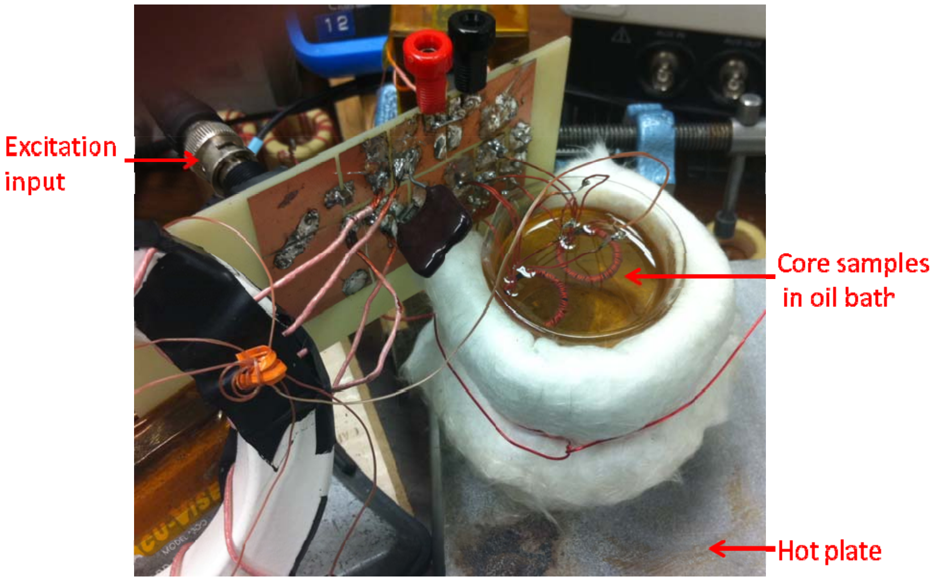

Figure 5.7 Measurement setup

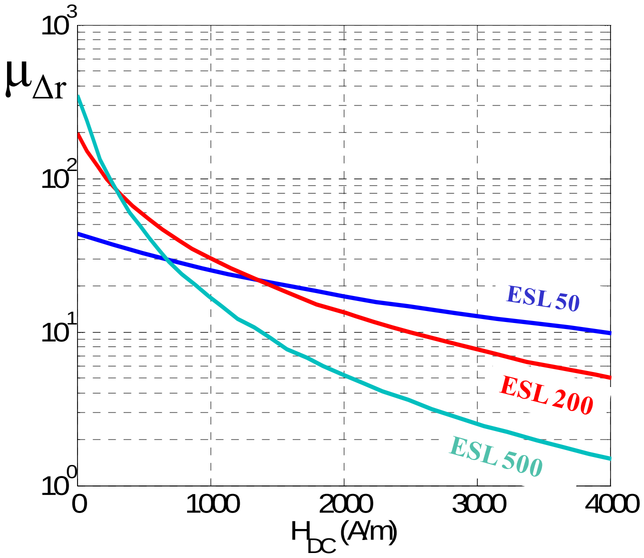

Figure 5.8 Incremental permeability for different values of H_{dc}

The measured core loss density of three types of LTCC materials are shown in Fig. 5.9. The measured frequency is 1.5MHz, 3MHz and 5MHz. Their core loss is benchmarked with NiZn ferrite 4F1 from Ferroxcube®. From the measured core loss density, we can see that LTCC 40012 is a better choice for lower frequency applications. At 1.5MHz, its core loss is as low as that of LTCC 40010, so its high permeability means it surpasses the other two for applications under 1.5MHz. From the core loss density curves at 3MHz and 5MHz, we can see that the loss curves of LTCC 40011 and LTCC 40012 rise further and further away from the curve of benchmark 4F1 as the frequency increases, which means that LTCC 40011 and LTCC 40012's loss density increase rapidly with frequency. LTCC 40010's loss density is comparable to that of 4F1 NiZn ferrite, and its curve sticks to 4F1's even at 5MHz. Thus LTCC 40010 is suitable for high-frequency applications.

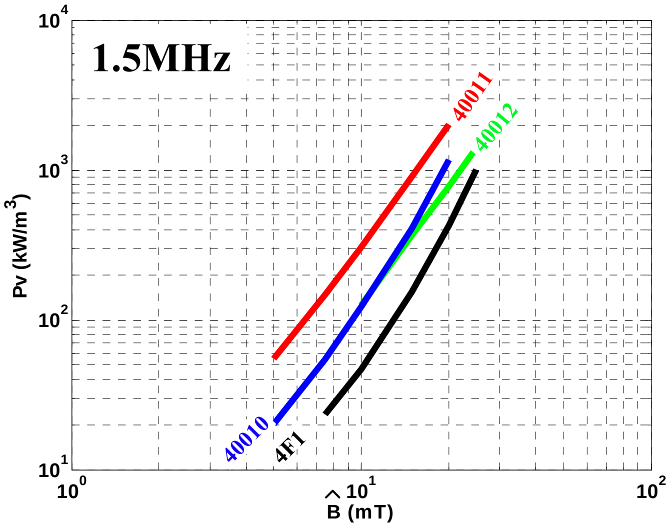

(a) 1.5MHz

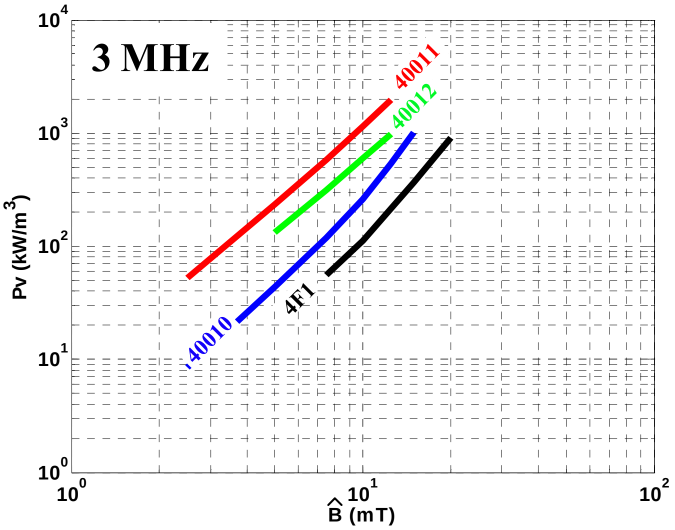

(b) 3MHz

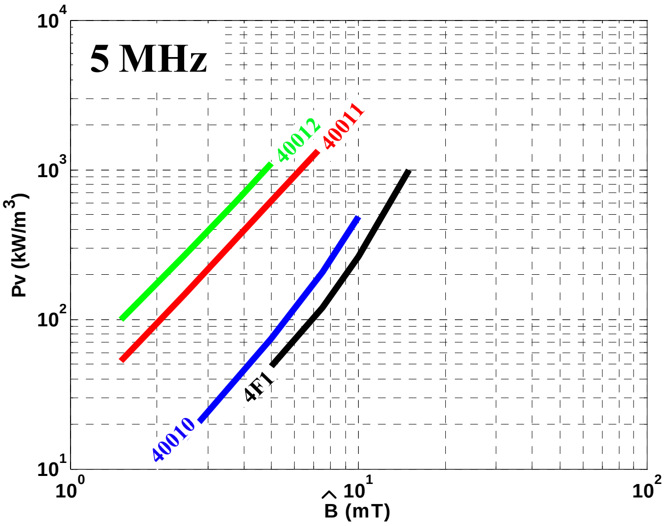

(c) 5MHz

Figure 5.9 Core loss comparison between LTCC 40010, 40011, 40012 and 4F1 at 1.5MHz, 3MHz, and 5 MHz

The relationship between core loss density and the DC magnetic field is shown in Fig. 5.10. The AC excitation is kept at a 1.5MHz sinusoidal curve, and the AC flux density is kept constant on each curve. The measured data shows that the core loss density changes with DC pre-magnetization, and in general the core loss increases with the DC bias. For the same AC flux density, LTCC 40010 and LTCC 40012 simply have higher loss when H_{dc} is higher. LTCC 40011's core loss density first decreases then increases as H_{dc} increases. The core loss near saturation may become 3 or 4 times higher than when there is no bias.

According to the permeability and core loss density information, LTCC 40010 is the best choice for high-current inductors in converters over 1.5MHz.

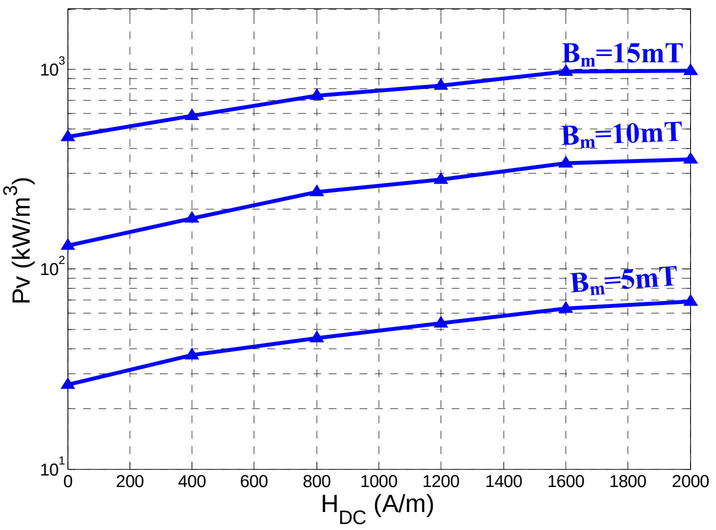

(a) 40010

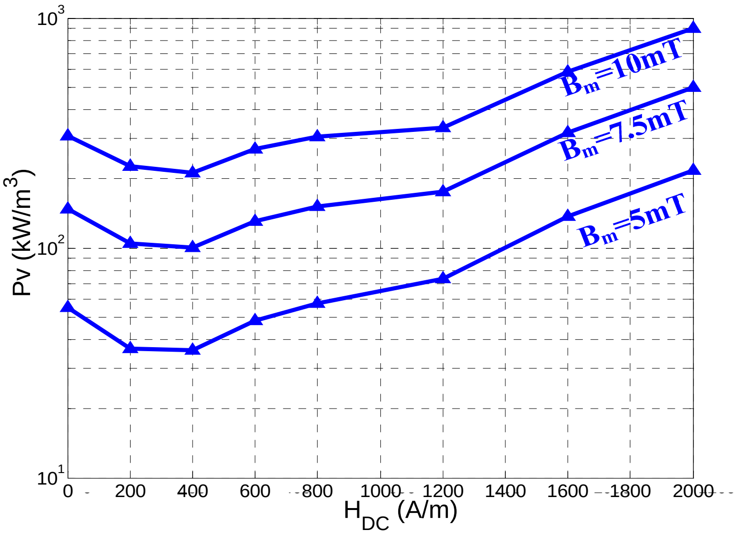

(b) 40011

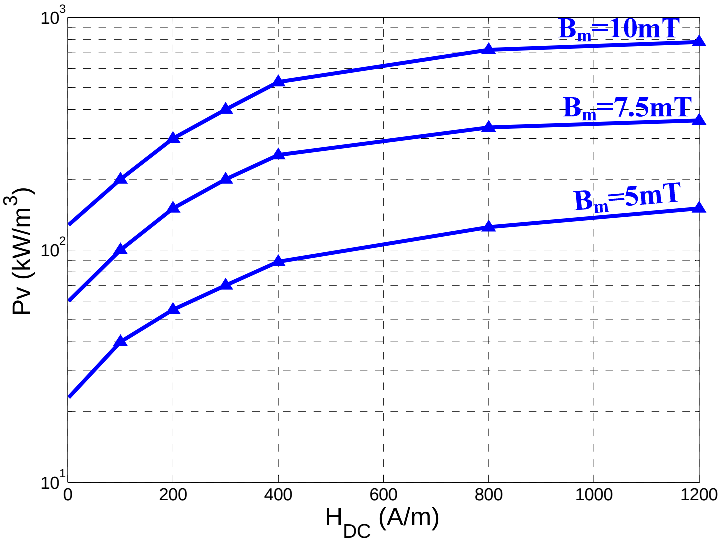

(c) 40012

Figure 5.10 Core loss density as a function of H_{dc} (AC is at 1.5MHz)

The magnetic characteristics of low-temperature co-fired ceramic ferrite tapes 40010, 40011 and 40012 from ESL® are measured at 1.5MHz, 3 MHz, and 5 MHz, respectively. The DC bias magnetic field is pushed up to 2000A/m. According to measurement data, LTCC 40012 is more suitable for low-frequency transformers, coupled inductors, or low-current inductors. LTCC 40010 is a good candidate for applications with high frequencies and high current. LTCC 40011 is an intermediate choice between the two.

5.3 Laminated LTCC Ferrite

5.3.1 The Concept and Microstructure

According to the simulation in Fig. 5.2(b), for a 10A planar lateral flux inductor, the major part of the core is bias in the range of 1000A/m to 3000A/m. During this bias range, LTCC 40010 starts with a higher permeability than the other two materials. However, if we can find another material which has the same saturation flux but somewhat higher initial permeability than LTCC 40010's, we can expect that the new material will have a higher permeability than all three commercial materials in the desired range. Mixing different LTCC material can be a good way to get a medium permeability. Because the commercial material is in the form of green tape, we can laminate the two types of material and co-fire them. Fig. 5.11 shows the laminated structure made by LTCC 40012 and 40010.

Figure 5.11 Lamination of different LTCC tapes

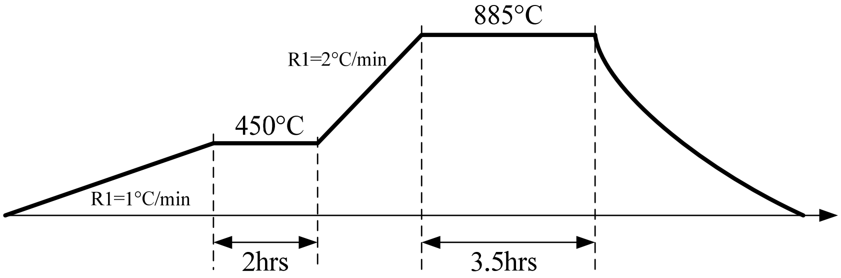

Figure 5.12 Original sintering profile

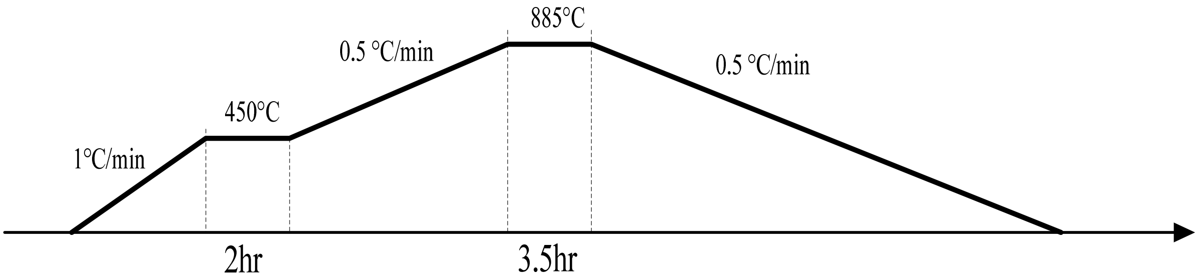

Figure 5.13 Modified sintering profile if necessary

During the sintering, the shrinkage of the two LTCC tapes is not the same, though they are provided by the same manufacturer. When their shrinkage is not the same, it causes internal stress, which can cause the material to de-laminate. One solution to tackle this problem is reducing the temperature ramp, which can slow the release of the stress. The original slope is 2°C/min, the modified slope is 0.5°C/min. Sometimes, pressure may need to be applied during the sintering to prevent de-lamination.

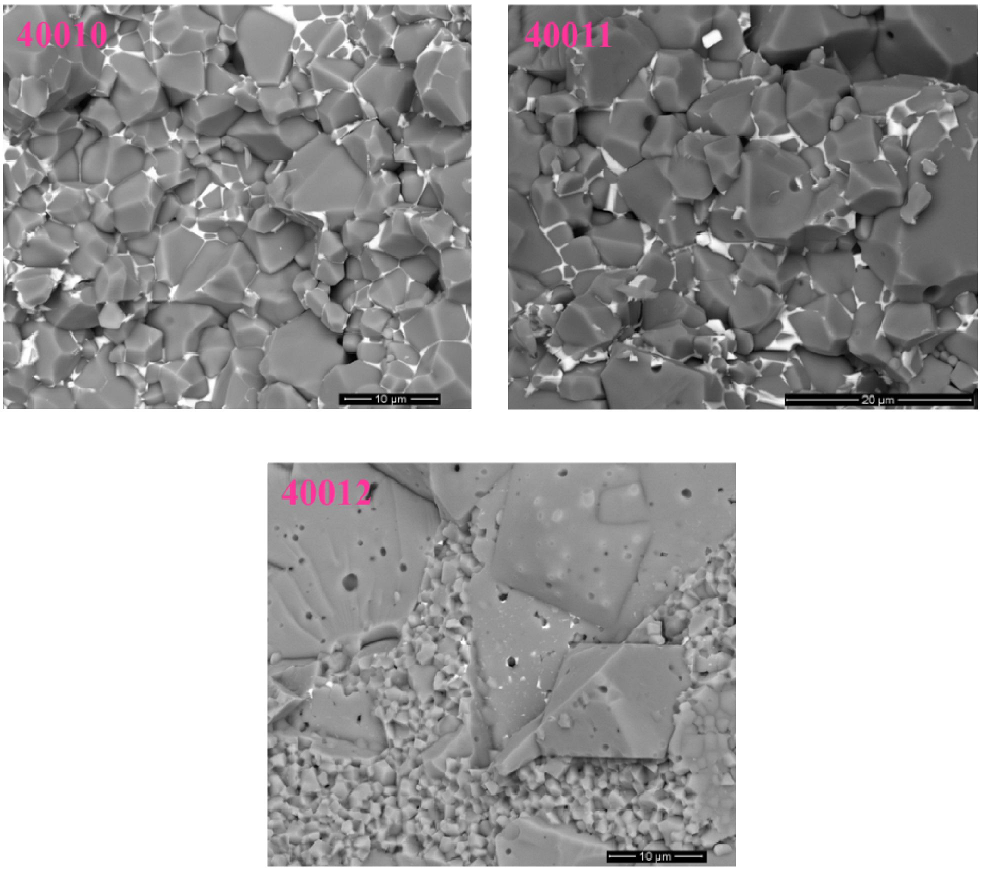

Figure 5.14 Microstructure of ESL ferrite tapes sintered at 885°C for three hours (back scattering electron images on cross-section of the samples).

To check the uniformity of the new material, its composition is investigated. The energy-dispersive X-ray spectroscopy (EDS) results demonstrate that all examined tapes are NiCuZn ferrites with different amounts of Bi_2O_3 additives. All three materials can be expressed by the general formula $x(Ni_aZn_bCu_{1-a-b})Fe_2O_4 + (1-x)Bi_2O_3$. Bi_2O_3 is used because it can form eutectics with NiO, CuO, ZnO, and Fe_2O_3 in the relatively low temperature range of 700 - 870°C. Therefore, the use of Bi_2O_3 additives can effectively reduce the sintering temperature for NiCuZn ferrites from 1250°C to around 900°C by virtue of the liquid phase sintering mechanism. The measured chemical composition of ESL low-fire ferrite tapes is summarized in Table 5.2. The ratios of Ni:Cu:Zn for each material are calculated from the EDS results. It is observed that the 40011 and 40012 tapes have very similar ferrite composition, but the ferrites in LTCC 40011 are mixed with more Bi_2O_3 sintering additives than in LTCC 40012, as shown in scanning electron microscope (SEM) images in Fig. 5.14.

Table 5.2 Composition of ESL's LTCC and laminated LTCC

Ferrite Tape	Ni	Cu	Zn
40010	0.44	0.18	0.38
40011	0.25	0.12	0.63
40012	0.25	0.11	0.64
40010/40012 (1:1)	0.35	0.15	0.50

Figure 5.15(a) shows the cross-sectional microstructure of a sintered laminate with alternating layers of 40010 and 40012 tapes in a 1:1 ratio. No obvious boundaries are seen between the different layers. In addition, it is confirmed that Bi is dispersed evenly in both the 40010 and 40012 tape layers after sintering, which is clearly shown in Fig.

5.15(b). The diffusion of Bi increases the sintering compatibility between the 40010 and 40012 tapes for the laminate.

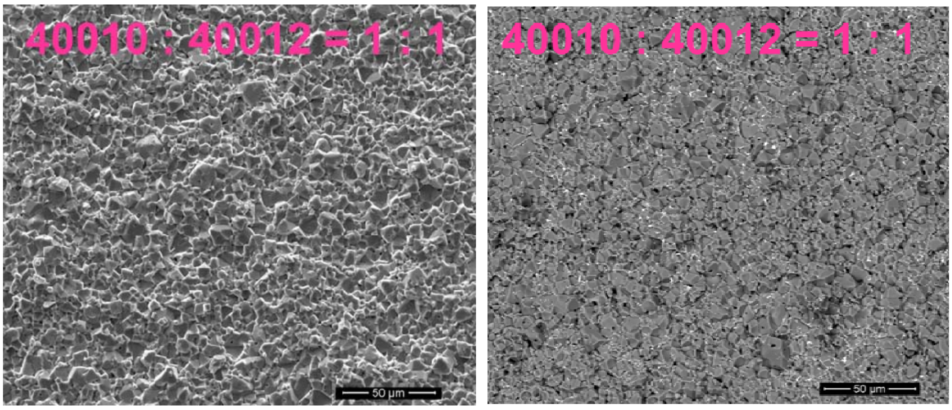

(a) (b)

Figure 5.15 Microstructure of a laminate with alternating layers of 40010 and 40012 in a 1:1 ratio (a) SE image (b) BSD image

As discussed above, laminating two different tapes together mixes different LTCC ferrites, and their permeability and core loss will change accordingly. There are a lot of combinations of laminated materials. There are three LTCC materials, so each of them can be combined with another to create a new material. The ratio of the two materials can be adjusted, perhaps in ratios of 1:1, 1:2, or 1:3, etc. Several combinations are investigated to find the best one for the 3D integration. The combinations tested are:

A. 1 layer LTCC 40010 and 1 layer LTCC 40012

B. 2 layer LTCC 40010 and 1 layer LTCC 40012

C. 1 layer LTCC 40011 and 1 layer LTCC 40012

D. 1 layer LTCC 40010 and 1 layer LTCC 40011

Each of the combinations creates a new material that new material is fabricated and tested. Their magnetic characterizations are shown in Fig. 5.16- Fig. 5.23. To distinguish the new material from ESL's LTCC, the new materials are labeled with L-LTCC and their initial permeability. Thus the combinations A, B, C, and D listed above are named L-LTCC 80, L-LTCC 70, L-LTCC 200 and L-LTCC 90, respectively.

5.3.2 L-LTCC 80 (1 layer LTCC 40010 and 1 layer LTCC 40012)

L-LTCC 80 is a combination of ESL LTCC 40010 and LTCC 40012 in a 1:1 ratio. Its permeability is higher than that of LTCC 40010 up to 4000A/m under the bias field. Hence L-LTCC 80 can further reduce the volume of 40010 if the inductance is kept the same. In term of core loss density, L-LTCC 80 and LTCC 40012 show the same core loss density of 1.5MHz, which is a little higher than that of LTCC 40010, but L-LTCC 80 has much lower core density than LTCC 40012 at 3MHz and 5MHz. Considering its high permeability and low core loss density, L-LTCC 80 is a better material than LTCC 40010 for high-frequency POL applications that operate at frequencies of 1MHz to 3MHz.

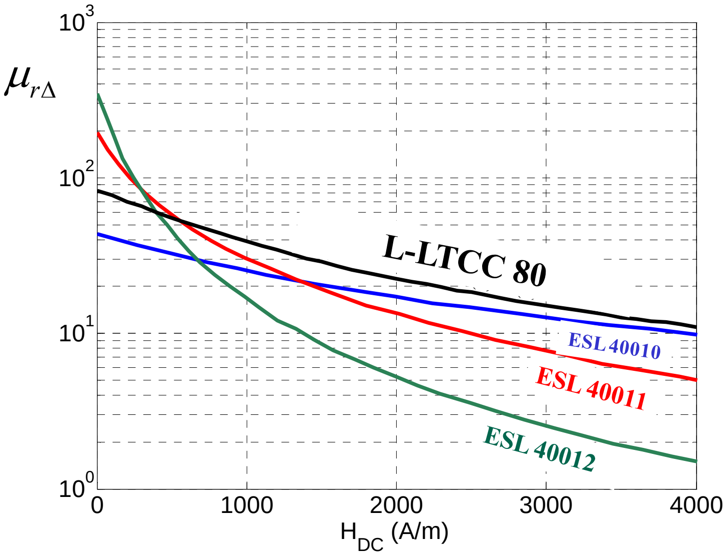

Figure 5.16 Permeability of laminated LTCC

(1 layer LTCC 40010 and 1 layer LTCC 40012)

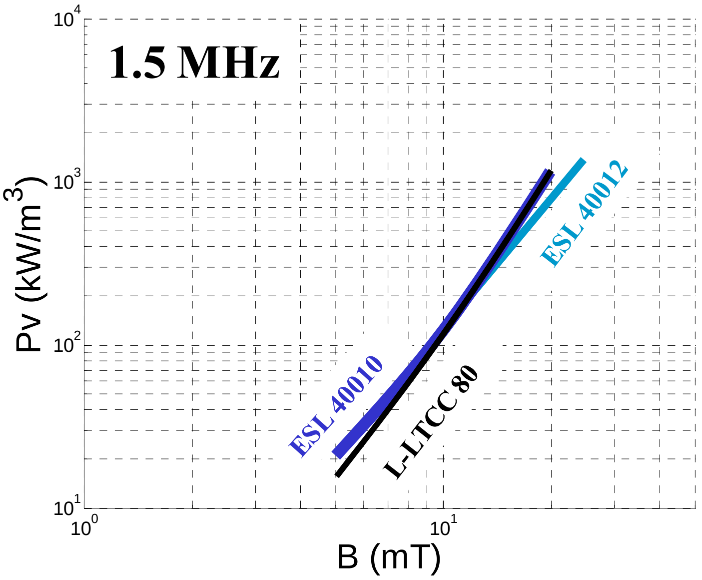

(a) Core loss at 1.5 MHz

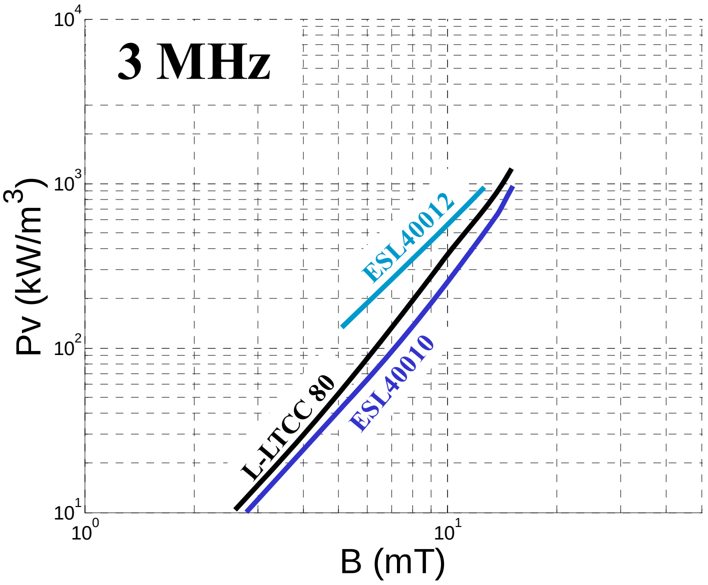

(b) Core loss at 3 MHz

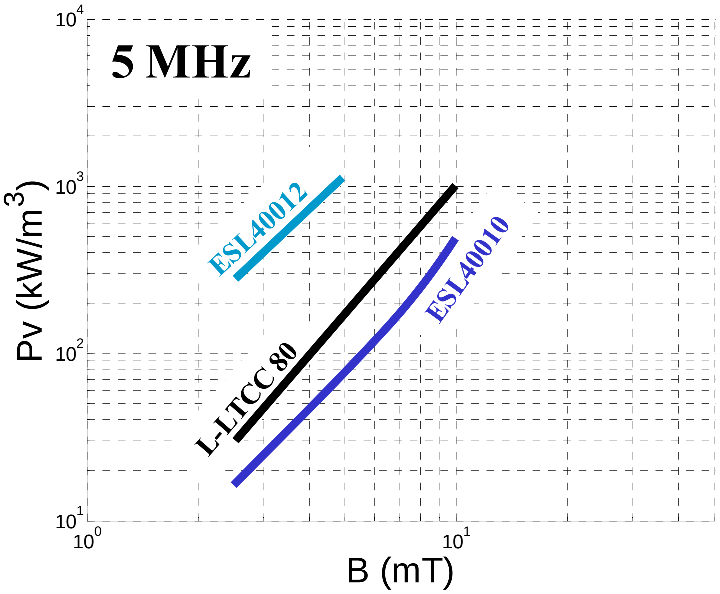

(c) Core loss at 5 MHz

Figure 5.17 Core loss density of laminated LTCC

(1 layer LTCC 40010 and 1 layer LTCC 40012)

5.3.3 L-LTCC 70 (2 layer LTCC 40010 and 1 layer LTCC 40012)

L-LTCC 70 is the product of two layers of LTCC 40010 and one layer of LTCC 40012. L-LTCC 70 has almost the same core loss density as L-LTCC 80, but it has a lower incremental permeability under a bias condition. Its overall properties are not as good as those of L-LTCC 80, but it still has some advantages over LTCC 40010.

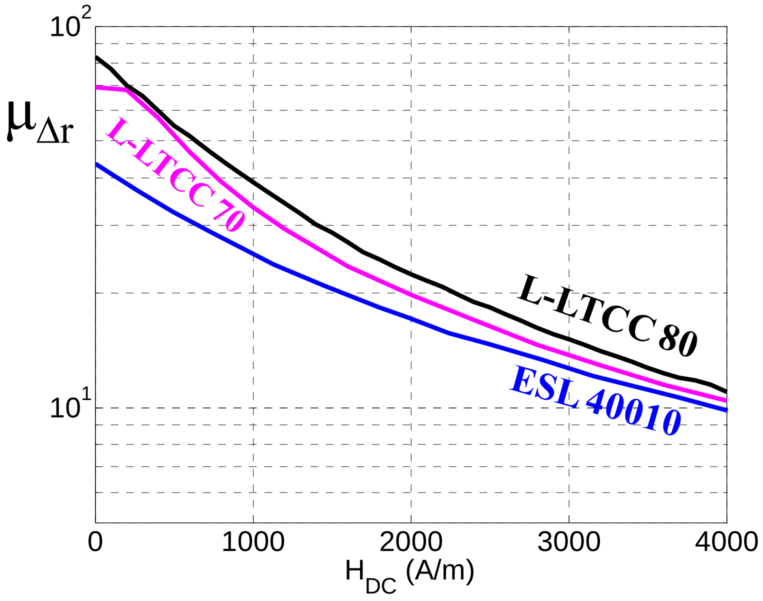

Figure 5.18 Permeability of laminated LTCC

(2 layers LTCC 40010 and 1 layer LTCC 40012)

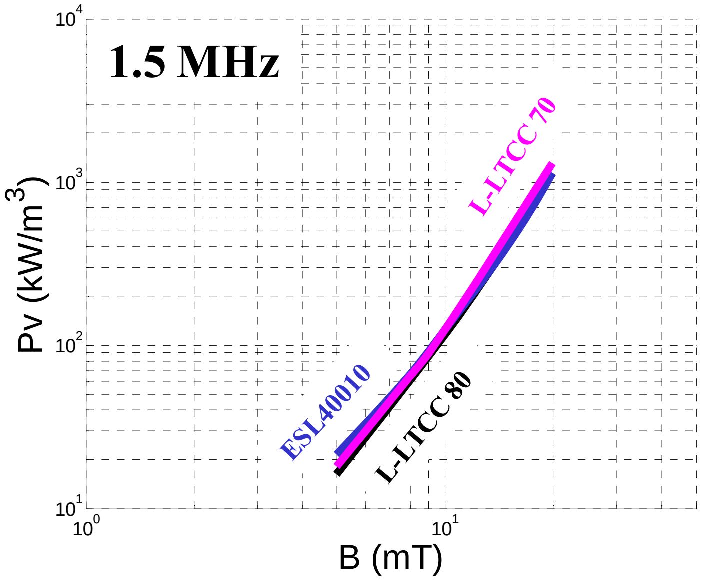

(a) Core loss at 1.5 MHz

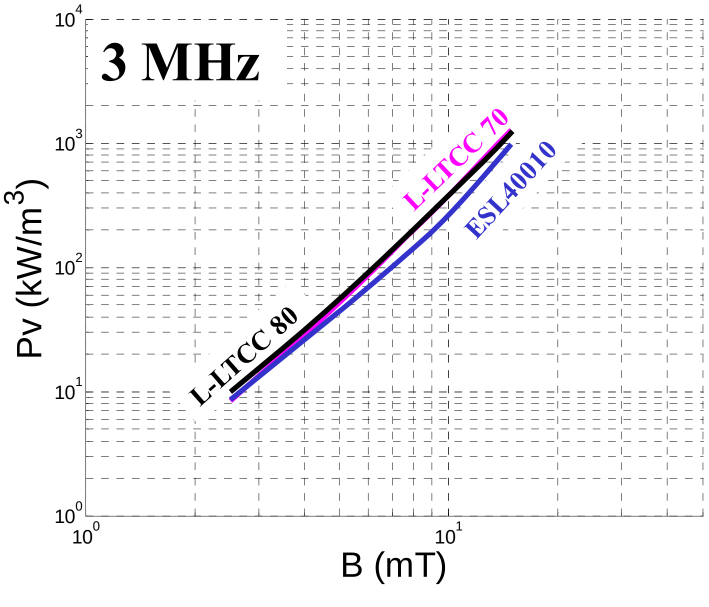

(b) Core loss at 3 MHz

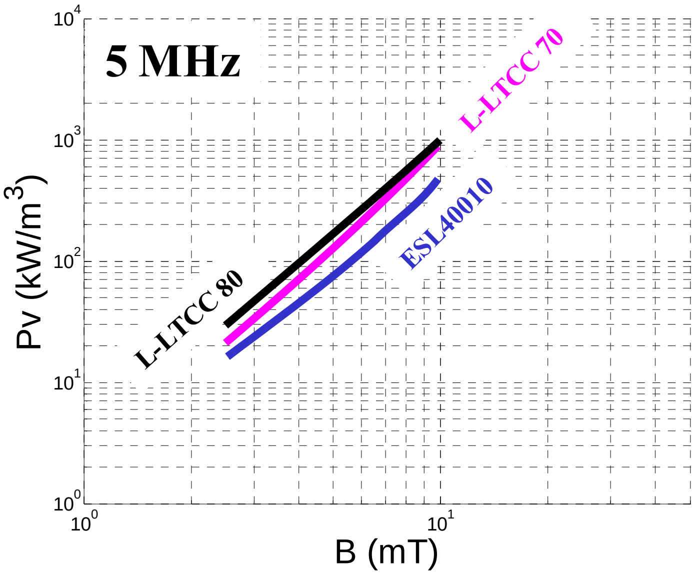

(c) Core loss at 5 MHz

Figure 5.19 Core loss density of laminated LTCC

(2 layers LTCC 40010 and 1 layer LTCC 40012)

5.3.4 LTCC 200 (1 layer LTCC 40011 and 1 layer LTCC 40012)

L-LTCC 200 is fabricated by laminating one layer of LTCC 40011 and one layer of LTCC 40012. It is almost the same as LTCC 40011. This can be explained by the same composition ratios of Ni, Cu, Zn of LTCC 40011 and 40012. The different content of Bi_2O_3 makes the two have different property. It seems that mixing the two make the new material closer to LTCC 40011.

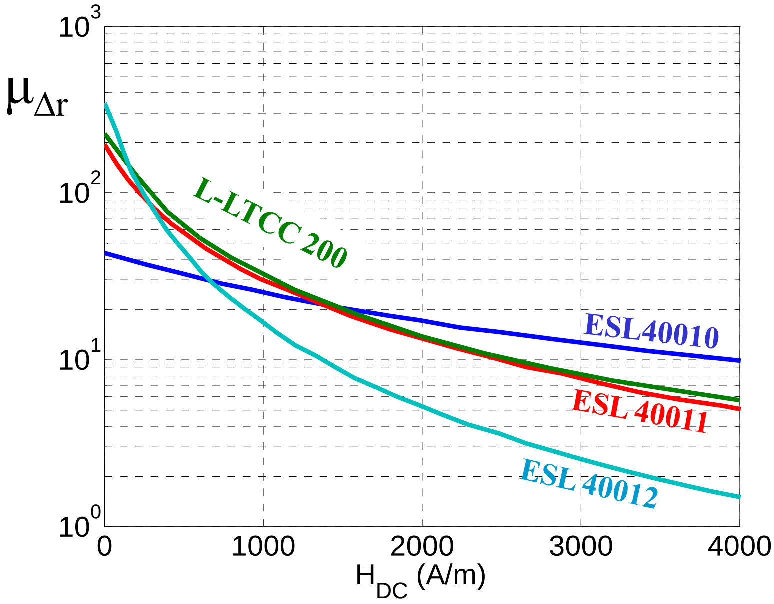

Figure 5.20 Permeability of laminated LTCC

(1 layer LTCC 40011 and 1 layer LTCC 40012)

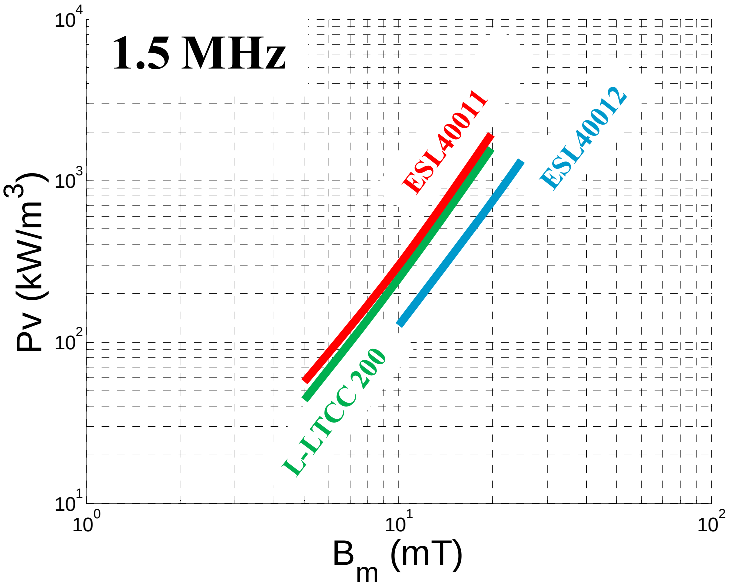

(a) Core loss at 1.5 MHz

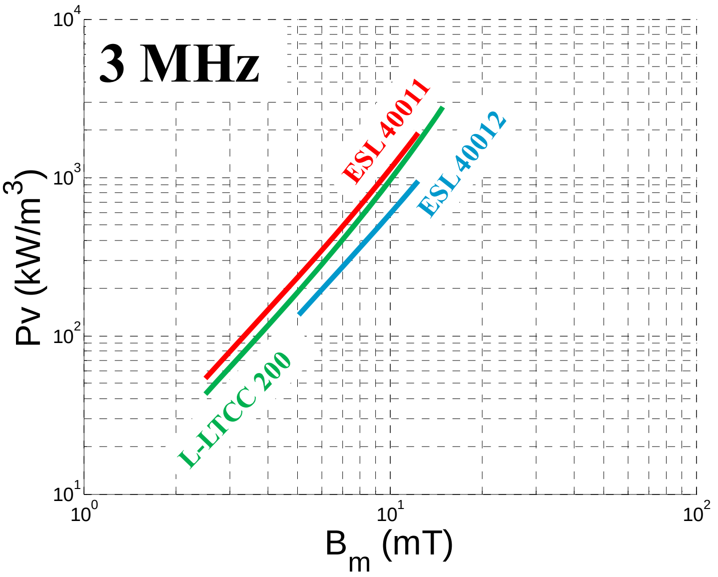

(b) Core loss at 3 MHz

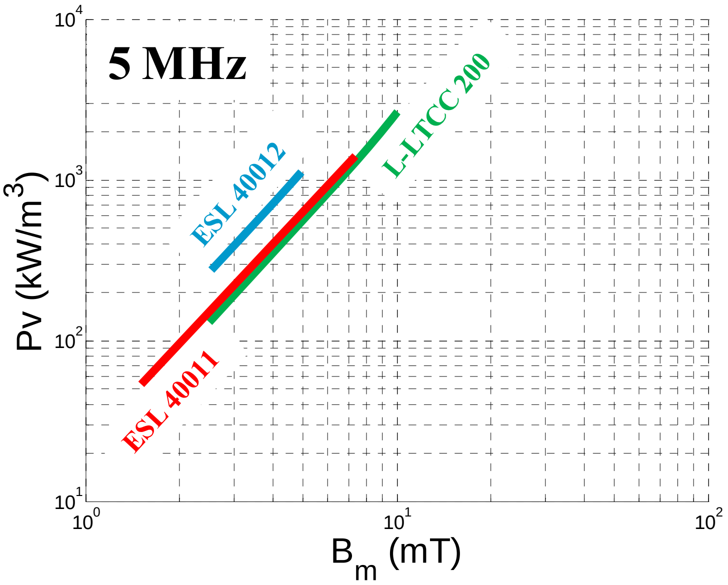

(c) Core loss at 5 MHz

Figure 5.21 Core loss density of laminated LTCC

(1 layer LTCC 40011 and 1 layer LTCC 40012)

5.3.5 L-LTCC 90 (1 layer LTCC 40010 and 1 layer LTCC 40011)

L-LTCC 90 is the combination of LTCC 40010 and 40011 at a ratio of 1:1. It has a higher initial permeability than L-LTCC 80, but the permeability drops faster than that of L-LTCC 80 as the bias increases. Its core loss isn't much better than that of L-LTCC 80. According to the characterizations of these materials, different materials can be chosen for different applications. For high-current POL converters, L-LTCC 80 is the best material among these laminated materials.

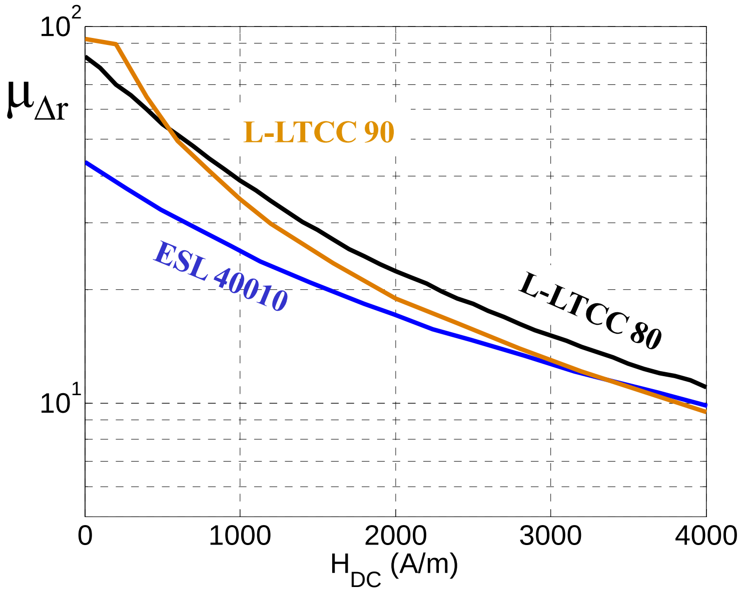

Figure 5.22 Permeability of laminated LTCC

(1 layer LTCC 40010 and 1 layer LTCC 40011)

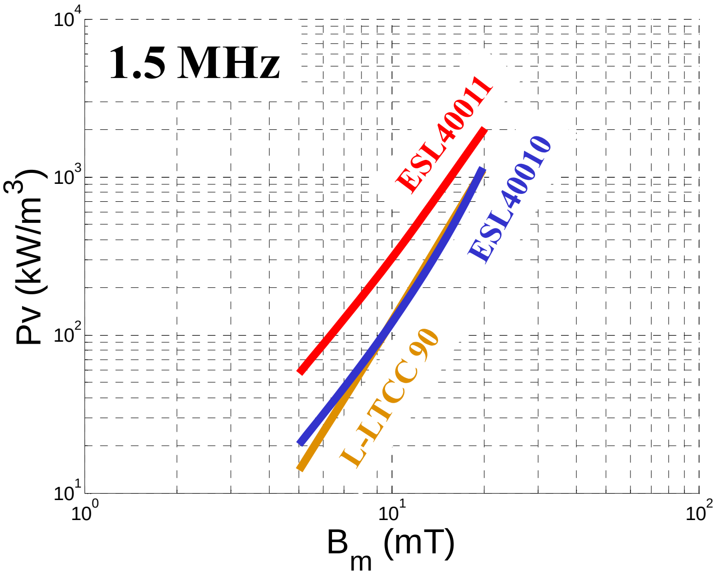

(a) Core loss at 1.5 MHz

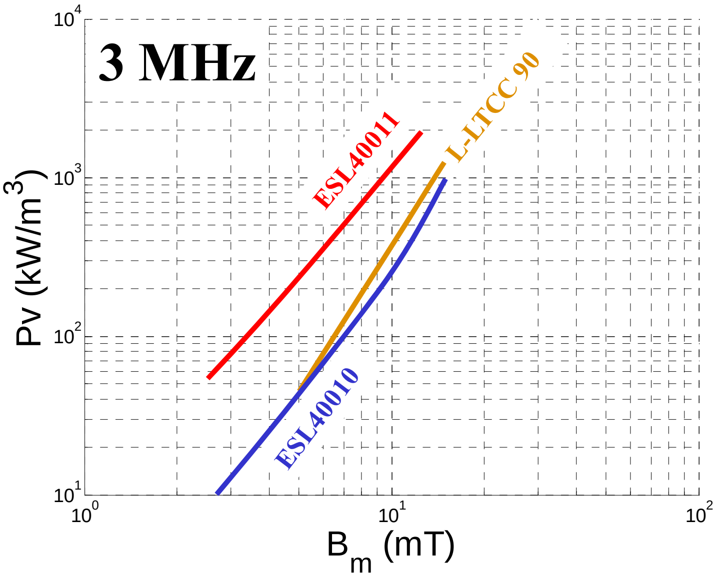

(b) Core loss at 3 MHz

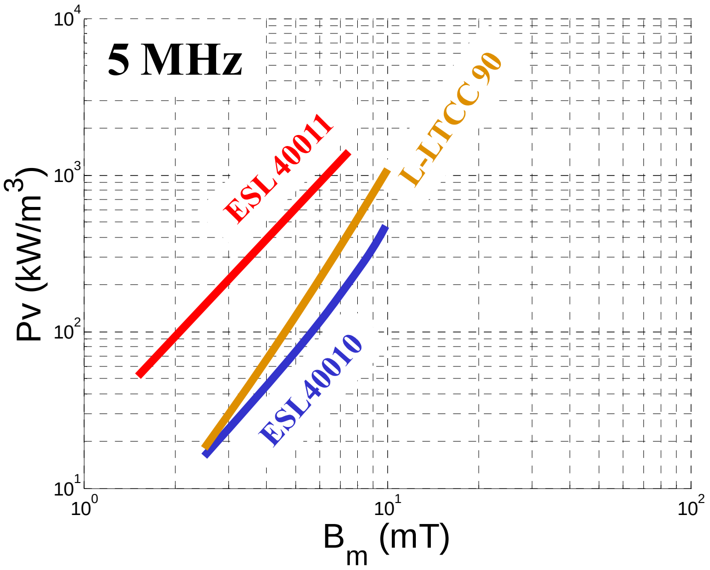

(c) Core loss at 5 MHz

Figure 5.23 Core loss density of laminated LTCC

(1 layer LTCC 40010 and 1 layer LTCC 40011)

The point of laminating LTCC materials is to optimize the composition of the LTCC to achieve the desired permeability in the working conditions for a given application. Experimental characterization shows that this lamination does increase the permeability, and the core loss doesn't increase much more than the LTCC 40010 material. Material L-LTCC 80 appears to be a better material than the commercial LTCC ferrites.

5.4 3D Integrated Point-of-Load Converter using Laminated LTCC Magnetic Substrate

To demonstrate the benefits of the new laminated LTCC material, a 3D integrated converter is built to illustrate its advantages over commercial LTCC ferrite ESL 40010.

As shown in Fig. 5.24, the active layer is built with IR's gallium nitride switch pair. The drivers are in the same package with the GaN die. The input and output capacitors are also mounted on the active layer. Below the active layer is the LTCC magnetic substrate. A lateral flux planar inductor is built on this layer. Two turns are used to provide enough inductance at full load.

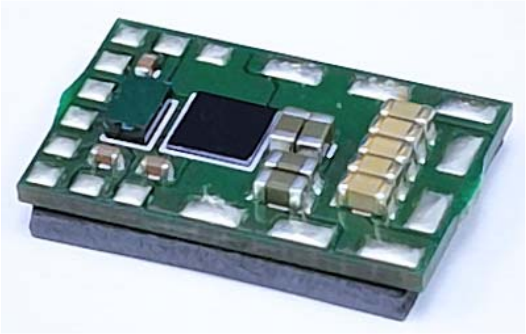

Figure 5.24 3D integrated converter with GaN active layer and LTCC substrate

The switching frequency of the 3D integrated converter is designed to be 2MHz, with 12V input voltage and 1.2V output. The maximum output current is 10A. To make a parallel comparison, inductors are fabricated made of both the new material and the commercial material. Two comparisons are made. The first comparison is to show the higher permeability of the new material. To this end, two identically sized inductors are sintered, as shown in Fig. 5.25. The inductor on the left is made of ESL 40010, while the inductor on the right is made of L-LTCC 80. The designed dimensions and number of turns are the same.

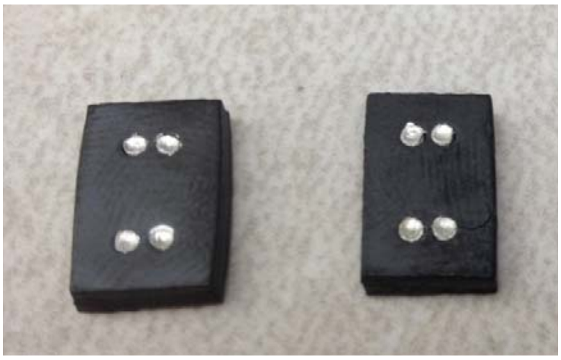

Figure 5.25 Two-turn planar inductors made of ESL LTCC 40010 (left) and L-LTCC 80 (right) with the same thickness (h=2.3mm)

Due to its higher permeability, L-LTCC 80 has a higher inductance over the entire load range. Its inductance is 50% higher under a 10A load, and about 80% higher under a lighter load. Keeping the active layer the same, due to the high inductance, the efficiency of the converter built with L-LTCC 80 is higher than the one with LTCC 50. This is because its smaller current ripple can reduce the switches' turn-off loss, which is a major contributor to the converter's total loss. From the inductance and efficiency test, we can see that L-LTCC 80 can increase the converter efficiency by 0.7% without compromising volume.

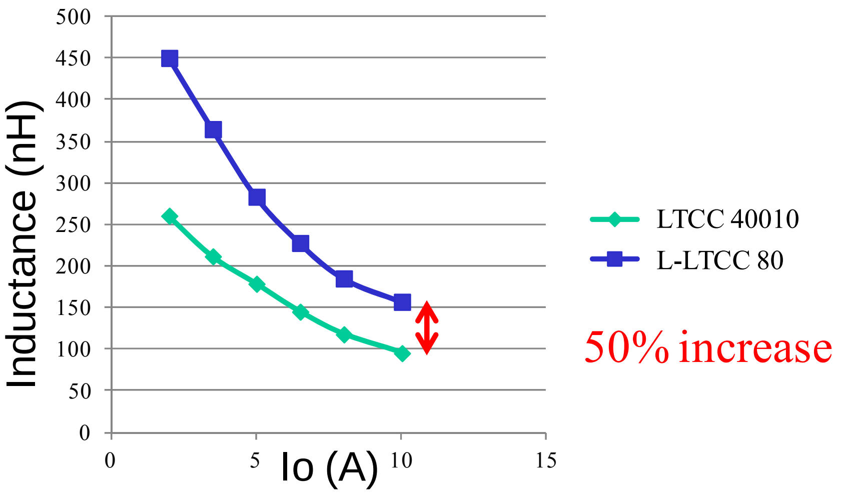

Figure 5.26 Inductance comparison of L-LTCC 80 and LTCC 40010

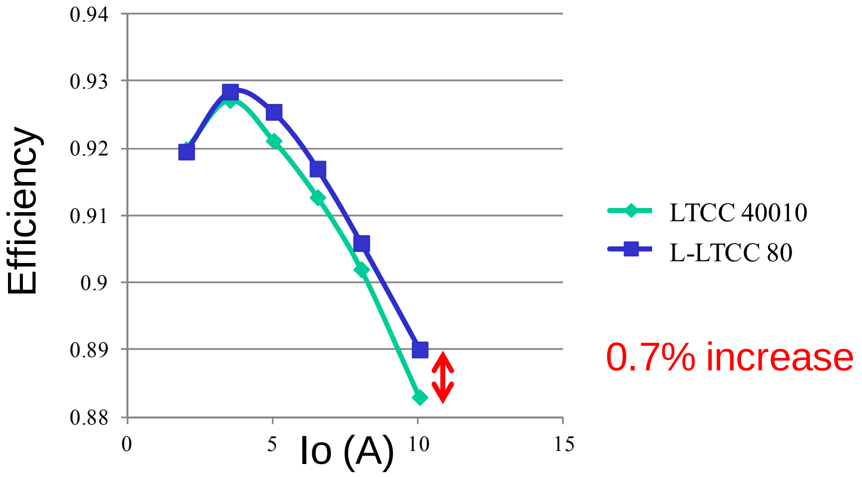

Figure 5.27 Efficiency comparison

The second group of inductors is built to compare the volume-saving capability of the new material. A thinner L-LTCC 80 inductor is made, which has the same full-load inductance as that of the ESL LTCC 40010 inductor. Their footprints are the same, while the L-LTCC 80 inductor is 30% thinner. Both inductors are tested with a GaN active layer. Their full-load inductances are the same, and L-LTCC 80's light-load inductance is even higher than that of ESL LTCC 40010. The efficiency test shows that under a light load, ESL's inductor has lower loss. It makes sense that with smaller volume, the L-LTCC 80 inductor's core loss will be higher. Under a heavy load, L-LTCC 80's efficiency is better. This is because its DCR is lower, due to a thinner inductor thickness. The metal via made with silver paste has a much higher resistivity than the copper via in ESL LTCC 40010. Thus the winding loss is considerably affected by the metal via's thickness. The L-LTCC 80's inductor is 30% thinner than the ESL's, so its DCR is noticeably lower.

According to this comparison, we can see the new material can save 30% of the inductor thickness while maintaining similar or even better efficiency.

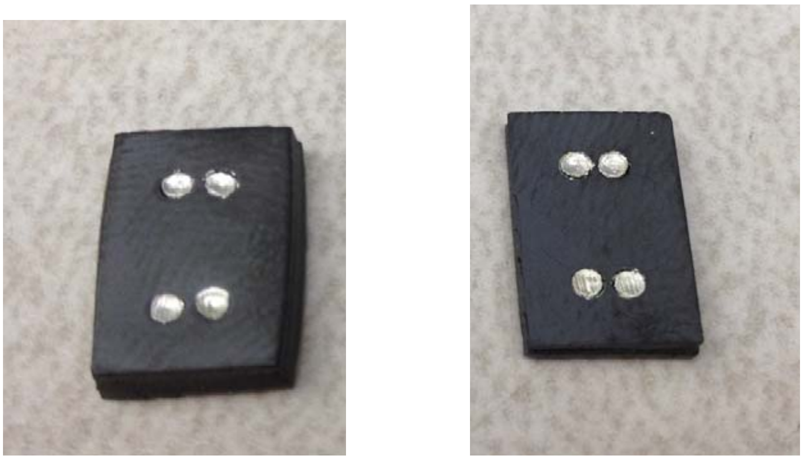

Figure 5.28 Planar inductors made of ESL LTCC 40010 (left) and L-LTCC 80 (right) (ESL 40010, h=2.3mm; L-LTCC 80, h=1.65mm)

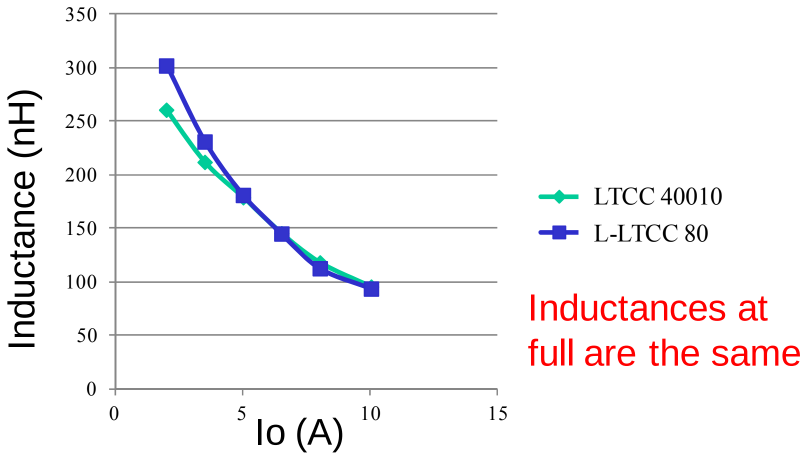

Figure 5.29 Inductance comparison

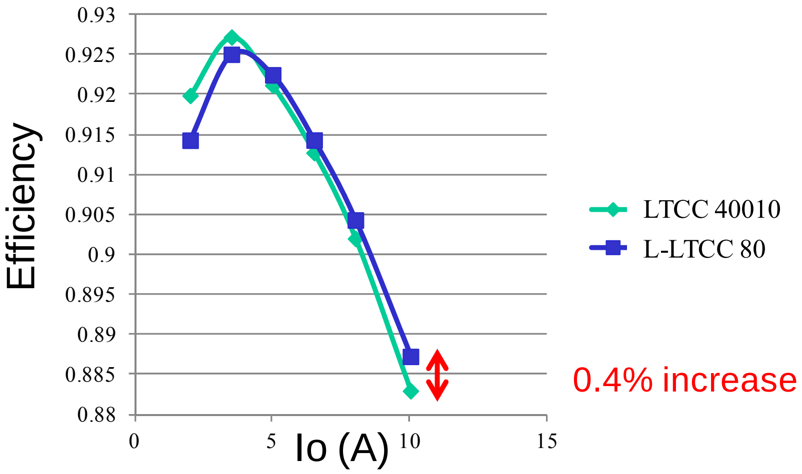

Figure 5.30 Efficiency comparison

In conclusion, the new laminated material L-LTCC 80 has better performance than the commercial LTCCs for 3D integrated power converters. It also shows that magnetic materials should be optimized for specific applications.

Chapter Six Finite Element Analysis of Inductor Core Loss under DC Bias Conditions

Finite element method is a popular way to analyze the magnetic core loss in complex core structures. However, accurate calculation of the inductor core loss under DC bias condition is still a challenge because the magnetic properties like permeability and core loss density will change when a DC pre-magnetization is present, especially for saturable core. This chapter proposes a method which can accurately calculate the inductor loss when it works under DC bias current condition. The method utilizes the material model built by curve fitting the measurement data. This model is effective and simple. To prove this approach, planar inductors built with low temperature co-fired ceramic (LTCC) ferrite are simulated and the calculated core losses are experimentally verified.

6.1 Non-uniform Flux Distribution in a Partially Saturated Planar Inductor

Integrated point-of-load (POL) converters are being used at higher frequencies in order to reduce the size of passive components. As the frequency increases and the magnetic core size is reduced, inductor core loss becomes a significant part of the total loss. Under certain conditions, core loss can dominate the total converter efficiency and thermally limit the power density. Accurately modeling the inductor core loss can not only be used to predict efficiency, but can also improve the thermal design and push the magnetic design near its thermal limits to fully utilize the core volume.

The inductors used in POL converters, which are mostly buck converters, will work under different output currents. The DC current changes the inductance and core loss of the inductor, especially for some non-linear integrated inductors [73][75]. The lateral flux planar inductor is shown in Fig. 6.1(a) [75]. This planar inductor is built using a magnetic plate with holes filled with metal and surface connectors. It has a low profile and can achieve high inductance density. Because it is symmetric along the middle line between the two holes, we can cut along this line and analyze only one half of the inductor. The surface winding contributes a negligible amount of flux in the core, so we are ignoring it here.

The simplest low-profile planar inductor is composed of only one magnetic plate and one conducting via in the middle. Unlike conventional ring cores, the area of the plate that the flux flows through is very wide, so the flux density and magnetic field are very non-uniform, as shown in Fig. 6.1(b). When DC current flows through the via, the DC magnetic field near the middle is so strong that the middle part is partially saturated. As a result, the permeability near the middle is lower due to saturation, and the core loss density also varies for different locations in the core, because the core loss density changes with DC pre-magnetization conditions. The core loss can increase several fold if the DC bias is pushed close to saturation. To calculate the core loss in this kind of nonlinear inductor, we should model the complete material characterization under a wide DC bias range.

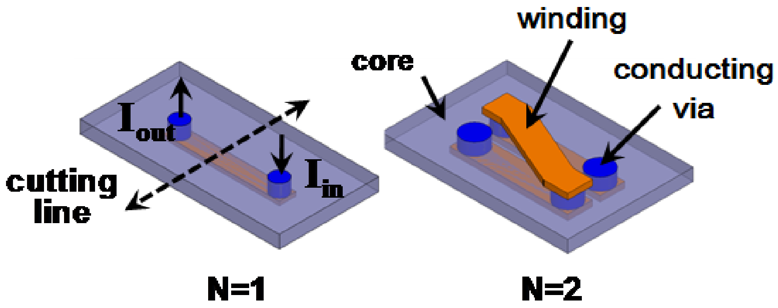

(a) Planar inductor substrate (N = number of turns)

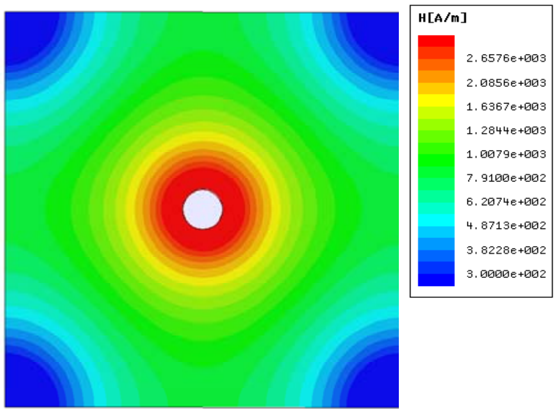

(b) Unit cell and simulated field distribution (top view)

Figure 6.1 Low-profile magnetic substrate structure

According to the modeling works and the characterization of LTCC materials in Chapter four and five, this chapter uses the curve-fitting method to model the core loss under DC bias.

For a complicated structure like the low-profile planar inductor, the flux and magnetic field are not uniformly distributed. An analytical method that approximates the planar inductor as a set of ring cores may be used to calculate the core loss, as shown in Fig. 6.2.[77] The DC bias and AC flux density are assumed to be uniform in each thin toroid or ellipse ring. At low DC current conditions, this approximation may hold, because the inner part around the via is weakly biased, and most of the AC flux still crowds around the via. This approximation is acceptable, because the flux pattern near the via is still in a round shape. However, at high DC currents, the middle part of the core is highly saturated, and the AC flux tends to be pushed outside. The flux pattern changes significantly and can't be regarded as a set of ring cores, as described in Section III. Other than shape approximation, finite element (FE) analysis is an effective and popular solution [60][61][62][63][64][65]. Thus this chapter uses finite element analysis to calculate the inductor loss.

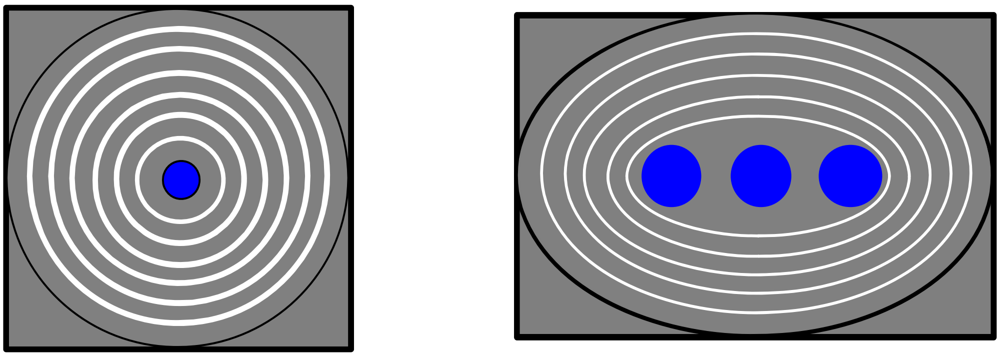

(a) Unit cell

(b) Multi-turn structure

Figure 6.2 Shape approximation for low-profile planar inductor

In the following section, the permeability and core loss density of one type of low-temperature co-fired ceramic (LTCC) ferrite material are modeled. In Section 6.3, the FE simulation and post-simulation process is introduced, and the flux and core loss distribution of planar inductor is discussed. Section 6.4 shows the experimental verification of the proposed approach.

6.2 Curve-fitted LTCC Model

As an example, low-profile planar inductors made of LTCC ferrite 40011 from ESL Science Lab® are investigated. The fabrication process used is that introduced in Chapter five. To accurately calculate the core loss of the inductor, the precise material model must be built first.

Because the permeability varies with AC excitation level, to make sure the tested data is valid for further analysis, the magnitude of AC flux density is kept around 7.5mT in the incremental permeability test. For ferrite materials, temperature has a strong impact on permeability and core loss. To keep the result consistent, all of the characterization and verification are performed at temperatures under 100°C.

As shown in Fig. 6.3, the relative incremental permeability drops exponentially with the DC bias field, and it is modeled by the equation below. The H_{dc} is the bias field strength in amperes per meter.

$$\mu_{\Delta r} = 121.6e^{-5.2\times 10^{-3} H_{dc}} + 70.29e^{-1.06\times 10^{-3} H_{dc}} \quad (0 \le H_{dc} \le 4000 A/m) \tag{6.1}$$

The core loss without DC bias is modeled by the Steinmetz equation, shown in (6.2). Since the frequency here is fixed, the Steinmetz equation has only one variable; the magnitude of AC flux density B_m. B_m is measured in millitesla, and P_v is in kilowatts per cubic meter.

$$P_{v0}(B_m) = 0.7146 \times B_m^{2.652} \tag{6.2}$$

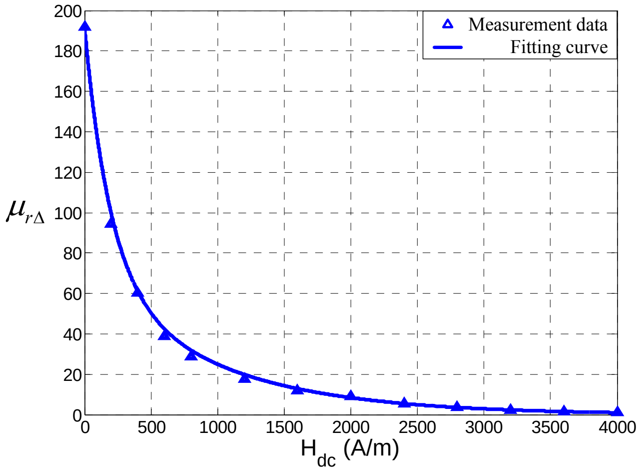

Figure 6.3 LTCC 40011 relative incremental permeability with

H$_{dc}$

(1.5MHz, 100°C, Bm~7.5mT,)

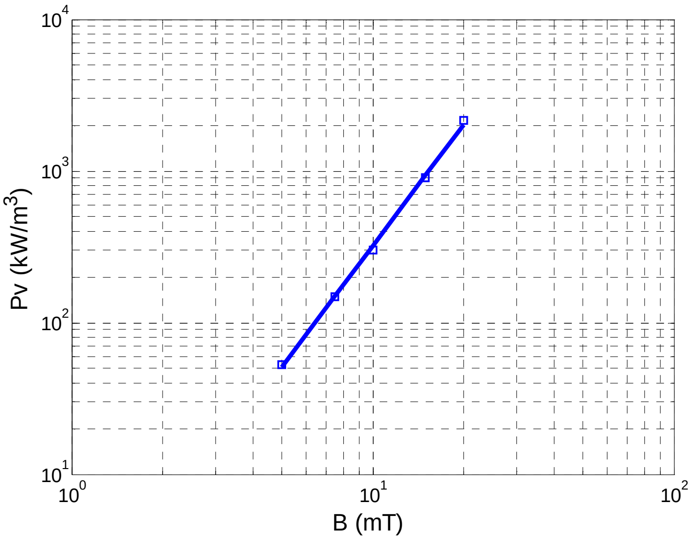

Figure 6.4 LTCC 40011 core loss density vs. AC flux density

(1.5MHz, 100°C)

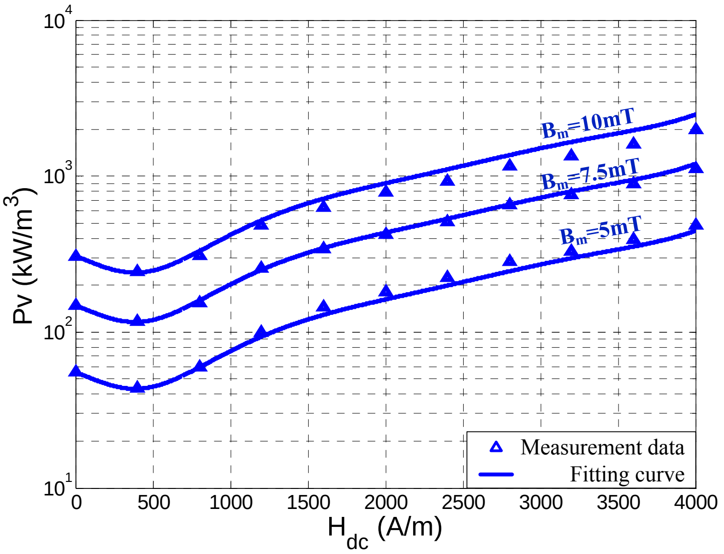

Figure 6.5 LTCC 40011 core loss density as a function of H_{dc}

(1.5MHz, 100°C)

The impact of the DC bias on core loss is shown in Fig. 6.5. The core loss model with DC bias can be modeled as the product of the zero-bias core loss density and the bias factor.

$$P_v = P_{v0} \times F_{dc} \tag{6.3}$$

Function F is the bias factor in (6.3). From the measured data points, we can see that for different DC biases, the spacing between three measurement points of 5mT, 7.5mT and 10mT are almost constant, which means we can assume that the factor F is only affected by H_{dc}. So the core loss density without DC bias is determined by B_m; the bias factor is determined by H_{dc}. Now we have decoupled the effects of B_m and H_{dc}, and they separately affect the final core loss density. From the measurement results, we know the factor function F is not a simple linear or exponential function, so it is curve-fitted as a polynomial form.

$$P_v(B_m, H_{dc}) = P_{v0}(B_m) \times F(H_{dc}) \tag{6.4}$$

$$\begin{aligned} F(H_{dc}) &= aH_{dc}^7 + bH_{dc}^6 + cH_{dc}^5 \\ &\quad + dH_{dc}^4 + eH_{dc}^3 + fH_{dc}^2 + gH_{dc} + 1 \end{aligned} \qquad (0 \le H_{dc} \le 4000 A/m) \tag{6.5}$$

where,

$$\begin{aligned} a &= 2.782 \times 10^{-23} \\ b &= -3.667 \times 10^{-19} \\ c &= 1.861 \times 10^{-15} \\ d &= -4.45 \times 10^{-12} \\ e &= 4.65 \times 10^{-9} \\ f &= -5.24 \times 10^{-7} \\ g &= -8.39 \times 10^{-4} \end{aligned}$$

Compared with the DC factor model discussed in [32]and[64], this model has several advantages. First, it decouples the impact of the AC and DC components on the core loss. From the measurement results, it is apparent that AC flux doesn't have much of an effect on the core loss factor. Similar phenomena can be observed in the data measured in [32][34].

Second, the core loss under bias is modeled with the DC bias field, instead of DC flux. The reason is explained in Chapter four.

Third, a polynomial form can accommodate different core loss behaviors under DC bias better. Sometimes core loss is not simply an increasing function of DC bias. The core loss under DC bias is a complex mechanism, and core loss may reach its minimum at a certain bias value. According to [35], this phenomenon may be explained as an eddy-current-dominant case. The eddy current loss drops first, and then rises quickly with DC bias. Thus if eddy current loss is the major part of the total core loss, the core loss will experience this phenomenon. As a conclusion, a simple exponential or square root form can't model the complexity of the DC bias impact.

The impact of temperature is not included in this model. The core loss varies with temperature, especially when using ferrites. Generally, ferrites have the lowest core loss within the temperature range of 60°C to 90°C. The impact of temperature can also be modeled as a factor multiplied using the Steinmetz equation.[14][79] It may be reasonable to multiply the temperature factor by the DC bias factor to describe the core loss change at a certain bias and temperature, but whether the DC bias factor can be decoupled with temperature factor has not been investigated in this dissertation. Thus the analysis is performed at a single temperature in this paper.

Now the permeability and core-loss curves are fitted as the functions of B_m and H_{dc}, so we only need to know the B_m and H_{dc} of the core structure to calculate the core loss density.

6.3 Core Loss Calculation with Finite Element Tool

Finite element analysis is used to simulate the AC flux density and DC magnetic field in each element for the planar inductor in Fig. 6.1. ANSYS Multiphysics® is used in this FE simulation. A transient simulation is performed, because the transient solver can support a non-linear B-H curve and the eddy current effect in the conductor. The non-linear B-H curve used in the simulator is derived by integrating the incremental permeability in Fig. 6.3. Though this may not be the real static B-H curve because it is obtained from dynamic measurement results [78], it can still be used in this simulation because the accuracy of the DC flux is not necessary in this core loss calculation, and only B_{ac} and H_{dc} are required for the core-loss model. The limitations of this approach are discussed in the last section of this chapter.

The excitation used in the simulation is a current source with two components: the DC current bias and the AC current ripple. The reason to choose the current-driven simulation is its ease of verification. Because the inductor used in the test will have lead inductance, which is comparable to the inductance contributed by the core, the measured voltage will include the lead inductor voltage, which is difficult to accurately compensate for some cases (such as the three-turn case). Measuring the current is much easier and more reliable. However, the voltage-driven simulation should be as valid as the current-driven simulation demonstrated in this example.

Before running the simulation, the inductor structure is built in ANSYS, and the material characteristics are assigned for each part of the inductor, including the nonlinear B-H curve for the core material. After meshing the structure, the transient simulation is run for several periods. The excitation waveform is illustrated in Fig. 6.6, and the AC ripple's frequency is 1.5MHz. The simulator will iterate for each element at each time step until convergence. The flux density and field strength for each element are recorded at each time step. After the solution is found, the post-simulation process is begun.

At T_m, the current reaches the maximum value, so the magnetic flux density and field strength also reach their maximum values. Likewise, at T_n, the current reaches its minimum value, so the magnetic flux density and field strength also reach their minimum values. Measuring the B and H values in each element at these two moments, we find that the difference between $B(T_m)$ and $B(T_n)$ is the AC fluctuation of the flux density in each element. The average of $H(T_m)$ and $H(T_n)$ is regarded as the DC magnetic field strength H_{dc}. The H_{dc} and B_m in the plate can be plotted using the B_m and H_{dc} values in each element, as shown in Fig. 6.8 and Fig. 6.9. With the B_m and H_{dc} value, we can calculate the core loss in each element by plugging the simulated B_m and H_{dc} into the material's loss density in (6.2), (6.4), and (6.5), and multiplying the core loss by the element volume. The core loss density is plotted in Fig. 6.10. Summing up the loss in all elements, we can calculate the total loss in the core volume.

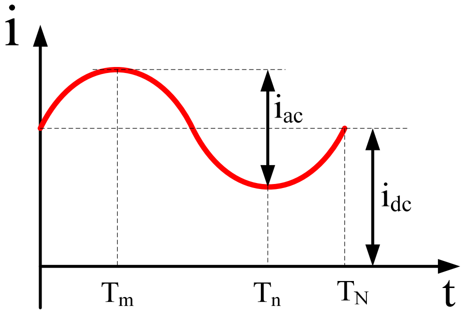

Figure 6.6 Current excitation in the via conductor

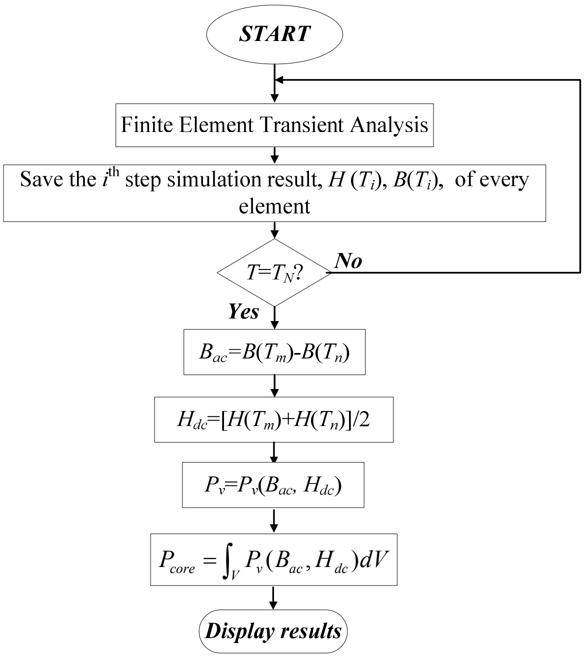

Figure 6.7 Core loss calculation flow chart

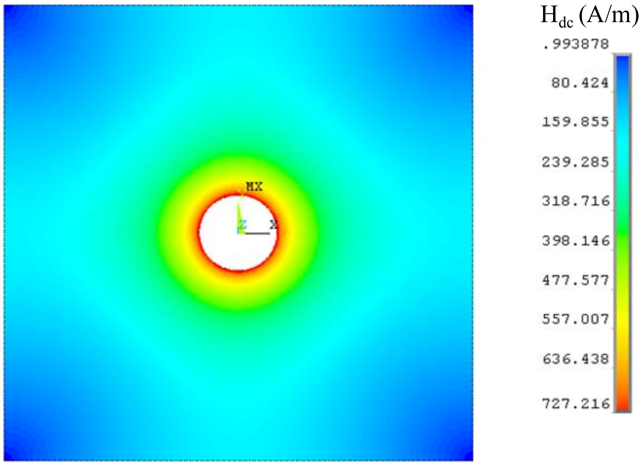

Figure 6.8 Simulated DC magnetic field H_{dc} (I_{dc}=3A)

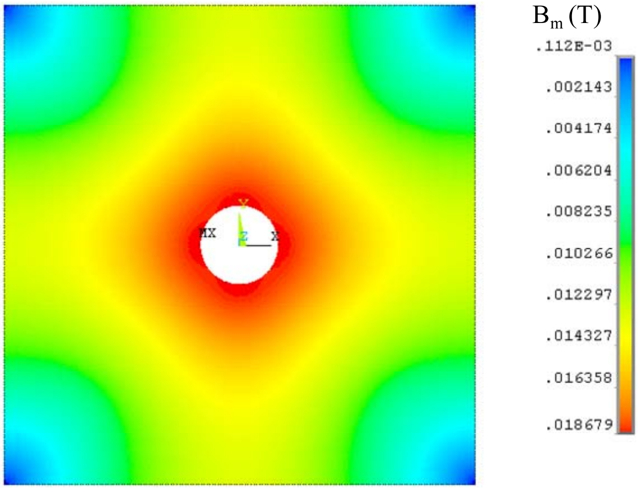

Figure 6.9 Simulated AC flux density magnitude B_m (I_{dc}=3A)

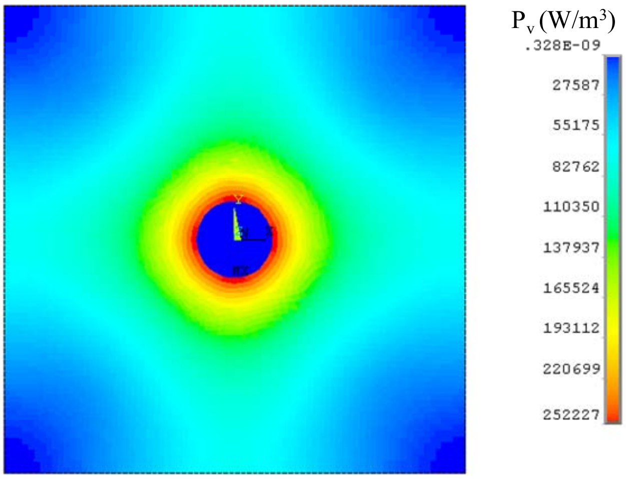

Figure 6.10 Core loss density in the unit cell (I_{dc}=3A)

From the simulated flux and core loss distribution, we can see that when the DC current is at a low level, the core near the middle via is less saturated. Most of the AC flux is still crowded around the via, as is the core loss density. The flux density and core loss density distribution are still round, so it is reasonable to assume that the core can be modeled as a set of toroid cores.

However, as the DC current rises, for example to 10A, the middle part is highly saturated, and the permeability drops significantly. As a result, the AC flux is pushed far away from the middle, because the outer part has higher permeability even thought their magnetic path length is larger, as shown in Fig. 6.11. The AC flux distribution can no longer be approximated as a round shape, but is more like a cross, as is the core loss density distribution, shown in Fig. 6.13. The core loss density is determined by both the AC flux and DC bias field. The middle part near the via has higher bias, but the AC flux density is low. The outer part near the edge has higher AC flux density, but the DC bias is low. The highest core loss density occurs somewhere between the inner and outer part, which is the hot spot in the core. From the simulation result, we can found that the DC bias level can shift the hot spot in the core. As DC current increases, the location of the greatest core loss moves from around the via to the outside, which is an interesting observation from this simulation.

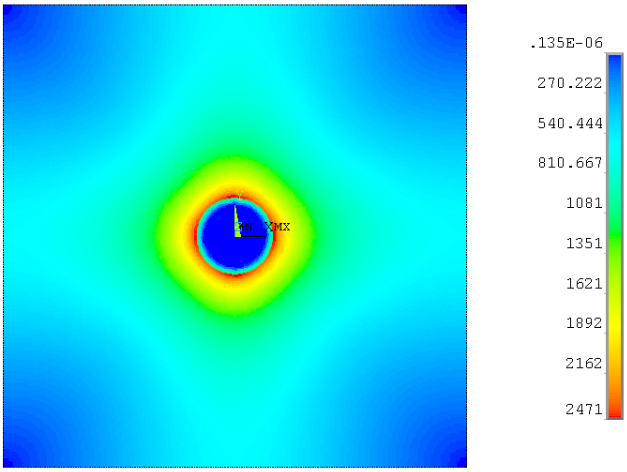

Figure 6.11 Simulated DC magnetic field H_{dc} (I_{dc}=10A)

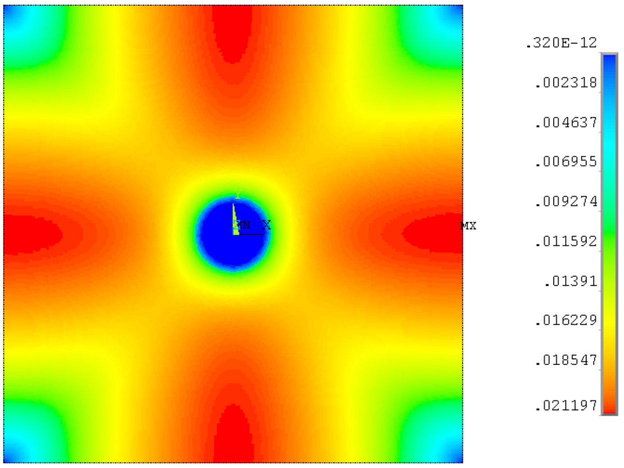

Figure 6.12 Simulated AC flux density magnitude B_m (I_{dc}=10A)

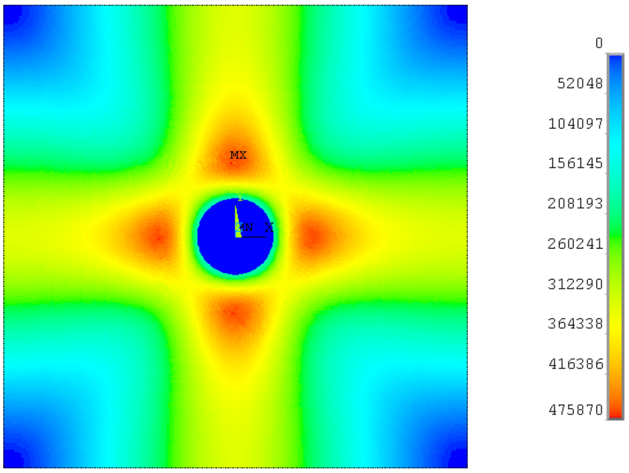

Figure 6.13 Core loss density in the unit cell (I_{dc}=10A)

The same simulation can be performed on a multi-turn structure, where a similar cross-like flux distribution and core loss density distribution can be observed.

6.4 Experimental Verification

6.4.1 Verification on Unit Cell of Planar Inductor

To validate the calculation method using the finite element simulation in the previous section, the results are experimentally verified. The measurement circuit used for verification is shown in Fig. 6.14, and the setup is shown in Fig. 6.15. The measurement principle and setup details are discussed in Chapter three.

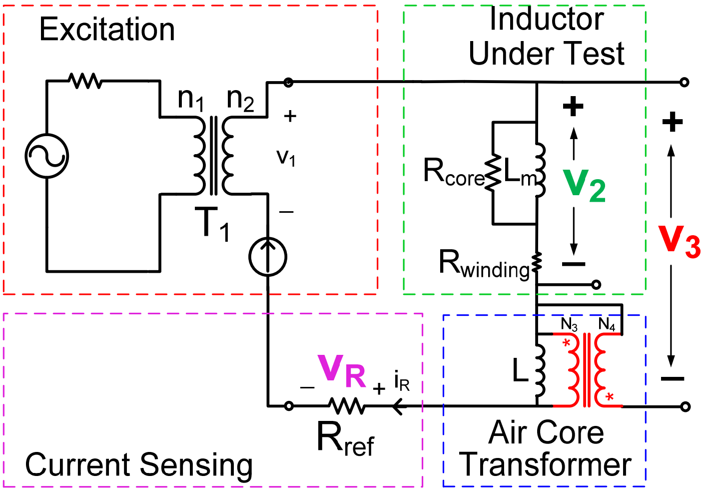

Figure 6.14 Inductor loss measurement circuit

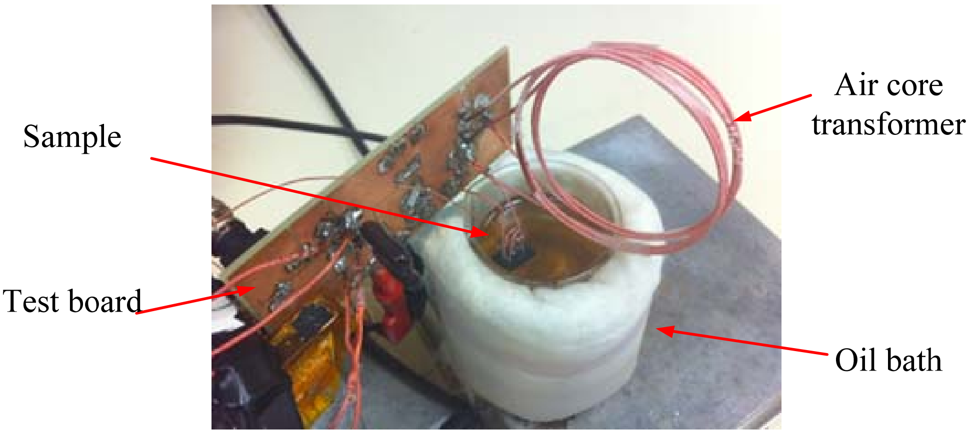

Figure 6.15 Inductor loss measurement setup

The first step of verification is to compare the calculated results of a unit cell with experimental results. The dimensions and a photo of the sample unit cell made of LTCC 40011 are shown in Fig. 6.16. The inductor loss is measured at 1.5MHz and 100°C.

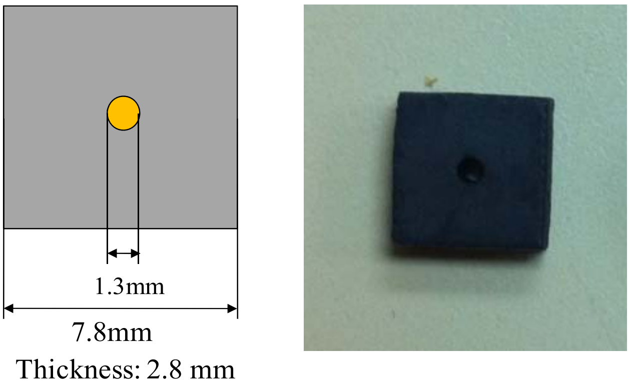

(a) Unit cell dimensions

(b) Fabricated unit cell

Figure 6.16 Unit cell used for verification

The winding used in the unit cell inductor is Litz wire, because of its low AC resistance and easier winding loss compensation. Once the current through the winding is measured, it is easy to calculate the winding loss of the Litz wire and estimate the core loss by subtracting the winding loss from the measured total loss. The process for measuring the inductor core loss is:

(1) Measure the AC winding resistance of the Litz wire at the given frequency using an impedance analyzer.

(2) Measure the total loss of the inductor under certain current conditions.

(3) Calculate the winding loss under each of the current conditions.

(4) Subtract the winding loss from the total loss.

Finally, the core loss of the unit cell structures can be measured.

The calculation and measurement results of the unit cell are displayed in Table 6.1. The calculation results match the measurement very well for both the case with no DC

Table 6. 1 Calculation and measurement results for unit cells

Excitation	**Measurement**	**Calculation**	**Error**
I_{dc}=0A, I_{ac}=0.4A	4.77mW	4.23mW	-11.3%
I_{dc}=0A, I_{ac}=0.6A	12.73mW	12.4mW	-2.6%
I_{dc}=0A, I_{ac}=0.8A	26.85mW	26.6mW	-0.93%
I_{dc}=3A, I_{ac}=0.8A	1.9mW	1.7mW	-10.5%
I_{dc}=3A, I_{ac}=1.6A	11.5mW	11.1mW	-3.5%
I_{dc}=3A, I_{ac}=2.4A	35.7mW	33.2mW	-7%

current and the case with DC current. The maximum error is below 10%. The error is larger at a low AC excitation level. This may be explained by measurement error, because the loss is too small and the waveform measured by the probe is vulnerable to noise. Another thing which may need to be explained is that the core loss with DC bias is much lower than AC bias even with the same AC current. This is because the permeability drops significantly with the DC bias. Hence the AC flux density will be much lower when the AC current is the same, and the core loss is also much lower.

6.4.2 Verification on Three-turn Planar Inductor

To further verify the model, a more complicated planar inductor with three turns is investigated. The dimensions of the inductor are shown in Fig. 6.17. The winding of the inductor is also Litz wire, and the core loss measurement process is the same as that for the unit cell. The calculation and measurement results are shown in Table 6.2.

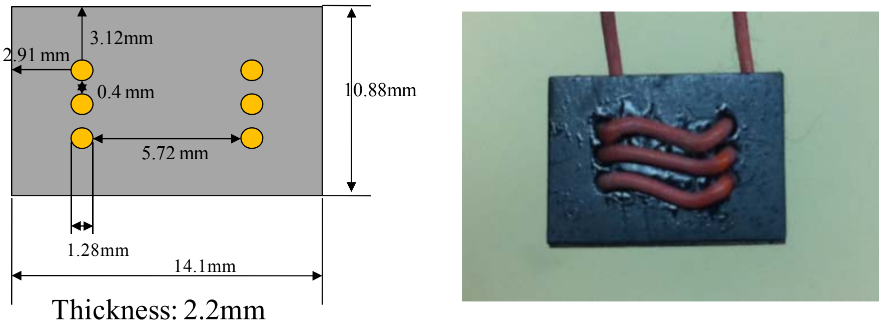

(a) Dimensions (b) Inductor with Litz wire

Figure 6.17 Three-turn planar inductor used for verification

Table 6. 2 Calculation and measurement results for three-turn inductor

Excitation	**Measurement**	**Calculation**	**Error**	**Calculation $D(H_{dc})=1$**	**Error $D(H_{dc})=1$**
I_{dc}=0A, I_{ac}=0.2A	8.68mW	7.57mW	-11.3%	-	-
I_{dc}=0A, I_{ac}=0.4A	44.34mW	47.6mW	2.6%	-	-
I_{dc}=0A, I_{ac}=0.6A	130.4mW	139mW	0.93%	-	-
I_{dc}=3A, I_{ac}=0.6A	3.13mW	2.71mW	-10.5%	2.88mW	-8%
I_{dc}=3A, I_{ac}=1.2A	16.6mW	17.4mW	3.5%	21.8mW	31.3%
I_{dc}=3A, I_{ac}=1.8A	47.6mW	52.4mW	7%	55.7mW	17%
I_{dc}=10A, I_{ac}=2A	3.96mW	3.59mW	-9.3%	1.77mW	-55.3%
I_{dc}=10A, I_{ac}=4A	22.5mW	23.8mW	5.8%	11.6mW	-48.5%
I_{dc}=10A, I_{ac}=6A	71.8mW	76.4mW	6.4%	36.6mW	-49%

The results in Table 6.2 show that the calculation agrees with the experiment for both the biased and non-biased cases. The table also lists the core loss calculation results without considering the DC bias factor, which is often assumed in practice. At low-bias conditions, the calculation is close to the test result, but with higher discrepancy than the result considering the DC factor. At high-bias conditions, this approximation has much more error. The actual core loss can be twice the calculated loss if the DC bias impact is neglected.

After the experimental verification, the accuracy of this core loss calculation method with finite element analysis is proven.

6.5 Conclusion and Discussion

This chapter proposes a finite element analysis approach to calculate the magnetic core loss in a planar inductor when a DC current is present. Though only the low-profile planar inductor built with LTCC, which is a thick film technology, is simulated and discussed, other kinds of inductors made of different magnetic materials can be analyzed in the same way. For the thin film inductors used in the power supply on the chip, the core loss and permeability can also be characterized using the test setup introduced in this dissertation. Once the characterization is finished, the analysis can follow the approach demonstrated in this chapter.

Experimental verification shows that the proposed approach has good accuracy. The core loss density can be predicted, which is very helpful to determining the hot spot in a complicated core structure. Even though this approach requires some effort to measure the core loss under biased conditions, the core-loss modeling is straightforward and accurate. The combination of a curve-fitting model and the finite element method enables core loss calculation in complicated structures. This core loss simulation can be possibly combined with thermal simulation to predict the thermal distribution inside of the core.

However, the method of analysis in this chapter has limitations. The major drawback is the dynamically derived B-H curve. It is not a real B-H curve, because it only represents the information of incremental permeability, not the amplitude permeability. It works for inductance and core loss calculation of non-gapped inductors. However, for gapped inductors, the simulated H_{dc} won't be the actual DC bias field strength, and neither the calculated loss nor the calculated inductance will be accurate. One possible solution to this problem is to plot two B-H curves. One is a dynamically derived B-H curve; the other is a static B-H curve. First the H_{dc} is simulated using the static B-H curve to determine the DC working condition in gapped core. Then the dynamic B-H curve can be used to get the incremental permeability and the AC flux density at each element. This approach is much more complicated than the method demonstrated above, and its exploration can be the future extension of the work in this chapter.

Chapter Seven Conclusions and Future Work

7.1 Conclusions

In the dissertation, two new core loss measurement methods are introduced in Chapter two and Chapter three. These two methods use the same reactive cancellation concept to reduce the sensitivity to phase error, which was the most critical error in classic two-winding method at high frequency. By using the new methods, the accuracy can be improved by several orders. The first method is for sinusoidal, and the second is for non-sinusoidal. The new techniques enable high frequency core loss characterization capability, which will help scientists and engineers on material research and inductor/transformer design. The details are discussed, which is critical to the measurement accuracy.

With the measurement techniques, the core loss under AC rectangular voltage and DC bias current are investigated in Chapter four. A new core loss model named rectangular extension of Steinmetz equation (RESE) is proposed base on the measurement results. The new model is shown to be more accurate than the existing core loss models. Several commercially available MnZn ferrites are characterized and modeled.

Chapter five shows the characteristics of three commercial LTCC materials, which is the first complete magnetic characterization of these materials for power electronics applications. Based on characterized properties of ESL LTCC ferrites, a group of new LTCC ferrites are fabricated and tested. The new LTCC is made by laminating commercial LTCC tapes and co-firing. The laminated LTCC is demonstrated to have over 50% more inductance over the commercial LTCC materials. This work indicates that the power electronics engineers should work with material engineers to get the optimum material for a given application.

In Chapter six, the core loss of partially saturated lateral flux planar inductor is analyzed. The challenge of the analysis is the complexity of the distribution of bias field and flux density in a highly biased lateral flux inductor. Each point in the core is working at different excitation and bias condition, and the core loss density is very non-uniform. The proposed method combines the characterization tested in previous chapters and the commercial finite element tool. The calculation results are verified by experiments.

In conclusion, the research in this dissertation proposed a complete solution to measure, model and analyze the high frequency core loss. This solution will not only help fundamental research on physics understanding and material innovation, but also development of power electronics and RF applications.

7.2 Future Work

Though this dissertation has proposed a complete solution for core loss characterization, modeling and analysis, there are still some future work can be extended on the following directions:

1. The core loss measurement setup can be improved. For the capacitive cancellation method, the resonant capacitor needs to be tuned to work properly. Changing the capacitor needs certain labor and makes the setup not completely

automatic. An auto tunable capacitor with high quality factor should be designed to build an automatic measurement instrument.

2. For the inductive cancellation method, the parasitic capacitor on the transformer should be further controlled, in order to extend the measurable frequency to over 5MHz. Furthermore, the adjustable transformer can be further improved.
3. A more general core loss model can be developed based on the work in this dissertation. More materials can be characterized, and some modifications could be added to the proposed model, to make it match other materials and other waveforms better. Furthermore, a material core loss database can be built to facilitate the design of power transformers and inductors.
4. The finite element core loss analysis method can be improved for gapped inductor. The method proposed here is limited to non-gapped case. The possible solution for gapped core is discussed in Chapter six.

Reference

[1] Wenjian Gu and Rui Liu, “A Study of Volume and Weight vs. Frequency for High-Frequency Transformers”, Power Electronics Specialists Conference, 1993. PESC '93 Record., 24th Annual IEEE， pg. 1123-1129.

[2] Odendaal, W.G.; Ferreira, J.A.; , "Effects of scaling high-frequency transformer parameters," *Industry Applications, IEEE Transactions on* , vol.35, no.4, pp.932-940, Jul/Aug 1999.

[3] David J. Perreault, Jingying Hu, Juan M. Rivas, Yehui Han, Olivia Leitermann, Robert C.N. Pilawa-Podgurski, Anthony Sagneri, Charles R. Sullivan, “Opportunities and Challenges in Very High Frequency Power Conversion”, Applied Power Electronics Conference and Exposition, 2009. APEC 2009. Twenty-Fourth Annual IEEE, pp. 1-14.

[4] Chih-Wen Chen, “Magnetism and Metallurgy of Soft Magnetic Materials”, 1977.

[5] Bertotti, G, “Physical interpretation of eddy current losses in ferromagnetic materials. I. Theoretical considerations”, Journal of Applied Physics, 1985.

[6] Donald S. Gardner, Gerhard Schrom, Fabrice Paillet, Brice Jamieson, Tanay Karnik, and Shekhar Borkar, “Review of On-Chip Inductor Structures With Magnetic Films”, IEEE Transactions on Magnetics, Vol. 45, No. 10, October 2009, pp. 4760-4766.

[7] T. O'Donnell, N. Wang, R. Meere, F. Rhen, S. Roy, D. O'Sullivan, C. O'Mathuna, “Microfabricated Inductors for 20 MHz Dc-Dc Converters”, Applied Power Electronics Conference and Exposition, 2008. APEC 2008. Twenty-Third Annual IEEE, pp. 689-693.

[8] Daniel V. Harburg, Xuehong Yu, Florian Herrault, Christopher G. Levey, Mark G. Allen, and Charles R. Sullivan, “Micro-fabricated thin-film inductors for on-chip power conversion”, Integrated Power Electronics Systems (CIPS), 2012 7th International Conference on, pp. 1-6.

[9] Jeff Sherman, Juan Herbsommer, “Advancing Silicon Performance Beyond the Capabilities of Discrete Power MOSFETs- Combining NexFETTM MOSFETs with stacked die techniques significantly reduceds parasitic losses”, Bodo’s Power Systems, August 2010 .

[10] Parul Dhagat, Satish Prabhakaran, Charles R. Sullivan, “Comparison of Magnetic Materials for V-Groove Inductors in Optimized High-Frequency DC-DC Converters”, IEEE TRANSACTIONS ON MAGNETICS, VOL. 40, NO. 4, JULY 2004, pp. 2008-2010.

[11] Di Yao, Charles R. Sullivan, “Optimization of V-Groove Inductors Using Multilayer Co-Zr-O Thin Films for 10 MHz to 100 MHz DC-DC Converters”, Control and Modeling for Power Electronics (COMPEL), 2010 IEEE 12th Workshop on, pp. 1-5.

[12] Chas P. Steinmetz, “On the law of hysteresis”, Proceedings of IEEE, Vol,72, Issue 2, pp. 197-221, Feb. 1984.

[13] Datasheet of 3F3 MnZn ferrite, Ferroxcube, 2008 Sept. 01.

[14] “Design of Planar Power Transformers”, Ferroxcube application note.

[15] Ray Ridley, Art Nace, “Modeling ferrite core losses”, Switching Power Magazine, vol. 3, no. 1, pp. 6–13, 2002.

[16] Christopher Oliver, “A New Core Loss Model", Switching Power Magazine, Volume 3, Issue 2, 2002.

[17] Dan Chen, “Comparisons of high frequency magnetic core losses under two different driving conditions - A sinusoidal voltage and a square-wave voltage”, Power Electronics Specialists Conference, p. 237-241, 1978.

[18] Chen, D.Y.; , "High-frequency core loss characteristics of amorphous magnetic alloy," Proceedings of the IEEE , vol.69, no.7, pp. 853- 855, July 1981.

[19] Rudy Severns, “HF core losses for non-sinusoidal waveforms”, Proc. HFPC 1991.

[20] Albach, M. Durbaum, T., Brockmeyer, A. , "Calculating core losses in transformers for arbitrary magnetizing currents a comparison of different approaches," Power Electronics Specialists Conference, 1996.

[21] J. Reinert, A. Brockmeyer, R.W. De Doncker, “Calculation of Losses in Ferro- and Ferrimagnetic Materials Based on the Modified Steinmetz Equation”, Industry Applications Conference, 1999. Thirty-Fourth IAS Annual Meeting. Vol. 3, pg. 2087-2092.

[22] Jieli Li, Tarek Abdallah, and Charles R. Sullivan, “Improved Calculation of Core Loss With Nonsinusoidal Waveforms”, IEEE Industry Applications Society Annual Meeting, Oct. 2001, pp. 2203–2210.

[23] Kapil Venkatachalani, Charles R Sullivan.Tarek Abdallah, and H e m h Tacca, “Accurate Prediction of Ferrite Core Loss with Nonsinusoidal Waveforms Using Only Steinmetz Parameters”, 2002 IEEE Workshop on Computers in Power Electronics, 2002, pg. 36-41.

[24] Van den Bossche, A.P.; Van de Sype, D.M.; Valchev, V.C.; , "Ferrite Loss Measurement and Models in Half Bridge and Full Bridge Waveforms," Power Electronics Specialists Conference, 2005. PESC '05. IEEE 36th , vol., no., pp.1535-1539, 16-16 June 2005.

[25] Van den Bossche, A.; Valchev, V.C.; Georgiev, G.B.; , "Measurement and loss model of ferrites with non-sinusoidal waveforms," Power Electronics Specialists Conference, 2004. PESC 04. 2004 IEEE 35th Annual , vol.6, no., pp. 4814- 4818 Vol.6, 20-25 June 2004.

[26] Wei Shen, “Design of High-density Transformers for High-frequency High-power Converters” Virginia Tech dissertation, 2006.

[27] Villar, I.; Viscarret, U.; Etxeberria-Otadui, I.; Rufer, A.; , "Global Loss Evaluation Methods for Nonsinusoidally Fed Medium-Frequency Power Transformers," Industrial Electronics, IEEE Transactions on , vol.56, no.10, pp.4132-4140, Oct. 2009.

[28] Muhlethaler, J.; Biela, J.; Kolar, J.W.; Ecklebe, A.; , "Improved Core-Loss Calculation for Magnetic Components Employed in Power Electronic Systems," Power Electronics, IEEE Transactions on , vol.27, no.2, pp.964-973, Feb. 2012.

[29] Datasheet of 3F45 MnZn ferrite, Ferroxcube, 2008 Sept. 01.

[30] Charles Sullivan, John Harris, Edward Herbert, “ Tesing core loss for rectangular waveforms”, PSMA project report, 2010.

[31] CharlesSullivan,John Harris, “ Testing core loss for rectangular waveforms, phase II”, PSMA project report, 2011.

[32] A. Brockmeyer, “Experimental evaluation of the influence of DC premagnetization on the properties of power electronic ferrites”, in proc. Appl. Power Electron. Conf., vol. 1, 3-7 March 1996, pp. 454 – 460.

[33] J. Mühlethaler, J. Biela, J. W. Kolar, and A. Ecklebe, "Core Losses under DC Bias Condition based on Steinmetz Parameters", International Power Electronics Conference, 2010.

[34] C.A.Baguley, B. Carsten, U.K. Madawala, "The effect of DC bias conditions on ferrite core losses", IEEE transactions on Magnetics, vol. 44, No. 2, February 2008.

[35] Wai Keung Mo, David K.W. Cheng, Y. S. Lee, “Simple Approximations of the DC Flux Influence on the Core Loss Power Electronic Ferrites and Their Use in Design of Magnetic Components”, IEEE Transactions on Industrial Electronics, Vol. 44, No. 6, December 1997, pg. 788 – 799.

[36] Janis M. Niedra, “Comparative wide temperature core loss characteristics of two candidate ferrites for the NASA/TRW 1500 W PEBB converter”, NASA/CR-1999-209302.

[37] Conroy, D.K.; Pierce, G.F.; Troyk, P.R.; , "Measurement techniques for the design of high-frequency SMPS transformers," Applied Power Electronics Conference and Exposition, 1988.

[38] Chucheng Xiao; Gang Chen; Odendaal, W.G.H.; "Overview of Power Loss Measurement Techniques in Power Electronics Systems", IEEE Transactions on Industry Applications, Volume 43, Issue 3, May-june 2007, pp. 657 - 664.

[39] R. Linkous, A. W. Kelley, K. C. Armstrong, “An improved calorimeter for measuring the core loss of magnetic materials”, in proc. Appl. Power Electron. Conf., vol. 2, 6-10 Feb. 2000, pp. 633 – 639.

[40] Jalilian, A., Gosbell, V., Perera, B. and Cooper, P. (1999), ‘Double chamber calorimeter (DCC): a new approach to measure induction motor harmonic losses’, IEEE Trans. Energy Convers. 14(3), 680–685.

[41] M. Wien, “Ueber die magnetisirung durch wechselstrom”, Ann. Phys. Chem.66[13], 859-953, 1898.

[42] Agilent, “Agilent Technologies impedance measurement handbooks”, Dec. 2003.

[43] Pawel Gradzki, “ Core loss characterization and design optimization of high-frequency power ferrite devices in power electronics applications”, Virginia Tech dissertation, 1992.

[44] Pawel Gradzki, Frec C. Lee “High-frequency core loss characterization technique based on impedance measurement”, HFPC, 1991.

[45] Sato, T., Yo Sakaki , "100 KHz-10 MHz iron loss measuring system," Magnetics, IEEE Transactions on , vol.23, no.5, pp. 2593- 2595, Sep 1987.

[46] V. J. Thottuvelil, T. G. Wilson, Jr. H. A. Owen, “High-frequency measurement techniques for magnetic cores”, IEEE Trans. Power Electron., vol. 5, no. 1, Jan. 1990, pp. 41 – 53.

[47] IEEE Power Electronics Society, “IEEE Standard for test procedures for magnetic cores”, IEEE Std 393-1991.

[48] James N. Lester, and Benjamin M. Alexandrovich, ‘‘Compensating Power Measurement Phase Delay Error’’, Industry Applications Conference, vol.3, pp. 1679 -- 1684, 1999.

[49] J. Zhang, G. Skutt, F. C. Lee, “Some practical issues related to core loss measurement using impedance analyzer approach”, in proc. Appl. Power Electron. Conf., vol. 2, no. 0, part 2, 5-9 March 1995, pp. 547 – 553.

[50] Yongtao Han, Yan-Fei Liu, "A Practical Transformer Core Loss Measurement Scheme for High-Frequency Power Converter", IEEE Transactions on Industrial Electronics, 2008, pp. 941-948.

[51] Yehui Han; Cheung, G.; An Li; Sullivan, C. R.; Perreault, D.J. ,"Evaluation of magnetic materials for very high frequency power applications", Power Electronics Specialists Conference, 2008. 15-19, pp. 4270 - 4276.

[52] F. Dong Tan, Jeff L. Vollin, Slobodan M. Cuk, “A practical approach for magnetic core-loss characterization” IEEE transaction on power electronics, vo. 10, no. 2, pp. 124-130, March 1995.

[53] Vencislav Cekov Valchev, Alex Van den Bossche, ‘‘Inductors and Transformers for Power Electronics’’, Chapter 11, CRC Press, 2005.

[54] Bruce Carsten, “Why a magnetics designer should measure core loss; with a survey of loss measurement techniques and a low cost, high accuracy alternative,” in Proc. HFPC, San Jose, CA, May 1995, pp. 103–119.

[55] Ferreira, J.A., Van Wyk, J.D. , "Experimental evaluation of losses in magnetic components for power converters," Industry Applications Society Annual Meeting, 1988.

[56] Edward Herbert, “User-friendly Data for Magnetic Core Loss Calculations” , 2008.

[57] Jiles, D. and Atherton, D. (1986), ‘Theory of ferromagnetic hysteresis (invited)’, J. Appl. Phys. 55, 2115–2120.

[58] Jiles, D. C. (1994), ‘Frequency dependence of hysteresis curves in conducting magnetic materials’, J. Appl. Phys. 76(10), 5849–5855.

[59] Help document of Ansoft Maxwell 14®.

[60] D. Philips and L. Dupré, “A method for calculating switched reluctance motor core losses,” in Proc. Int. Aegean Conf. Elect. Mach. Power Electron. 1992, Kusadasi, Turkey, May 27–29, 1992, pp. 124–129.

[61] Johan J. C. Gyselinck, Luc R. L. Dupr´e, Lieven Vandevelde, and Jan A. A. Melkebeek, "Calculation of No-Load Induction Motor Core Losses Using the Rate-Dependent Preisach Model", IEEE Tran. on Magnetics, Vol. 34, No. 6, Nov. 1998.

[62] Han Ping, G.R. Skutt, Ju Zhang, Fred C. Lee, "Finite element method for ferrite core loss calculation", Applied Power Electronics Conference and Exposition, 1995.

[63] M. LoBue, V. Loyau, F. Mazaleyrat, “Analysis of Volume Distribution of Power Loss in Ferrite Cores”, Journal of Applied Physics, 2011.

[64] D. Lin, P. Zhou, W. N. Fu, Z. Badics, and Z. J. Cendes , “A Dynamic Core Loss Model for Soft Ferromagnetic and Power Ferrite Materials in Transient Finite Element Analysis”, IEEE transaction on Magnetics, 2004.

[65] M. Torrent, P. Andrada, B. Blanque, E. Martinez, J. I. Perat, J.A.Sanchez, “Method for estimating core losses in switched reluctance motors”, Euro. Trans. Electr. Power, 2010.

[66] Dan M. Ionel, Mircea Popescu, Malcolm I. McGilp, T.J.E.Miller, Stephen J. Dellinger, Robert J. Heideman, “Computation of Core losses in Electrical Machines Using Improved models for Laminated Steel”, IEEE industry applications 2007.

[67] B. Ganji, J. Faiz, K. Kasper, C.E. Carstensen, R.W. De Doncker, “Core loss model based on finite-element method for switched reluctance motors”, IET Electric Power Applications, 2009.

[68] A. Basak, C.H. Yu, G. Lloyd, "Efficient Transformer Design by Computing Core Loss Using a Novel Approach", IEEE Transaction on Magnetics, Vol. 30, No. 5, Sept. 1994.

[69] M. Joao Rosario, F. Le-Strat, P. –F. Alleaume, J. Caldinhas Vaz, J. Schroth, T. Muller, J. Costa Freire, “Low cost LTCC filters for a 30GHz satellite system”, in Proc.33rd European Microwave Conf., 7-9 Oct. 2003, vol. 2, pp. 817 – 820.

[70] W. Bakalski, N. Ilkov, O. Dernovsek, R. Matz, W. Simburger, P. Weger, A. L. Scholtz, “5-6.5 GHz LTCC power amplifier module with 0.3 W at 2.4 V in Si-bipolar”, Electronics Lett., vol. 39, no. 4, pp. 375 – 376, 20 Feb 2003.

[71] Rao Tummala, “Fundamentals of Microsystems Packaging”, McGraw Hill Professional, 1st edition, May 2001.

[72] Feingold A. H. , Heinz M., Wahlers R. L. "Compliant Dielectric and Magnetic Materials for Buried Components", IMAPS, 2002 .

[73] Michele Lim, J. Jacobus Daniel van Wyk, Fred C. Lee, Khai D. T. Ngo, "A Class of Ceramic-Based Chip Inductors for Hybrid Integration in Power Supplies", IEEE Trans. Power Electron. 2008, vol.23, pp. 1556 - 1464.

[74] Michele Lim, Jacobus Daniel van Wyk, Fred C. Lee, "Hybrid Integration of a Low-Voltage, High-Current Power Supply Buck Converter With an LTCC Substrate Inductor", IEEE Trans. Power Electron. 2010, vol.25, pp. 2287 - 2298.

[75] Qiang Li, Fred C. Lee, "High Inductance Density Low Profile Inductor Structure for Integrated DC-DC Converter Applications", Appl. Power Electron. Conf. 2009 , pp. 1011 - 1017.

[76] Miguel J. Prieto, Alberto M. Pernia, Juan M. Lopera, Juan A. Martin, Fernando Nuno, "Design and analysis of thick-film integrated inductors for power converters", IEEE transactions on industry applications, vol. 38, No. 2, March/April 2002.

[77] Qiang Li, Mingkai Mu, Fred C. Lee, "Analytical core loss models for planar inductors with non-uniform flux distribution and non-sinusoidal excitation", Applied Power Electronics Conference, Feb. 2012, pp. 1783 - 1789.

[78] Jennifer D. Pollok, Weyman Lundquist, Charles R. Sullivan, "Predicting inductance roll-off with DC excitations", Energy Conversion Congress and Exposition, Sept. 2011, pp. 2139 - 2145.

[79] Farzad Farahmand, Francis P. Dawson, J. Douglas Lavers, “Critical Temperature for Thermal Runaway in a Magnetic Material”, IEEE Transactions on Magnetics, Vol. 44, No. 11, November 2008, pg. 4513-4516.

[80] S. Ohnuma, H. J. Lee, N. Kobayashi, H. Fujimori, and T. Masumoto, “Co–Zr–O Nano-Granular Thin Films with Improved High Frequency Soft Magnetic

Properties", IEEE Transactions on Magnetics, VOL. 37, NO. 4, JULY 2001, p. 2251-2254.

[81] Andrew Franklin Goldberg, "Development of Magnetic Components for 1-10 MHz DC/DC Converters", Dissertation of Doctor of Science at Massachusetts Institute of Technology, Sep. 1988.

[82] Fausto Fiorillo · Cinzia Beatrice, "Energy Losses in Soft Magnets from DC to Radiofrequencies: Theory and Experiment", Journal of Superconductivity and Novel Magnetism, January 2011, Volume 24, Issue 1-2, pp 559-566.

[83] Alex P. Van den Bossche, Vencislav Cekov Valchev, David M. Van de Sype, Lode P. Vandenbossche, "Ferrite losses of cores with square wave voltage and DC bias", Journals of Applied Physics, Vol. 99, Issue 8, 2006, pp. 08M908 1-3.

[84] Zenchi Hayashi, Yasushi Katayama, Masaharu Edo, and Haruhiko Nishio, "High-Efficiency DC–DC Converter Chip Size Module With Integrated Soft Ferrite", IEEE Transactions on Magnetics, VOL. 39, NO. 5, SEPTEMBER 2003, pp. 3068-3072.

[85] Yasushi Katayama, Satoshi Sugahara, Haruo Nakazawa, Masaharu Edo, "High-Power-Density MHz-Switching Monolithic DC-DC Converter with Thin-Film Inductor", Power Electronics Specialists Conference, 2000. PESC 00. 2000 IEEE 31st Annual, Vol. 3, pp. 1485-1490.

[86] Ferroxcube Data Handbook, "Soft Ferrites and Accessories", 2008.

[87] Ningning Wang, Santosh Kulkarni, Brice Jamieson,James Rohan, Declan Casey, Saibal Roy, Cian O'Mathuna, "High Efficiency Si Integrated Micro-transformers Using Stacked Copper Windings for Power Conversion Applications", Applied

Power Electronics Conference and Exposition (APEC), 2012 Twenty-Seventh Annual IEEE, pp. 411-416.

[88] Ningning Wang, Terence O’Donnell, Ronan Meere, Fernando M. F. Rhen, Saibal Roy, and S. Cian O’Mathuna, “Thin-Film-Integrated Power Inductor on Si and Its Performance□in an 8-MHz Buck Converter”, IEEE TRANSACTIONS ON MAGNETICS, VOL. 44, NO. 11, NOVEMBER 2008, 4096-4099.